Distribution Agreement	
In presenting this thesis or dissertation as a partial degree from Emory University, I hereby grant to E license to archive, make accessible, and display in forms of media, now or hereafter known, including that I may select some access restrictions as a dissertation. I retain all ownership rights to the countering the right to use in future works (such as articles of	Emory University and its agents the non-exclusive my thesis or dissertation in whole or in part in all ing display on the world wide web. I understand part of the online submission of this thesis or opyright of the thesis or dissertation. I also retain
Signature:	
Ting Cheng	Date

Polyoxometalate-Modified Metal and Metal Oxides for Multifunctional Catalysis

Ву

Ting Cheng Doctor of Philosophy

	Chemistry	
	en e mba y	
_	Craig L. Hill, Ph.D.	
	Advisor	
	Brian Dyer, Ph.D.	
	Committee Member	
	Cora MacBeth, Ph.D.	
	Committee Member	
	Accepted:	
	1 1 7 1 1 1 1 1 1 1 1	
	berly Jacob Arriola, Ph.Des T. Laney School of Gra	
	·	
_	Date	

Polyoxometalate-Modified Metal and Metal Oxides for Multifunctional Catalysis

By

Ting Cheng

Bachelor of Science. Peking University, 2018

Advisor: Craig L. Hill, Ph.D.

An abstract of

A dissertation submitted to the Faculty of the

James T. Laney School of Graduate Studies of Emory University
in partial fulfillment of the requirements for the degree of

Doctor of Philosophy
in Chemistry

2023

Abstract

Polyoxometalate-Modified Metal and Metal Oxides for Multifunctional Catalysis

By

Ting Cheng

Polyoxometalate-modified metal and metal oxide materials have been applied in a wide range of fields. This dissertation focuses on the synthesis of the polyoxometalate-modified metal and metal oxides and studies their activities for photocatalysis and electrocatalysis. Chapter 2 describes the decatungstate-stabilized platinum nanoparticles (W₁₀-PtNPs) for photochemical dehydrogenation of alkanes at room temperature. The W_{10} -PtNPs (~ 20 nm) catalyze the reaction of alkane to produce alkene and hydrogen in acetonitrile under UV light with high selectivity and quantum efficiency. Several characterization methods confirm the integrity of decatung states that absorb on the surface of platinum nanoparticles during the catalysis. The calculation model of a (Na-3MeCN)₄W₁₀O₃₂/Pt₁₉ complex reveals the strong interaction between the Pt and decatungstates. Chapter 3 examines polyoxometalate-stabilized gold nanoparticles for electrochemical CO₂ reduction. Several Keggin-type POMs (PW₁₂O₄₀³⁻ and SiW₁₂O₄₀⁴⁻) are capable of protecting Au nanoparticles in aqueous solution by forming POM-AuNPs, which are centrifuged and deposited on the electrode for electrochemical CO₂ reduction in acetonitrile solution with 0.5% (v/v) H₂O. However, these POM-AuNPs only produce CO and show no obvious advantages compared to citrate-AuNPs. Chapter 4 reports a POM immobilization method by anchoring APS ligand on metal oxide light absorber that successfully fabricates a Co₉POM functionalized TiO₂ photoelectrode with three-fold photocurrent enhancement compared to bare TiO₂ in acid condition. We demonstrate the hybrid photoanode can operate for up to 5 hours with maintained Co₉POM structural integrity. To the best of our knowledge, this is the first application of functionalization of efficient OER catalyst Co₉POM on photoanode that achieves efficient water photo oxidation in acid condition. Further mechanistic studies conclude that the enhancement of photocurrent is mainly due to Co₉POM acting as a fast hole collector and active catalytic center rather than surface states passivation. TA spectroscopies further verify the fast photogenerated hole transfer from TiO₂ to Co₉POM at ps timescale. The highly charged surface by Co₉POM also modifies the TiO₂ band edge, enabling a suitable surface electric field to separate the surface photogenerated charge carrier. Chapter 5 describes the incorporation of $PV_xMo_{12-x}O_{40}^{(3+x)}$ (x = 1-3) and transition-metalsubstituted polytungstates, XPW11 (X = V, Co, Zn and Co) into the pores of HKUST-1. Studies show that the reactivity synergism exists between Cu(II) in the nodes of HKUST-1 and PV_xMo₁₂- $_{x}O_{40}^{(3+x)}$ (x = 1-3) but not for the corresponding transition-metal-substituted polytung states XPW₁₁ (X = V, Co, Zn and Co). In addition, synergism in activity also leads to synergism in stability by fast electron transfer between the POM and the MOF framework. For the XPW₁₁@HKUST, the Cu(II) nodes decompose to Cu(I) structures discovered by X-ray photoelectron spectroscopy (XPS).

Polyoxometalate-Modified Metal and Metal Oxides for Multifunctional Catalysis

By

Ting Cheng

Bachelor of Science. Peking University, 2018

Advisor: Craig L. Hill, Ph.D.

A dissertation submitted to the Faculty of the

James T. Laney School of Graduate Studies of Emory University
in partial fulfillment of the requirements for the degree of

Doctor of Philosophy
in Chemistry

2023

Acknowledgement

I would like to thank my advisor Dr. Craig Hill for accepting me as his last graduate student and opening up the polyoxometalate field for me. Thanks for his continuous support on my research and his amazing knowledge of history and geography. I want to thank Dr. Yurii Geletii for giving me hands-on experience during my earlier study. I would like to thank former members of the lab: Dr. Kevin P. Sullivan, Dr. Daniel L. Collins-Wildman, Dr. Qiushi (Benjamin) Yin, and Dr. Victoria G. Snider, who gave me substantial help on experimental details. I especially want to thank Dr. Xinlin Lu with whom I published several papers. Dr. Xinlin Lu always helps me with my research projects and offers me valuable advice on personal life. I want to thank the only current group member in the lab: Zhiyao (Philip) Zhu, who is a humorous and generous friend. I would also like to thank group members from Dr. Tianquan Lian's lab: Sheng He, who is my roommate for five years and helps me from the beginning of my life in the U.S., and Fengyi Zhao, who is my collaborator in the DOE solar program and always nice and helpful with any problems.

I would like to thank my committee members, Dr. Cora MacBeth and Dr. Brain Dyer, who teach me in the Advanced Inorganic Chemistry class and provide me with valuable feedback and insightful comments on my annual reports. I want to acknowledge the staff who trained me on several useful equipment in the Institute of Electronics and Nanotechnology and the Molecular Science Engineering at Georgia Institute of Technology. I also want to thank Dr. Alexey Kaledin and Dr. Djamaladdin Musaev at Emerson Center for Scientific Computation for their calculations on my research projects.

I would like to thank all the love from my friends and my family. I want to thank Dr. Renke Huang, Ailing Yu, Dr. Qinyi Lu, and Yuesong Hu, who joined the Department of Chemistry and shared wonderful experience with me. I want to thank Chen Lin and Dr. Jianghong Zhou from the Department of Computer Science for being my closest friends and spending time traveling and exploring unique things. Finally, I want to thank my mother, Xiaoqing Xiao, and my father, Lingcai Cheng, who strongly support me financially and mentally throughout my Ph.D. time. They will come to the U.S. very soon and I can't wait to meet them after five years of separation.

Table of Contents

Chapter 1: Introduction to Polyoxometalate-Modified Metal and Metal Oxides nultifunctional catalysis	
1.1 Overview of Polyoxometalates	
1.1.1 Polyoxometalate Structures	2
1.1.2 Polyoxometalate Redox Properties	4
1.1.3 Mixed-Valence Polyoxometalates	7
1.2 Polyoxometalate-Modified Metal Materials	9
1.2.1 Synthesis of POM-modified metal nanoparticles	10
1.2.2 Applications POM-modified metal nanoparticles	12
1.3 Polyoxometalate-Modified Metal Oxide Materials	15
1.3.1 POM-modified <i>p</i> -type photocathodes	16
1.3.2 POM-modified <i>n</i> -type photoanodes	17
1.4 Polyoxometalate-Immobilized Metal Organic Frameworks	19
1.5 Scope of Current Work	22
1.6 References	23
Chapter 2: Polyoxometalate-Stabilized Platinum Nanoparticles for Photochemi	
Dehydrogenation	
2.1 Introduction	
2.2 Experimental	
2.2.1 General Materials and Methods	
2.2.2 Synthesis of Na ₄ W ₁₀ O ₃₂ -stabilized Pt nanoparticles (W ₁₀ -PtNPs)	46
2.2.3 Photocatalytic alkane dehydrogenation	46
2.3 Results and Discussion	47
2.3.1 Synthesis and characterization of W ₁₀ -PtNPs	47
2.3.2 Reactivity and stability of W ₁₀ -PtNPs	55
2.3.3 Transient absorption spectroscopy	60
2.3.4 Calculations	60
2.4 Conclusions	66

2.5 References	67
Chapter 3: Polyoxometalate-Stabilized Gold Nanoparticles for Electrochemical Dioxide Reduction	
3.1 Introduction	73
3.2 Experimental	81
3.2.1 General Materials and Methods	81
3.2.2 Electrochemistry	82
3.3 Results and Discussion	82
3.3.1 Synthesis and characterization of PW ₁₂ -AuNPs/Citrate-AuNPs	82
3.3.2 Reactivity of PW ₁₂ -AuNPs/Citrate-AuNPs	91
3.4 Conclusions	94
3.5 References	95
Chapter 4: Co-Polyoxometalate-TiO2 Photoelectrode for Efficient Oxygen Evolution in Acidic Media	
4.1 Introduction	104
4.2 Experimental	111
4.2.1 General Materials and Methods	111
4.2.2 Preparation of POM/Co-Pi modified TiO ₂ Photoelectrodes	111
4.2.3 Photoelectrochemical Studies	113
4.2.4 Transient Absorption (TA) Spectroscopy Studies	114
4.3 Results and Discussion	116
4.3.1 Characterization of TiO ₂ and TiO ₂ -Co ₉ POM photoelectrodes	116
4.3.2 Photoelectrochemical Oxygen Evolution by TiO ₂ -Co ₉ POM	120
4.3.3 Transient Absorption Spectroscopies of TiO ₂ -Co ₉ POM	126
4.4 Conclusion	132
4.5 References	132
Chapter 5: Polyoxometalate-Incorporated Metal—Organic Frameworks for Aer Oxidation	
5.1 Introduction	144

5.2 Experimental	146
5.2.1 General Materials and Methods	146
5.2.2 Synthesis of POM@HKUST	147
5.2.3 Thiol (RSH) oxidation	148
5.3 Results and Discussion	148
5.3.1 POM@MOF Materials and Characterization	148
5.3.2 POM Leaching and Solvent Selection	151
5.4 Conclusion	152
5.5 References	153

List of Figures

Figure 1.1. Six principal broad POM structural families based on the point group of the polyhedron. MO _x L _y , of the POM
Figure 1.2. Dependence of the first one-electron reduction potentials on the negative charge5
Figure 1.3. Relationship between the first one-electron reduction potential of POMs and the acceptor number of the solvent
Figure 1.4. Polyhedral structures of "heteropoly browns" and "heteropoly blues"
Figure 1.5. Three methods for the synthesis of POM-modified metal nanoparticles10
Figure 1.6 . Photocatalytic systems of POM-modified Au nanoparticles on carbon nanotubes for the oxidative degradation of organic dyes and POM-modified Au nanoparticles in metal-organic frameworks for photocatalytic H ₂ evolution
Figure 1.7. Routes of forming POMOF or POM@MOF materials starting from the precursors of POMs and MOFs
Figure 1.8. X-ray crystal structure of POM@HKUST-1 (ball and stick)22
Figure 2.1. UV-Vis spectra of aqueous solutions of reduced Na ₄ W ₁₀ O ₃₂ and the W ₁₀ -PtNPs48
Figure 2.2. Thermogravimetric analysis (TGA) of Na ₄ W ₁₀ O ₄₀ ·12H ₂ O49
Figure 2.3. Cyclic voltammogram of 1.0 mM TBA ₄ W ₁₀ O ₄₀ in CH ₃ CN
Figure 2.4. Transmission electron microscopy (TEM) image of W ₁₀ -PtNPs50
Figure 2.5. Dynamic light scattering (DLS) data of W ₁₀ -PtNPs
Figure 2.6. Scanning electron microscopy (SEM) images of W ₁₀ -PtNPs51
Figure 2.7. EDX spectrum of W ₁₀ -PtNPs
Figure 2.8. SEM/EDX of W ₁₀ -PtNPs with elemental mapping of Pt, W, and O52
Figure 2.9. X-ray Photoelectron spectroscopy (XPS) of W ₁₀ -PtNPs53
Figure 2.10 . XPS of Pt 4f, W 4f, and Na 1s in W ₁₀ -PtNPs
Figure 2.11. UV-Vis spectra of post-salting and standard decatungstate aqueous solution55
Figure 2.12 . Hydrogen evolution kinetics from photocatalytic dehydrogenation of 50 mM 2,3-dimethylbutane by W_{10} -PtNPs, a mixture of $Na_4W_{10}O_{32}$ and Pt black, and experiments without

$Na_4W_{10}O_{32}$, Pt, and light in CH ₃ CN solution. Recyclability test of W_{10} -PtNPs for photocatalytic 2,3-dimethylbutane dehydrogenation56
Figure 2.13 . TEM images of W ₁₀ -PtNPs before and after 12 hours of continuous photochemical alkane dehydrogenation in acetonitrile
Figure 2.14 . FT-IR spectra of W ₁₀ -PtNPs before and after 12 hours of continuous photochemical alkane dehydrogenation in acetonitrile
Figure 2.15 . XPS spectra of Pt 4f and W 4f in W ₁₀ -PtNPs before and after 12 hours of continuous photochemical alkane dehydrogenation in acetonitrile
Figure 2.16 . ¹ H NMR spectrum of the acetonitrile-d ₃ solution after 3 hours of photochemical dehydrogenation of 2,3-dimethylbutane
Figure 2.17 . ¹ H NMR spectrum of the acetonitrile-d ₃ solution after 3 hours of photochemical dehydrogenation of cyclohexane
Figure 2.18 . ¹ H NMR spectrum of the chloroform-d solution after 3 hours of photochemical dehydrogenation of cyclooctane
Figure 2.19 . Graphical illustrations of structures along with free energies of complexation (in kcal/mol) calculated at $T = 298$ K and 1 atm
Figure 2.20 . The optimized structures of the "bare" W ₁₀ O ₃₂ ⁴⁻ POM ion and charge neutralized solvated (Na-3MeCN) ₄ W ₁₀ O ₃₂ complex
Figure 2.21 . Orientation horizontal: the lowest four HOMO and the LUMO orbitals of (Na-3MeCN) ₄ W ₁₀ O ₃₂
Figure 2.22 . The UV-Vis spectrum of a 0.5 mM Na ₄ W ₁₀ O ₃₂ aqueous solution in a 2 mm quartz cuvette and (Na-3MeCN) ₄ W ₁₀ O ₃₂ calculated with 600 singlets
Figure 2.23 . An optimized geometry of the (Na-3MeCN) ₄ W ₁₀ O ₃₂ /Pt ₁₉ strongly bound complex65
Figure 2.24 . Two frontier orbitals of the (Na-3MeCN) ₄ W ₁₀ O ₃₂ /Pt ₁₉ complex 66
Figure 2.25 . Density of MO states of the "bare" POM ⁴⁻ and charge neutral and solvated (Na-3MeCN) ₄ W ₁₀ O ₃₂ and its Pt complex (Na-3MeCN) ₄ W ₁₀ O ₃₂ /Pt ₁₉
Figure 3.1 . UV-Vis spectra of 0.70 mM aqueous solutions of H ₃ PW ₁₂ O ₄₀ , one-electron reduced H ₃ PW ₁₂ O ₄₀ , and the PW ₁₂ -AuNPs
Figure 3.2. TEM image of PW ₁₂ -AuNPs84
Figure 3.3. DLS data of citrate-AuNPs and PW ₁₂ -AuNPs84

Figure 3.4 . UV-Vis spectra and photograph of 0.70 mM aqueous solutions of citrate-AuNPs and the PW ₁₂ -AuNPs
Figure 3.5. TEM image of citrate-AuNPs
Figure 3.6. XPS of PW ₁₂ -AuNPs8
Figure 3.7. XPS of Au 4f and W 4f in PW ₁₂ -AuNPs
Figure 3.8. XPS of citrate-AuNPs
Figure 3.9. XPS of Au 4f and Na 1s in citrate-AuNPs
Figure 3.10. XPS of C 1s in citrate-AuNPs
Figure 3.11. UV-Vis spectra of standard and post-salting H ₃ PW ₁₂ O ₄₀ aqueous solution89
Figure 3.12 . FT-IR spectra of PW ₁₂ -AuNPs before and after 3 hours of continuous electrochemica CO ₂ reduction in acetonitrile
Figure 3.13 . Thermogravimetric analysis of H ₃ PW ₁₂ O ₄₀ · 12H ₂ O
Figure 3.14. CV of 1.0 mM ferrocene (Fc) in CH ₃ CN with 0.5% (v/v) added H ₂ O92
Figure 3.15 . CVs of PW ₁₂ -AuNPs deposited on glassy carbon electrode in CH ₃ CN with 0.5% (v/v added H ₂ O under an argon atmosphere and a CO ₂ atmosphere
Figure 3.16 . CVs of TBA ₃ PW ₁₂ in CH ₃ CN with 0.5% (v/v) added H ₂ O under an argon atmosphere and a CO ₂ atmosphere
Figure 3.17 . CVs of PW ₁₂ -AuNPs and citrate-AuNPs in CH ₃ CN with 0.5% (v/v) added H ₂ O unde a CO ₂ atmosphere94
Figure 4.1. FT-IR spectroscopy and TGA of Co ₉ POM
Figure 4.2. Raman spectra of TiO ₂ , TiO ₂ -APS-Co ₉ POM on the FTO, and Co ₉ POM solid11
Figure 4.3 . Diffuse reflectance spectra of TiO ₂ , TiO ₂ -APS, and TiO ₂ -APS-Co ₉ POM118
Figure 4.4. XPS of TiO ₂ -APS-Co ₉ POM
Figure 4.5. XPS of Ti 2p and W 4f in TiO ₂ -APS-Co ₉ POM
Figure 4.6. XPS of Co 2p and O 1s in TiO ₂ -APS-Co ₉ POM
Figure 4.7 . Linear sweep voltammogram and open circuit photovoltage of TiO ₂ and TiO ₂ Co ₉ POM under 100 mW/cm ² 365 nm illumination
Figure 4.8 . Mott-Schottky and Nyquist plot of electrochemical impedance spectroscopy of TiO ₂ -APS, and TiO ₂ -Co ₉ POM

Figure 4.9 . Band structure schematic of TiO ₂ and TiO ₂ -Co ₉ POM under illumination and dark OCP process
Figure 4.10 . Photocurrent density measured at 1.23 V _{RHE} and corresponding IPCE of TiO ₂ , TiO ₂ -APS, and TiO ₂ -Co ₉ POM plotted as a function of 365 nm illumination power density
Figure 4.11 . Chronoamperometry curve of TiO ₂ -Co ₉ POM photoanode collected at 0.73 V _{RHE} under 20 mW/cm ² 365 nm UV illumination and XPS test of Co 2p, W 4f, O 1s after stability test
Figure 4.12. XPS of Co 2p and O 1s in CoO _x
Figure 4.13 . J-V curve of H ₃ PW ₁₂ O ₄₀ and J-V photocurrent of Co-Pi modified TiO ₂ under 100 mW cm ⁻² 365 nm LED light illumination
Figure 4.14. Transient absorption spectroscopy of TiO ₂ on FTO pumped by 350 nm probe by visible white light
Figure 4.15. Transient absorption spectra of TiO ₂ -Co ₉ POM under 350 nm pump using a visible and a mid-IR probe
Figure 4.16 . TA-IR spectra of TiO ₂ , TiO ₂ -APS, and TiO ₂ -Co ₉ POM samples and kinetics comparison of three samples from 2020-2040 cm ⁻¹
Figure 4.17. Cyclic voltammetry of Co ₉ POM in pH 2 sulfate buffer solution131
Figure 5.1 . FT-IR of Na ₅ PV ₂ Mo ₁₀ O ₄₀ , HKUST-1 and PV ₂ Mo ₁₀ @HKUST and PXRD of PV ₂ Mo ₁₀ @HKUST
Figure 5.2. FT-IR of POM alone, HKUST-1 and the corresponding PXW ₁₁ @HKUST150
Figure 5.3 . N ₂ gas adsorption isotherms of PV ₂ Mo ₁₀ @HKUST and PCoW ₁₁ @HKUST measured at 77 K
Figure 5.4. Thiol consumption catalyzed by PV ₂ Mo ₁₀ @HKUST in different solvents and UV-Vis absorbance of the reduced supernatant solution after addition of SnCl ₂ under argon after reaction 152

Abbreviations and Symbols

A absorbance

APS 3-aminopropyltrimethoxysilane

ATR attenuated total reflectance

BTC 1,3,5-Benzenetricarboxylic acid (trimesic acid)

BE bulk electrolysis

CODH carbon monoxide dehydrogenase

COF covalent organic framework

CO₂RR carbon dioxide reduction reaction

CV cyclic voltammetry

DFT density functional theory
DLS dynamic light scattering
DMA N,N-dimethylacetamide

DOS density of states

EDX energy dispersive X-ray spectroscopy

FT-IR Fourier transform infrared spectroscopy

FTO fluorinated tin oxide

Fc ferrocene

Fc⁺ ferrocenium ion

GC gas chromatography

HEC hydrogen evolution catalyst

HOMO highest occupied molecular orbitals

ICP inductively coupled plasma

IPCE incident photo-to-current efficiency

IVCT intervalence charge-transfer

LMCT ligand to metal charge-transfer

LSV linear sweep voltammetry

LUMO lowest unoccupied molecular orbitals

MOF metal organic framework

NMR nuclear magnetic resonance

OER oxygen evolution reaction

POM polyoxometalate

PVMo TBA salts of $PV_nMo_{12-n}O_{40}^{(3+n)-}$ (n = 0-6)

PVW TBA salts of $PV_nW_{12-n}O_{40}^{(3+n)-}$ (n = 0-6)

QE quantum efficiency

RHE reversible hydrogen electrode

SEM scanning electron microscope

SPR surface plasma resonance

TA transient absorption

TBA tetrabutylammonium

TEM transmission electron microscope

TEOA triethanolamine

TGA thermogravimetric analysis

TOA tetraoctylammonium

TON turnover number

TOF turnover frequency

UV-Vis ultraviolet-visible spectrsocopy

WOC water oxidation catalyst

XPS X-ray photoelectron spectroscopy

XPW₁₁ Transition metal substituted polytungstates

Å angstrom (10^{-10} meters)

E potential of an electrode versus a reference, mV

E⁰ formal potential of some species, mV

Citrate-AuNPs citrate stabilized Au(0) nanoparticles

PW₁₂-AuNPs phosphotungstate stabilized Au(0) nanoparticles

W₁₀-PtNPs decatungstate stabilized Pt(0) nanoparticles

Chapter 1:

Introduction to Polyoxometalate-Modified Metal and Metal Oxides for Multifunctional Catalysis

1.1 Overview of Polyoxometalates

Polyoxometalates (POMs) represent a class of nanosized molecular metal oxides with structural and functional diversities that have been widely explored since the first synthesis by Berzelius in 1824 and the structure determination by Keggin in 1933.¹⁻³ The unique characteristics of POMs with respect to structure, geometry, and adjustable redox properties have attracted widespread attention in catalysis, nanomaterials, biomedicine, and (photo)electrochemical energy conversion.⁴⁻²⁵ In this work, we focus on polyoxometalate-modified metal and metal oxides and study their activities for photocatalysis and electrocatalysis. In addition, POMs immobilized in metal-organic frameworks (POM@MOFs) for oxidative catalysis will be briefly discussed.

1.1.1 Polyoxometalate Structures

POMs are anionic metal oxide species mostly composed of redox metal centers (Mo, W, V, and Nb) in their highest oxidation states. These electron-poor molecular units are usually formed from the condensation of basic tetra-oxoanions [MO₄]ⁿ⁻ in acidic medium giving connected [MO_n] polyhedron through corner or edge shared junctions.³ By tuning experimental variables such as concentration, pH, and temperature etc., various POMs with highly diverse structures can be synthesized.⁹ The structural features of POMs, especially the nature of the catenated polyhedral metal building blocks constituting the metal-oxo frameworks, are closely linked to their redox properties. This observation was first made by Pope who proposed a classification of POM structures into three types in 1972.²⁶ Since this historical classification, considerable advances in the structural chemistry of POMs have resulted in extending Pope's

classification to six types (Figure 1.1).

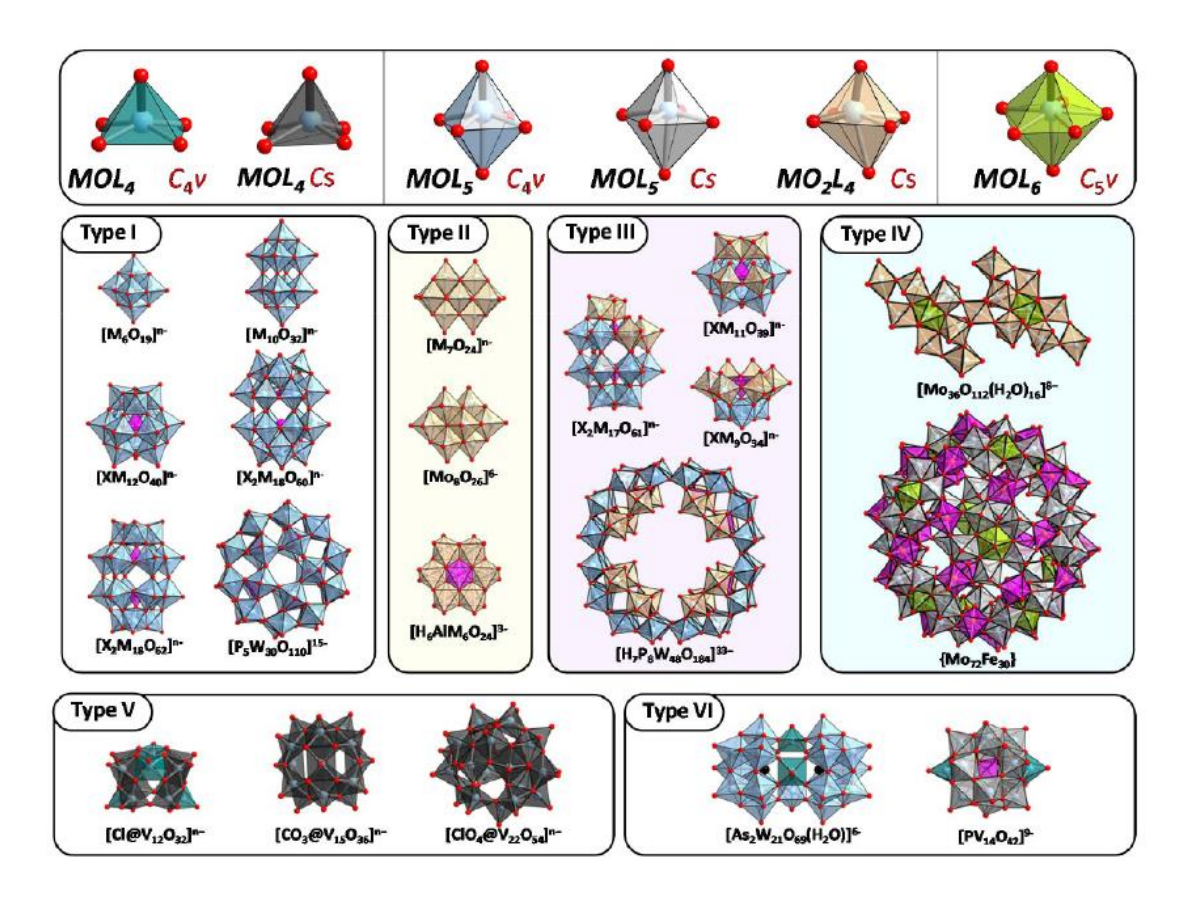


Figure 1.1. Six principal broad POM structural families based on the point group of the polyhedron, MO_xL_y , of the POM (O: oxygen atoms doubly bonded to the metal center; L = oxygen atoms singly bonded to the metal center) are named Type I, II, III, IV, V, and VI. Reproduced with permission from ref. 21. Copyright © 2022, American Chemical Society.

The first class, Type I, represents all POMs in which all the oxometalate centers (mostly Mo^{6+} or W^{6+} based) are in octahedral sites with a single unshared oxygen atom (MOL_5 with $C_{4\nu}$ symmetry). Illustrative examples of this family are the Lindqvist $[M_6O_{19}]^{n-}$, the Keggin $[XM_{12}O_{40}]^{n-}$, the Dawson $[X_2M_{18}O_{62}]^{n-}$, and the Preyssler-type $[P_5W_{30}O_{110}]^{15-}$, polyanions. Type I POMs exhibit reversible redox activity, and their reduction leads generally to mixed-valence POMs with delocalized electrons over the metals. The second structural type, namely Type II, corresponds to the polyoxoanions built from

addenda atoms with two mutually cis M=O bonds (MO₂L₄ with C_s symmetry). These POMs do not exhibit a reversible redox process because their reduction involves the addition of electrons to antibonding orbitals, which results in significant structural rearrangement of the polyanion. Type II archetypes are Anderson-type POMs or heptamolybdate [Mo₇O₂₄]⁶⁻. The POM structures built from MO₂L₄ octahedra with C_s symmetry and with MOL₅ with $C_{4\nu}$ symmetry, such as lacunary Keggin ($[XM_{11}O_{39}]^{n-}$, $[XM_{9}O_{34}]^{n-}$) or the macrocyclic type POMs, [H₇P₈W₄₈O₁₈₄]³³⁻, belong to the Type III structural family. These POMs are particularly interesting for (photo)electrocatalytic applications²⁷⁻³² because they exhibit nucleophilic oxygen atoms that are able to coordinate a large variety of transition metals and catalytically active metal atom clusters, which are suitable binding sites for reaction substrates such as O₂, H₂O₂, and CO₂. Type IV POMs contain the pentagonal bipyramidal units, MOL₆, with $C_{5\nu}$ symmetry. Such polyhedra have been identified as key building blocks for the construction of giant molybdenum POMs such as {Mo₁₃₂}, {Mo₁₅₄}, {Mo₃₆₈}, and {Mo₁₂₆W₃₀}.³³⁻³⁷ The structural Type V defines POMs exclusively constructed from square pyramids MOL₄. Such POMs are mostly built on vanadium-based hollow structures encapsulating a wide variety of anions (CO₃²-, Cl⁻, I⁻, SCN⁻, and ClO₄⁻ etc.).³⁸ The last structural type (Type VI) corresponds to POMs that result from the condensation of octahedra MOL₅ and square pyramids MOL₄ units. They often exhibit rich redox activity, as illustrated by sandwich-like compounds $[(XW_9O_{33})_2(VO)_3]^{9-}$ with $X = As^{III}$ or Sb^{III} .³⁹

1.1.2 Polyoxometalate Redox Properties

The redox properties of POMs are generally influenced by the metalate composition, the overall charge of the POMs, and its environment including

nature of the solvent, the proton concentration (pH), and the cation concentration,^{6, 40} which collectively make the electrochemical behavior of POMs fairly complicated. Here we discuss the effects of above factors with specific examples.

First, the potential of different metalates with similar structures follows the order of V > Mo > W in both aqueous and organic solvents. For instance, only V atoms in $[PV_2W_{10}]^{5-}$ are reduced during the first two-electron reduction process. Second, the negative overall charge of POMs dictates their reduction potentials. As shown in Figure 1.2, the first one-electron reduction potentials of $XW_{12}O_{40}^{7-}$ and $XW_{11}VO_{40}^{7-}$ decrease linearly with the overall anion charge of POMs, which is about 180 mV per unit charge. The heteroatom effect is small compared to the charge effect since POMs with the same charge but different heteroatoms exhibit similar potentials (e.g., Si vs. Ge and Fe vs. B). The POM

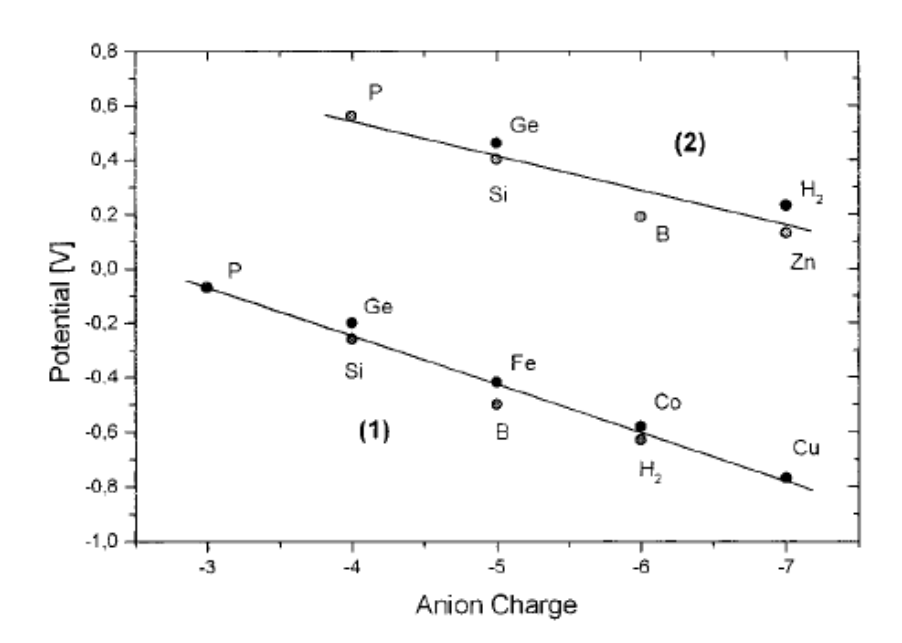


Figure 1.2. Dependence of the first one-electron reduction potentials on the negative charge: (1) $XW_{12}O_{40}^{n}$, X = P, Si, Ge, Fe, B, Co, H₂, Cu; and (2) $XW_{11}VO_{40}^{n}$, X = P, Si, Ge, B, H₂, Zn. Reproduced with permission from ref. 6. Copyright © 1998, American Chemical Society.

size also partly dictates charge and thus charge density as in the first redox potential of Preyssler-type POMs [Xⁿ⁺P₅W₃₀O₁₁₀]ⁿ⁻¹⁵, which vary with a slope of only 48 mV per unit charge.⁴¹ This slope is much lower than that of Keggin-type POMs and could be explained by the charge density: larger POMs disperse charge more effectively than smaller ones. The Preyssler and Keggin POMs have respective volumes of 1600 Å³ and 590 Å³.⁴¹ Third, Keggin POMs undergo several one-electron reductions in solutions where no protonation can happen, such as neutral aqueous and most organic solvents. In acidic aqueous conditions (pH < 1), the two one-electron waves convert into one two-electron wave and shift to more positive potentials by a proton-coupled electron transfer (PCET) process.⁴² This phenomenon could also be observed in organic solvents if a strong acid such as CF₃SO₃H is added.⁴³ Fourth, the potential of POMs vary in different solvents as shown in Figure 1.3. This is attributed to the

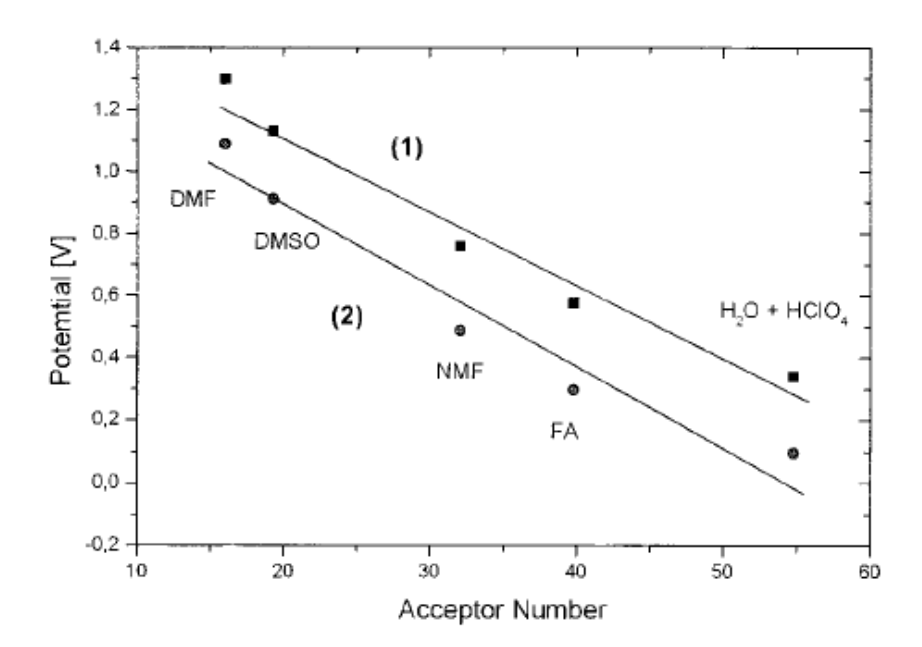


Figure 1.3. Relationship between the first one-electron reduction potential of POMs and the acceptor number of the solvent. (1) α -K₄SiW₁₂O₄₀ and (2) α -K₆P₂Mo₁₈O₆₂. Reproduced with permission from ref. 6. Copyright © 1998, American Chemical Society.

solvation energy difference in the overall thermodynamics⁴⁴ or the acceptor number that describes the Lewis acidity of the solvents.⁴⁵ The reduction peak potential shifts linearly to more negative potentials with the decreasing solvent acceptor number: H₂O (54.8) > formamide (39.8) > *N*-methylformamide (32.1) > DMSO (19.3) > DMF (16.0) because the reduced POM is better stabilized by solvents that have a higher acceptor number. In addition to above factors, the counter-cations and electrolytes also impact POM redox behaviors via cation-POM ion-pairing.⁴⁴

1.1.3 Mixed-Valence Polyoxometalates

The introduction of several electrons into polyoxometalates leads to intense blue-colored compounds in solution, usually named "heteropoly blues". These reduced POMs are designated as Class II mixed valence compounds according to the Robin-Day classification.⁴⁶ In such compounds, the added "blue" electrons are delocalized over different metal sites of the polyanions owing to fast thermal hopping ($\sim 10^9 - 10^{11} \text{ s}^{-1}$) at room temperature. While the "blue" electrons are delocalized over all 12 metal centers in the Keggin-type POMs ([XM₁₂O₄₀]ⁿ⁻), the "blue" electrons are delocalized over the 8 and 12 equatorial metal centers of decatungstate ([W₁₀O₃₂]⁶⁻) and the Wells-Dawson ([P₂W₁₈O₆₂]⁸⁻) polyanions, respectively.⁴⁷⁻⁴⁹ The UV-vis spectra of "heteropoly blues" are characterized by broad and intense absorption at wavelengths above 600 nm which are assigned as intervalence charge transfers (IVCTs: $Mo^{V} \rightarrow$ Mo^{VI} or $W^{V} \rightarrow W^{VI}$). 50, 51 A special case is the six-electron-reduced Keggin-type polyoxotungstates that are brown in color and are referred to as "heteropoly browns". In contrast to the "heteropoly blues", the electrons in "heteropoly browns" appear located within three W-W bonds forming a W^{IV}-based triad as

clearly indicated by ¹⁸³W NMR and X-ray diffraction studies.^{52, 53} Thus, the "heteropoly browns" are Robin and Day Class I complexes⁴⁶ and do not have IVCT bands. Figure 1.4 shows the structures of "heteropoly browns" and "heteropoly blues".

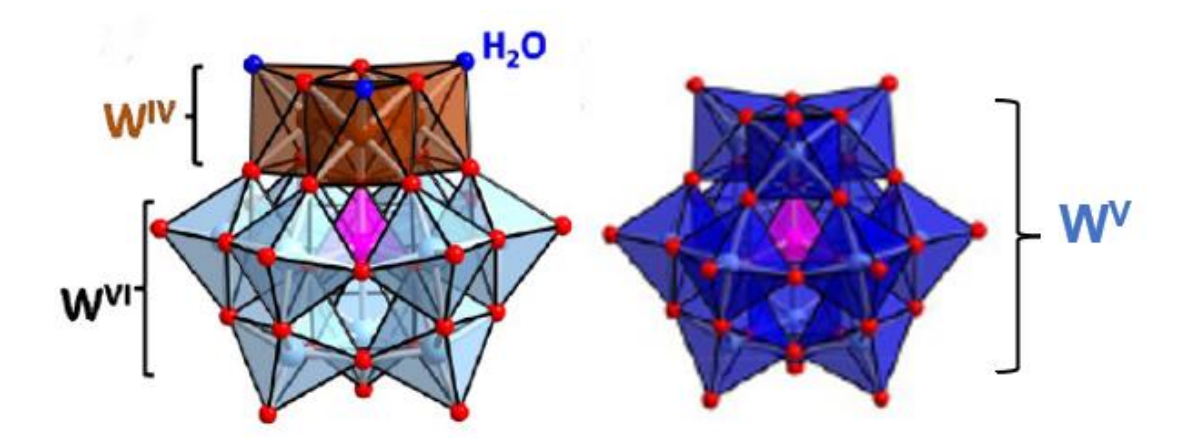


Figure 1.4. Polyhedral structures of "heteropoly browns" (left) and "heteropoly blues" (right). Different colors indicate different oxidation states: brown (+IV), light blue (+VI), and dark blue (+V). Most of W centers in "heteropoly blues" have W (VI) and W (V) properties. Reproduced with permission from ref. 21. Copyright © 2022, American Chemical Society.

The ability to reversibly accept and donate electrons makes POMs ideal for electron storage, and as a consequence, POMs are termed "electron reservoirs" or "electron sponges". Cronin et al. first reported that the Keggintype POM [SiW₁₂O₄₀]⁴⁻ acted as a recyclable redox mediator in a water splitting device. The incorporation of [SiW₁₂O₄₀]⁴⁻ in the platinum-catalyzed system produced pure hydrogen over 30 times faster than the proton exchange membrane electrolyzer at equivalent platinum loading.⁵⁴ More recently, Cronin et al. have also shown that the Dawson-type POM, [P₂W₁₈O₆₂]⁶⁻, is an appealing water-soluble charge carrier in both redox flow battery cells and electrolytic cells because this POM can accept a high number of electrons which can reach 18 electrons per POM unit.⁵⁵

1.2 Polyoxometalate-Modified Metal Materials

Metal nanoparticles are nanoparticulate metals with diameters in the range of 1–100 nm that exhibit unique physical and chemical properties. As such, they have been applied in a wide variety of fields, including catalysis, optics, electronics, sensing, medicines, surface chemistry, pharmaceutics, and fluorescent materials.56-59 The properties of metal nanoparticles can be modified with appropriate protecting ligands, polymers, and supporting materials. Methods for metal nanoparticle modification include using metal oxide supports to improve stability and reactivity,60 constructing conjugated metal-ligand interfacial bonds to achieve intraparticle charge transfer,61 employing specific biomolecules for bioimaging,62 and applying organic polymers to retain high dispersion stability by regulating interfacial interactions. 63 As a large family of anionic inorganic macromolecules, POMs have also been used to modify metal nanoparticles and their properties.^{64, 65} This research field emerged after the demonstration that POMs could modify electrode surfaces (Hg, Pt, and Au), which paved the way for later applications in electrochemistry.66 The first preparation of POM-modified metal nanoparticles was reported in 1994,67 and the resulting metal nanoparticles exhibited excellent catalytic activity, stability, and reusability in hydrogenation reactions.^{68, 69} Afterwards, a viable method for the preparation of noble-metal nanoparticles that relied on the photochemical redox properties of POMs was reported.⁷⁰ Further studies in this field have been conducted to encompass various nanoparticulate structures and different types of POMs for diverse applications.⁷¹⁻⁷³ In general, POMs including Keggin-type and Dawson-type POMs together with their lacunary species, can act as oxygen-based

multidentate ligands for capturing metals and constructing self-assembled structures, thereby resulting in new species with various structures and properties.

1.2.1 Synthesis of POM-Modified Metal Nanoparticles

The preparation methods for POM-modified metal nanoparticles can be divided into three methods according to the following classifications (Figure 1.5):

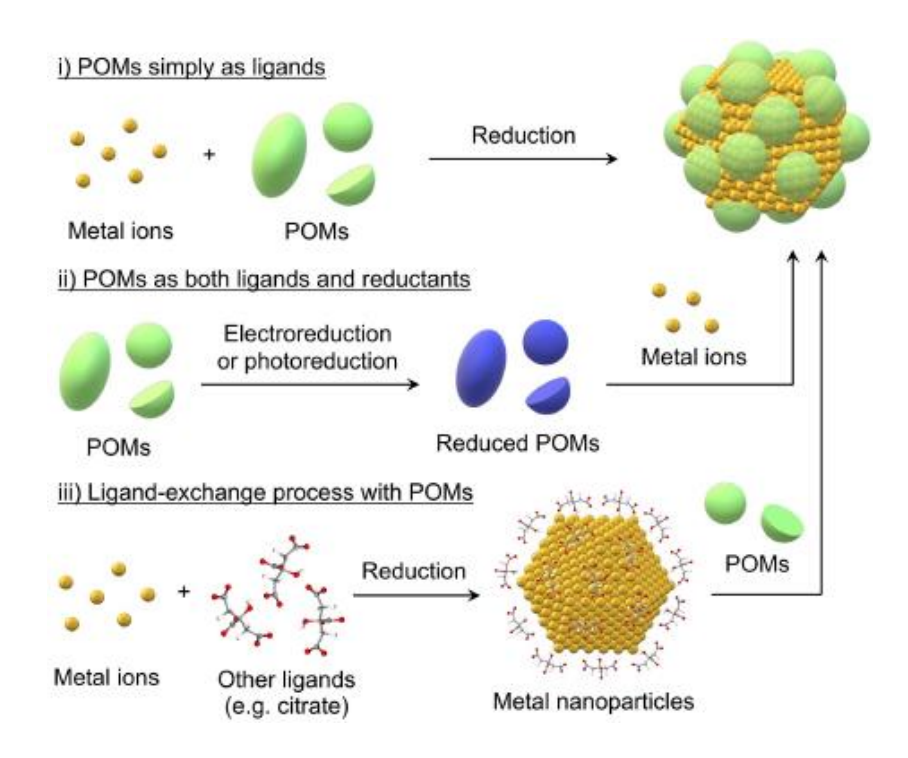


Figure 1.5. Three methods for the synthesis of POM-modified metal nanoparticles. Reproduced with permission from ref. 23. Copyright © 2022, Wiley-VCH GmbH.

(i) reduction of metal ions by suitable reductants in the presence of POM stabilizing ligands; (ii) reduction of metal ions using (photo)electrochemically reduced POMs as both reductants and ligands; and (iii) ligand exchange between POMs and metal nanoparticles stabilized by other ligands such as citrate. In the first method, POM-modified metal nanoparticles can be prepared by reducing metal ions with a number of reductants such as sodium borohydride, ascorbic acid, and hydrogen gas in the presence of various types of POMs.⁶⁷

This method is the most adopted method owing to its wide applicability to various types of POMs because general POMs with high negative charges and coordination sites can satisfy the role of stabilizing ligands. The second method is based on the reversible redox properties of POMs, whereby reduced POMs are prepared by electroreduction or photoreduction and are used as both the ligands and reductants. 70, 72 In this method, despite the limitation that only redox-active POMs with appropriate redox potentials for metal ions can be used, the control of particle size and morphology can be achieved relatively easily because of the following two reasons. First, the POM functions simultaneously as a reducing agent and a protecting ligand, which facilitates the formation of metal nanoparticles. Second, the reaction conditions of the photochemical and electrochemical reactions are more easily adjusted than the thermal reduction method. The third method is applicable since POMs are generally better stabilizing ligands than many other common ligands such as citrates, phosphates, acetates, and halogen anions.74-77 When metal nanoparticles protected by these ligands are treated with POMs, they undergo a ligandexchange process to form POM-modified metal nanoparticles. However, the exchanged ligands are supposed to be removed before practical applications, which makes this method less competitive compared to the other two methods. It is important to note that only noble-metal nanoparticles (Ru, Rh, Pd, Ag, Ir, Pt, Au) have been synthesized with POM ligands; the preparation of non-noblemetal nanoparticles has not been reported yet possibly due to their low stability. In addition, metal nanoclusters incorporated in POMs have also been explored with great success,⁷⁸⁻⁸¹ which is beyond the scope of this chapter.

1.2.2 Applications of POM-Modified Metal Nanoparticles

POM-modified metal nanoparticles have wide and promising applications in various fields such as electrochemistry, photochemistry, catalysis, and biochemistry. For example, Au nanoparticles can assist POMs with a facile twoelectron reduction of the environmentally significant analyte bromate by lowering the potential commonly needed for bromate reduction.⁸² Furthermore, POM-protected Pd and Pt nanoparticles were found to be highly efficient and stable for the electrocatalytic methanol oxidation reaction (MOR).⁷³ Oxygen reduction reaction (ORR) and CO₂ reduction reaction (CO₂RR) were also reported to be catalyzed by POM-modified Pt and Ag nanoparticles, respectively.^{83, 84} In general, the multielectron redox properties as well as high negative charges of POMs are used to facilitate electron transfer, strengthen the adsorption of the substrates, and reduce the overpotential. The photoresponsive redox properties of POMs enable attractive applications in photochemistry. The report of $[SiW_{12}O_{40}]^{4-}$ photoreduction with UV light (λ >320 nm) in the presence of 2-propanol as a sacrificial reagent and metal ions as precursors⁷⁰ is the foundation for the photochemical synthesis of POMstabilized nanoparticles. Metal-containing POMs and thiol-functionalized POMs can also be used as functional ligands. Notably, the combination of the photoredox properties of POMs and the strong coordination ability of thiols enabled the synthesis of highly stable and uniformly sized photo- and redox-active hybrid metal nanoparticles.85 The surface plasmon resonance (SPR) of these POM-modified metal nanoparticles can be used for photocatalytic reactions. For example, the SPR of Au nanoparticles was found to assist the esterification of 3-phenylpropionic acid with methanol under POM acid catalysis. This likely

arises from a local photothermal effect and/or electric field effect caused by the SPR of the Au nanoparticles. ⁸⁶ In addition, the immobilization of POM-modified metal nanoparticles on appropriate supporting materials is another strategy for efficient photocatalytic systems. For instance, POM-modified Au nanoparticles on multiwalled carbon nanotubes (Figure 1.6a) and POM-modified Pt nanoparticles inside metal-organic frameworks (MOFs) (Figure 1.6b) are visible-light-responsive photocatalysts for the oxidation of rhodamine B (RhB) or H₂ evolution. ^{87, 88} In these cases, the POMs act as multielectron transfer mediators for charge separation between the metal nanoparticles and the supporting materials to increase the photocatalytic efficiency.

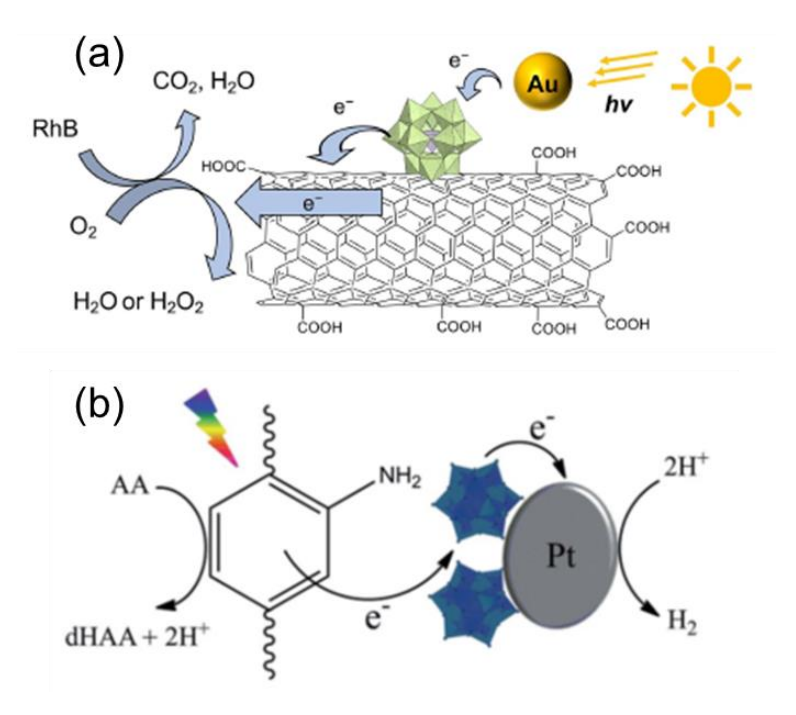


Figure 1.6. Photocatalytic systems of a) POM-modified Au nanoparticles on carbon nanotubes for the oxidative degradation of organic dyes and b) POM-modified Au nanoparticles in metal-organic frameworks for photocatalytic H₂ evolution. Reproduced from ref. 87 and ref. 88 with permission from The Royal Society of Chemistry.

The application of POM-modified metal nanoparticles in catalysis dates back to their discovery in 1994 when Finke et al. conducted a study of cyclohexene hydrogenation in acetone catalyzed by an iridium-containing POM.⁶⁷ The authors prepared the Ir-900 nanoclusters by reacting the iridium-containing POM with high pressure H₂ gas and found that the Ir-900 nanoclusters catalyzed the cyclohexene hydrogenation with high yield and excellent recyclability. Later on, POM-modified metal nanoparticles were employed in Suzuki-Miyaura, Heck, and Stille C-C and C-N coupling reactions,⁸⁹ the epoxidation of alkenes,⁷² and the aerobic oxidation of secondary alcohols.⁹⁰ In particular, POM-modified Pd nanoparticles performed well in Heck reactions, the ring-opening reactions of epoxy compounds, and acylation reactions, while POM-modified Ru nanoparticles were used for catalytic aromatic hydrogenations (Scheme 1.1).⁹¹⁻⁹³ POM-modified metal nanoparticles are found to be active and rather stable in the above reactions, which demonstrates the versability and viability of these hybrid materials.

(i) Cyclohexene hydrogenation reaction

(ii) C-C and C-N coupling reactions

$$R - X + ArB(OH)_2 \frac{[PW_{11}O_{39}]^{7-}-Pd NPs}{Ar, base, 80-85 °C, 12 h} R - Ar$$

$$X = CI, Br; R = H, CH_3, CN, COCH_3$$

R
$$\longrightarrow$$
 X + \bigcirc NH \longrightarrow Ar, 90 °C, 12 h \longrightarrow R \longrightarrow NO₂

(iii) Aerobic oxidations of secondary alcohols

(iv) Ring-opening reactions of epoxy compounds

$$R_1 = CH_2CI$$
, Ph; $R_2 = CH_3$, Ph major product

Scheme 1.1. Representative examples of organic functional group transformations catalyzed by POM-modified metal nanoparticles. Reproduced with permission from ref. 23. Copyright © 2022, Wiley-VCH GmbH.

Complementing the above applications, POM-modified metal nanoparticles have shown considerable potential in biochemical applications as well. While Ag nanoparticles are used as antibacterial agents94 and Au nanoparticles can be used in nanomedicine because of their good biocompatibility⁹⁵, POMs also possess antibacterial, antiviral, and anticancer activity.^{5, 14, 96} In this context, the first application of POM-modified Au and Ag nanoparticles in antimicrobial study was reported by a stepwise functionalization of metal nanoparticles using POMs in combination with lysine or tyrosine to manipulate their antibacterial activity. 97 Further studies suggested that the metal nanoparticles (Au and Ag) and POMs functioned synergistically, 98, 99 and the selectivity and cytotoxicity of the nanoparticles could be controlled by the type of POM. 100 Another important finding was that POM- and peptide-co-modified Au nanoparticles can function as multifunctional anti-Alzheimer drugs. 101

1.3 Polyoxometalate-Modified Metal Oxide Materials

Polyoxometalates have been widely used to modify the existing properties of metal oxides, especially photoactive semiconducting materials. The combination of POMs and semiconductors (SCs) provides an attractive way to convert solar power into clean, energy dense, and storable fuels, such as H₂ and CO₂ reduction products. Consequently, numerous semiconductors with a band gap ranging from 1.1 eV (Si) to 3.2 eV (TiO₂) have been associated with POMs to efficiently promote light-driven cathodic or anodic reactions.

1.3.1 POM-Modified *p*-type Photocathodes

Among different semiconductors, silicon appears as one of the most promising candidates to be used as a photocathode because of its abundance, biocompatibility, and ability to harvest photons from a large portion of the solar spectrum. 102 Moreover, the position of its conduction band is particularly appropriate relatively to the H+/H2 redox potential for HER and the different proton-assisted multielectron reduction potentials for CO₂. Nevertheless, bare silicon like other SCs fails to efficiently promote multielectron transfers because of slow charge-transfer kinetics. 102 Additionally, Si electrodes are often susceptible to degradation under certain harsh electrochemical conditions by the notorious photo-corrosion phenomenon. Therefore, the interface between the semiconductor and the POM constitutes a critical step in efficient and sustained photo-electrocatalysis. Lacunary Keggin [PW₁₁O₃₉]⁷-type POM hybrids have been covalently grafted on Si/SiO₂ substrates through carboxylic acid binding units.¹⁰⁴ However, the presence of an electrically insulating SiO₂ layer precluded the use of these modified surfaces for photo-electrocatalytic purposes. Improved interfacial electron transfer properties have been obtained when these hybrid assemblies were covalently attached to hydrogenterminated, oxide-free Si (Si-H) surfaces through the aryldiazonium chemistry. 105 Unlike SiO₂, Si-H possesses a very low density of electrically active surface defects (the so-called surface states), which renders it particularly attractive for electrical applications. M. J. Rose and co-workers have also prepared high electronic quality and densely packed lacunary Keggin [[PW₁₁O₃₉]⁷⁻ POM monolayers covalently bound to p- or n-type Si(111).¹⁰⁶ Recently, Cadot et al. reported on the remarkable catalytic properties for HER

of silicon photocathodes functionalized with polyoxothiometalate-incorporating polymer assemblies. The so-called anionic thio-POM resulting from the covalent association of the [Mo₃S₄(H₂O)₉]⁴⁺ cluster with the robust macrocyclic polyoxotungstate [H₇P₈W₄₈O₁₈₄]³³⁻ was electrostatically entrapped into a conducting polymer film, namely poly(3,4-ethylenedioxythiophene) (PEDOT), to durably retain the catalyst at the interface of the silicon photocathode. 107 This molecular and material engineering strategy makes thio-POM/PEDOT-coated silicon photocathodes able to produce H₂ under one-sun illumination at a rate of ca. 100 µmol cm⁻² h⁻¹ at 0 V vs RHE. Besides silicon, a p-type Cu₂O photocathode with a direct band gap of 2.0 eV has been modified with a POM catalytic multilayer of anionic Ni-containing Weakley-type [Ni₄(H₂O)₂(PW₉O₃₄)₂]¹⁰⁻ using a cationic polyethyleneimine as an electrostatic adhesive. 108 Despite a significant improvement in the stability of the photocathode under HER electrolytic conditions, the maximum photocurrent densities reached for the POM-functionalized photocathode were quite low (ca. 0.2 mA cm⁻² at 0.35 V vs RHE) and only modestly higher than those measured for a bare Cu₂O photocathode.

1.3.2 POM-Modified *n*-type Photoanodes

In parallel to these POM-modified *p*-type SC photocathodes designed for photo-electrocatalytic HER, some studies focused on the fabrication of POM-modified n-type photoanodes to catalytically promote oxidation reactions with photogenerated holes. For example, an organic lead halide perovskite photoanode was judiciously modified with dual POMs, namely [PW₁₂O₄₀]³⁻ and [{Co(H₂O)₃}₂{CoBi₂W₁₉O₆₆(OH)₄}]¹⁰⁻, both to improve the quality of the perovskite film and facilitate transfer of photogenerated holes.¹⁰⁹ By effectively

reducing the photogenerated charge carrier recombination, the photoelectrocatalytic efficiency for the oxidation of benzene into phenol was markedly boosted. The modified photoanode showed 2.6-fold higher photocurrent densities and a significantly increased conversion yield (32% vs 26%) than a pure perovskite photoanode. Apart from this report, all the other recent studies have dealt with POM-modified photoanodes for sunlight-driven OER, which is more challenging and more directly associated with solar fuel production. 110 In the report published by Hill and co-workers, semiconducting photoanodes consisting of nano-porous TiO2 and electrostatically immobilized ruthenium $([Ru^{IV}_4O_5(OH)(H_2O)_4(\gamma-PW_{10}O_{36})_2]^{9-}$ and **POMs** $[Ru^{IV}_4O_4(OH)_2(H_2O)_4(V-$ SiW₁₀O₃₄)₂]¹⁰⁻) have been prepared and used for UV-light-driven OER with photocurrent densities of 1.2 mA cm⁻² at 1.5 V vs RHE and pH = 10.¹¹¹ A recent study employed the same immobilizing method for TiO₂ coated with the cobalt POM, $[Co^{III}Co^{II}(H_2O)W_{11}O_{39}]^{7-}$, and achieved efficient and stable photocatalytic oxygen evolution under 365 nm UV light illumination. 112 In another study, an earth-abundant and cost-effective hematite α-Fe₂O₃ photoanode was decorated with $[Ru^{IV}_4O_4(OH)_2(H_2O)_4(v-SiW_{10}O_{34})_2]^{10-}$ and then protected by an optimized 4-nm-thick Al₂O₃ stabilizing layer. ¹¹³ Because of this protecting layer, the POM-modified photoanode was able to sustain the photoelectrochemical production of O_2 at 1.24 V vs RHE in aqueous solution pH = 8.3 with a nearly 100% Faradaic yield with an operating stability of >12 h which is much greater than that of an unfunctionalized photoanode. Besides binary metal oxides, there are also some examples of POM-modified photoanodes using the ternary oxide BiVO₄ as the electrode material. In the first example, a BiVO₄ photoanode modified with Keggin POMs ($[PW_{12}O_{40}]^{3-}$ or $[CoW_{12}O_{40}]^{6-}$) was prepared.

Nevertheless, such assemblies exhibited poor photo-electrocatalytic performance with disappointingly low photocurrent densities of 0.2 mA cm $^{-2}$ at about 1.8 V vs RHE in sulfate solution (pH = 5.9). 114 Better performance was reported for a BiVO₄ photoanode modified with an anionic Co-containing Weakley-type POM [Co₄(H₂O)₂(VW₉O₃₄)₂] $^{10-}$ electrostatically entrapped into a cationic polyethyleneimine multilayer. 108 Such a photoanode working at pH = 7 showed an onset potential for OER of 0.24 V vs RHE and a photocurrent density of 2.3 mA cm $^{-2}$ at 1.23 V vs RHE. The beneficial effect of the immobilized POM was clearly indicated by a ca. 400 mV cathodic shift of the onset potential and a 3-fold higher photocurrent relative to the pristine BiVO₄ photoanode.

In addition to the above POM-modified semiconductor materials, Weinstock et al. has pioneered the field of POM-stabilized metal oxide nanoparticles for homogeneous catalytic reactions including oxygen evolution¹¹⁵⁻¹¹⁸ and carbon dioxide reduction.^{119, 120} Such research highlights the unique role of POMs in protecting small metal oxide nanoclusters in solution and narrows the common division between molecular and solid-state materials.

1.4 Polyoxometalate-Immobilized Metal-Organic Frameworks

Metal-organic frameworks (MOFs) are porous materials formed by the self-assembly of organic ligands and transition metal ions or clusters through coordination bonds.^{121, 122} Due to their abundant cavities and adjustable functional groups, MOFs have widespread applications in catalysis, gas separation, and biomedicine.¹²³⁻¹²⁵ The introduction of POMs into MOF structures endows both the POMs and the MOFs with new properties by creating additional active sites and building synergistic effects for different reactions.¹²⁶⁻¹²⁸ There are generally three methods for the synthesis of MOF-

immobilized POMs as shown in Figure 1.7. The first method involves covalent bonding between POM modes and organic linkers, which generates POMbased MOF materials termed as POMOFs. 129 The second and third methods are by immersion of pre-synthesized MOFs in POM solution and in-situ synthesis via one-pot reaction of POMs, metal ions, and linkers, respectively. The POM-based MOF materials made by these two methods are labeled as POM@MOFs indicating the electrostatic nature of interactions between POMs and MOFs.

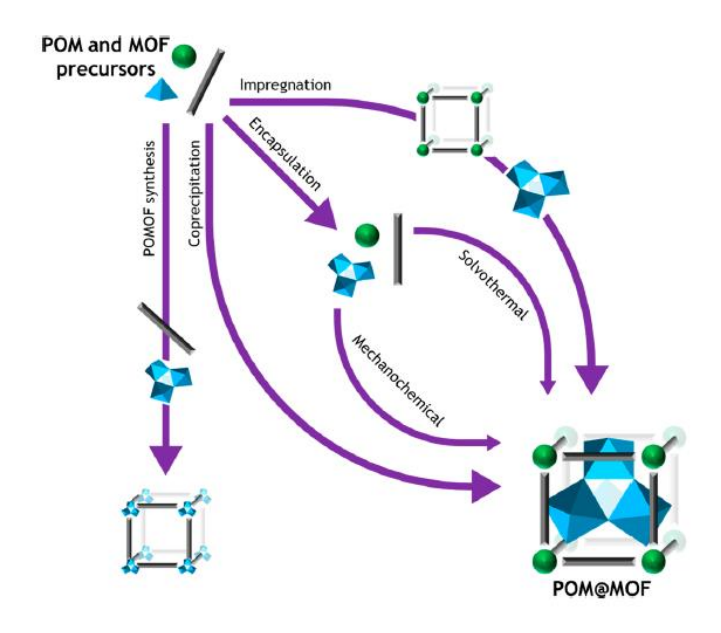


Figure 1.7. Routes of forming POMOF or POM@MOF materials starting from the precursors of POMs and MOFs. Reproduced with permission from ref. 127. Copyright © 2020, American Chemical Society.

The study in this thesis focuses on Keggin-type POMs incorporated into the pores of HKUST-1 (MOF-199), which is named after Hong Kong University of Science and Technology and uses 1,3,5-benzenetricarboxylic acid (BTC) as the organic linker and Cu²⁺ ions as inorganic nodes.¹³⁰ The two large pores in HKUST-1 have sizes of 10 and 13 Å, respectively. Considering the size of

Keggin-type POM is around 10 Å in diameter, HKUST-1 can accommodate one Keggin unit within its larger pore (Figure 1.8). 131 Since the accessible window to the larger pore is around 11 Å, Keggin POMs residing in HKUST-1 pores after hydrothermal synthesis cannot easily leak out. 132 Yamase et al. synthesized the first POM@HKUST-1 using a one-pot hydrothermal synthesis that generates POM and MOF at the same time from the initial reactants. 133 Several Keggin-type POMs including H₄SiMo₁₂O₄₀, H₃PW₁₂O₄₀ and H₃PMo₆W₆O₄₀ were generated inside the pores of HKUST-1. Subsequently, Su et al. used a different synthetic method to insert pre-formed Keggin POMs during hydrothermal synthesis. A series of Keggin complexes have been successful inserted into the pores of the MOF, NENU 1-6 (Northeast Normal University) during synthesis. 132 Hill et al. incorporated the transition-metalsubstituted Keggin, [CuPW₁₁O₃₉]⁵⁻ into HKUST-1 and found a synergistic effect between this MOF and POM with respect to both catalytic activity (H₂S and thiol oxidation) and stability. 131 In general, POM@HKUST-1 materials are effective catalysts for catalytic oxidative desulfurization, oxidation of olefins, benzene, and thiols. 134-136

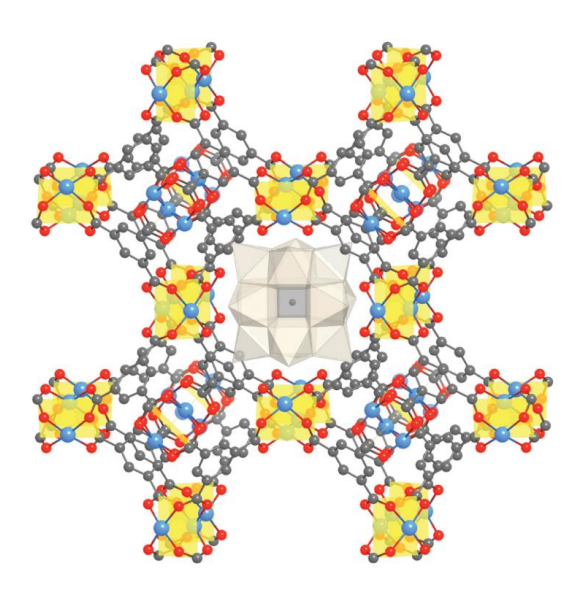


Figure 1.8. X-ray crystal structure of POM@HKUST-1 (ball and stick). Atoms: gray, C; red, O; and blue, Cu. The Keggin POM is present in white polyhedral notation and the copper(II) acetate cluster linkers are yellow cubes. Reproduced with permission from ref. 131. Copyright © 2011, American Chemical Society.

1.5 Scope of Current Work

In the following chapters, polyoxometalate-modified metal nanoparticles and metal oxide photoelectrodes for photocatalysis and electrocatalysis are explored and discussed. Chapter 2 describes the decatungstate-stabilized platinum nanoparticles (W₁₀-PtNPs) for photochemical dehydrogenation of alkanes at room temperature. The W₁₀-PtNPs (~ 20 nm) catalyze the reaction of alkane to produce alkene and hydrogen in acetonitrile under UV light with high selectivity and quantum efficiency. Several characterization methods confirm the integrity of decatungstates that absorb on the surface of platinum nanoparticles during the catalysis. The calculation model of a (Na-3MeCN)₄W₁₀O₃₂/Pt₁₉ complex reveals the strong interaction between the Pt and decatungstates. Chapter 3 examines polyoxometalate-stabilized gold nanoparticles for electrochemical CO₂ reduction. Several Keggin-type POMs (PW₁₂O₄₀³⁻ and SiW₁₂O₄₀⁴⁻) are capable of protecting Au nanoparticles in aqueous solution by forming POM-AuNPs, which are centrifuged and deposited on the electrode for electrochemical CO2 reduction in acetonitrile solution with 0.5% (v/v) H₂O. However, these POM-AuNPs only produce CO and show no obvious advantages compared to citrate-AuNPs. Chapter 4 reports the fabrication of amorphous n-type TiO₂ photoelectrodes by treatment of cationic 3-aminopropyltrimethoxysilane (APS)-functionalized TiO₂ with $Na_8K_8[Co_9(H_2O)_6(OH)_3(HPO_4)_2(PW_9O_{34})_3]$ (Co₉POM). Compared the

unmodified TiO₂, the functionalized TiO₂ photoanode, TiO₂-APS-Co₉POM, exhibits an approximately three-fold OER enhancement of photocurrent in a sulfate buffer solution (pH = 2). Mechanistic investigations indicate that Co₉POM serves as an efficient water oxidation catalyst, extracting photogenerated holes from TiO₂ at picosecond timescale. Moreover, by shifting the TiO₂ band edge, the functionalized catalytic layer creates a favorable interfacial electric field, which efficiently separates the photogenerated carriers and mitigates surface recombination. Chapter 5 describes the incorporation of $PV_xMo_{12-x}O_{40}^{(3+x)}$ (x = 1-3) and transition-metal-substituted polytung states, XPW11 (X = V, Co, Zn and Co) into the pores of HKUST-1. Their catalytic activity for aerobic thiol oxidation and stability are studied. Reactivity synergism between POM and Cu(II) ion is confirmed in these heterogeneous PVMo@HKUST catalysts, but this synergism does not exist in the polytungstate-MOFs, XPW₁₁@HKUST. corresponding Moreover, the PVMo@HKUST catalysts are stable after the reaction while XPW11@HKUST materials decompose completely under the same aerobic oxidation conditions.

1.6 References

- 1. Keggin, J. F., Structure of the crystals of 12-phosphotungstic acid.

 Nature 1933, 131, 908-909.
- 2. Baker, L. C. W.; Glick, D. C., Present General Status of Understanding of Heteropoly Electrolytes and a Tracing of Some Major Highlights in the History of Their Elucidation. *Chem. Rev.* **1998**, *98*, 3-49.
- 3. Pope, M. T.; Müller, A., Polyoxometalate Chemistry: An Old Field with New Dimensions in Several Disciplines. *Angew. Chem., Int. Ed.* **1991,** *30* (1), 34-48.

- 4. Hill, C. L.; Prosser-McCartha, C. M., Homogeneous catalysis by transition metal oxygen anion clusters. *Coord. Chem. Rev.* **1995**, *143*, 407-455.
- 5. Rhule, J. T.; Hill, C. L.; Judd, D. A.; Schinazi, R. F., Polyoxometalates in Medicine. *Chem. Rev.* **1998**, 98, 327-357.
- 6. Sadakane, M.; Steckhan, E., Electrochemical Properties of Polyoxometalates as Electrocatalysts. *Chem. Rev.* **1998**, *98*, 219-237.
- 7. Yamase, T., Photo- and Electrochromism of Polyoxometalates and Related Materials. *Chem. Rev.* **1998**, *98*, 307-325.
- 8. Lv, H.; Geletii, Y. V.; Zhao, C.; Vickers, J. W.; Zhu, G.; Luo, Z.; Song, J.; Lian, T.; Musaev, D. G.; Hill, C. L., Polyoxometalate water oxidation catalysts and the production of green fuel. *Chem. Soc. Rev.* **2012**, *41* (22), 7572-7589.
- 9. Miras, H. N.; Yan, J.; Long, D. L.; Cronin, L., Engineering polyoxometalates with emergent properties. *Chem. Soc. Rev.* **2012**, *41* (22), 7403-7430.
- 10. Wang, S. S.; Yang, G. Y., Recent advances in polyoxometalate-catalyzed reactions. *Chem. Rev.* **2015**, *115* (11), 4893-4962.
- 11. Walsh, J. J.; Bond, A. M.; Forster, R. J.; Keyes, T. E., Hybrid polyoxometalate materials for photo(electro-) chemical applications. *Coord. Chem. Rev.* **2016**, *306*, 217-234.
- 12. Yang, P.; Kortz, U., Discovery and Evolution of Polyoxopalladates. *Acc. Chem. Res.* **2018**, *51* (7), 1599-1608.
- 13. Suzuki, K.; Mizuno, N.; Yamaguchi, K., Polyoxometalate Photocatalysis for Liquid-Phase Selective Organic Functional Group Transformations. *ACS Catal.* **2018**, *8* (11), 10809-10825.

- 14. Bijelic, A.; Aureliano, M.; Rompel, A., Polyoxometalates as Potential Next-Generation Metallodrugs in the Combat Against Cancer. *Angew. Chem., Int. Ed.* **2019**, *58* (10), 2980-2999.
- 15. Chen, L.; Chen, W. L.; Wang, X. L.; Li, Y. G.; Su, Z. M.; Wang, E. B., Polyoxometalates in dye-sensitized solar cells. *Chem. Soc. Rev.* **2019**, *48* (1), 260-284.
- 16. Li, N.; Liu, J.; Dong, B. X.; Lan, Y. Q., Polyoxometalate-Based Compounds for Photo- and Electrocatalytic Applications. *Angew. Chem., Int. Ed.* **2020**, *59* (47), 20779-20793.
- 17. Anjass, M.; Lowe, G. A.; Streb, C., Molecular Vanadium Oxides for Energy Conversion and Energy Storage: Current Trends and Emerging Opportunities. *Angew. Chem., Int. Ed.* **2021**, *60* (14), 7522-7532.
- 18. Liu, R.; Streb, C., Polyoxometalate Single Atom Catalysts (POM SACs) in Energy Research and Catalysis. *Adv. Energy Mater.* **2021,** *11* (25).
- 19. Yang, L.; Lei, J.; Fan, J. M.; Yuan, R. M.; Zheng, M. S.; Chen, J. J.; Dong, Q. F., The Intrinsic Charge Carrier Behaviors and Applications of Polyoxometalate Clusters Based Materials. *Adv. Mater.* **2021**, 33 (50), e2005019.
- 20. Cameron, J. M.; Guillemot, G.; Galambos, T.; Amin, S. S.; Hampson, E.; Mall Haidaraly, K.; Newton, G. N.; Izzet, G., Supramolecular assemblies of organo-functionalised hybrid polyoxometalates: from functional building blocks to hierarchical nanomaterials. *Chem. Soc. Rev.* **2022**, *51* (1), 293-328.
- 21. Fabre, B.; Falaise, C.; Cadot, E., Polyoxometalates-Functionalized Electrodes for (Photo)Electrocatalytic Applications: Recent Advances and Prospects. *ACS Catal.* **2022**, *12* (19), 12055-12091.

- 22. Guo, L.; He, L.; Zhuang, Q.; Li, B.; Wang, C.; Lv, Y.; Chu, J.; Song, Y. F., Recent Advances in Confining Polyoxometalates and the Applications. *Small* **2023**, e2207315.
- 23. Xia, K.; Yamaguchi, K.; Suzuki, K., Recent Advances in Hybrid Materials of Metal Nanoparticles and Polyoxometalates. *Angew. Chem., Int. Ed.* **2023**, *62* (1), e202214506.
- 24. Zhang, S.; Shi, W.; Wang, X., Locking volatile organic molecules by subnanometer inorganic nanowire-based organogels. *Science* **2022**, *377*, 100-104.
- 25. Zhang, H.; Li, A.; Li, K.; Wang, Z.; Xu, X.; Wang, Y.; Sheridan, M. V.; Hu, H. S.; Xu, C.; Alekseev, E. V.; Zhang, Z.; Yan, P.; Cao, K.; Chai, Z.; Albrecht-Schonzart, T. E.; Wang, S., Ultrafiltration separation of Am(VI)-polyoxometalate from lanthanides. *Nature* **2023**, *616* (7957), 482-487.
- 26. Pope, M. T., Heteropoly and Isopoly Anions as Oxo Complexes and Their Reducibility to Mixed-Valence "Blues". *Inorg. Chem.* **1972**, *11* (8), 1973-1974.
- 27. Geletii, Y. V.; Botar, B.; Kogerler, P.; Hillesheim, D. A.; Musaev, D. G.; Hill, C. L., An all-inorganic, stable, and highly active tetraruthenium homogeneous catalyst for water oxidation. *Angew. Chem., Int. Ed.* **2008,** *47* (21), 3896-3899.
- 28. Yin, Q.; Tan, J. M.; Besson, C.; Geletii, Y. V.; Musaev, D. G.; Kuznetsov, A. E.; Luo, Z.; Hardcastle, K. I.; Hill, C. L., A Fast Soluble Carbon-Free Molecular Water Oxidation Catalyst Based on Abundant Metals. *Science* **2010**, *328*, 342-345.
- 29. Lv, H.; Guo, W.; Wu, K.; Chen, Z.; Bacsa, J.; Musaev, D. G.; Geletii, Y. V.; Lauinger, S. M.; Lian, T.; Hill, C. L., A noble-metal-free, tetra-nickel

- polyoxotungstate catalyst for efficient photocatalytic hydrogen evolution. *J. Am. Chem. Soc.* **2014**, *136* (40), 14015-14018.
- 30. Lv, H.; Song, J.; Geletii, Y. V.; Vickers, J. W.; Sumliner, J. M.; Musaev, D. G.; Kogerler, P.; Zhuk, P. F.; Bacsa, J.; Zhu, G.; Hill, C. L., An exceptionally fast homogeneous carbon-free cobalt-based water oxidation catalyst. *J. Am. Chem. Soc.* **2014**, *136* (26), 9268-9271.
- 31. Blasco-Ahicart, M.; Soriano-Lopez, J.; Carbo, J. J.; Poblet, J. M.; Galan-Mascaros, J. R., Polyoxometalate electrocatalysts based on earth-abundant metals for efficient water oxidation in acidic media. *Nat. Chem.* **2018**, *10* (1), 24-30.
- 32. Martin-Sabi, M.; Soriano-Lopez, J.; Winter, R. S.; Chen, J. J.; Vila-Nadal, L.; Long, D. L.; Galan-Mascaros, J. R.; Cronin, L., Redox tuning the Weakley-type polyoxometalate archetype for the oxygen evolution reaction. *Nat. Catal.* **2018**, *1* (3), 208-213.
- 33. Müller, A.; Beckmann, E.; Bögge, H.; Schmidtmann, M.; Dress, A., Inorganic Chemistry Goes Protein Size: A Mo₃₆₈ Nano-Hedgehog Initiating Nanochemistry by Symmetry Breaking. *Angew. Chem., Int. Ed.* **2002,** *41* (7), 1162-1167.
- 34. Ribo, E. G.; Bell, N. L.; Long, D. L.; Cronin, L., Engineering Highly Reduced Molybdenum Polyoxometalates via the Incorporation of d and f Block Metal Ions. *Angew. Chem., Int. Ed.* **2022**, *61* (21), e202201672.
- 35. Zhu, M.; Han, S.; Liu, J.; Tan, M.; Wang, W.; Suzuki, K.; Yin, P.; Xia, D.; Fang, X., {Mo₁₂₆W₃₀}: Polyoxometalate Cages Shaped by π – π Interactions. *Angew. Chem., Int. Ed.* **2022**, *61* (50), e202213910.
- 36. Müller, A.; Krickemeyer, E.; Meyer, J.; Bögge, H.; Peters, F.; Plass,

- W.; Diemann, E.; Dillinger, S.; Nonnenbruch, F.; Randerath, M.; Menke, C., [Mo₁₅₄(NO)₁₄O₄₂₀(OH)₂₈(H₂O)₇₀]^{(25±5)-}: A Water-Soluble Big Wheel with More than 700 Atoms and a Relative Molecular Mass of About 24000. *Angew. Chem., Int. Ed.* **1995**, *34* (19), 2122-2124.
- 37. Müller, A.; Krickemeyer, E.; Bögge, H.; Schmidtmann, M.; Peters, F., Organizational Forms of Matter: An Inorganic Super Fullerene and Keplerate Based on Molybdenum Oxide. *Angew. Chem., Int. Ed.* **1998,** 37 (24), 3359-3363.
- 38. Müller, A.; Krickemeyer, E.; Penk, M.; Rohlfing, R.; Armatage, A.; Bögge, H., Template-Controlled Formation of Cluster Shells or a Type of Molecular Recognition: Synthesis of[HV-22O₅₄(ClO₄)]⁶⁻ and[H₂V₁₈O₄₄(N₃)]⁵⁻. *Angew. Chem., Int. Ed.* **1991,** *30* (12), 1674-1677.
- 39. Bamba, I. F.; Falaise, C.; Marrot, J.; Gbassi, G. K.; Atheba, P.; Guillot, R.; Haouas, M.; Cadot, E., Revisiting the Three Vanadium Sandwich-Type Polyoxometalates: Structures, Solution Behavior, and Redox Properties. *Inorg. Chem.* **2022**, *61* (21), 8309-8319.
- 40. Ueda, T., Electrochemistry of Polyoxometalates: From Fundamental Aspects to Applications. *ChemElectroChem* **2018**, *5* (6), 823-838.
- 41. Fernandez, J. A.; Lopez, X.; Bo, C.; De Graaf, C.; Baerends, E. J.; Poblet, J. M., Polyoxometalates with Internal Cavities: Redox Activity, Basicity, and Cation Encapsulation in [Xⁿ⁺P₅W₃₀O₁₁₀]⁽¹⁵⁻ⁿ⁾-Preyssler Complexes, with X = Na⁺, Ca²⁺, Y³⁺, La³⁺, Ce³⁺, and Th⁴⁺. *J. Am. Chem. Soc.* **2007**, *129*, 12244-12253.
- 42. Altenau, J. J.; Pope, M. T.; Prados, R. A.; So, H., Models for Heteropoly Blues. Degrees of Valence Trapping in Vanadium(IV)- and Molybdenum(V)-

- Substituted Keggin Anions. Inorg. Chem. 1975, 14, 417-421.
- 43. Guo, S. X.; Mariotti, A. W. A.; Schlipf, C.; Bond, A. M.; G., W. A., Investigation of the Pronounced Medium Effects Observed in the Voltammetry of the Highly Charged Lacunary Anions $[\alpha\text{-SiW}_{11}O_{39}]^{8-}$ and $[\alpha\text{-PW}_{11}O_{39}]^{7-}$. *Inorg. Chem.* **2006**, *45*, 8563-8574.
- 44. Maeda, K.; Katano, H.; Osakai, T.; Himeno, S.; Saito, A., Charge dependence of one-electron redox potentials of Keggin-type heteropolyoxometalate anions. *J. Electroanal. Chem.* **1995**, 389, 167-173.
- 45. Keita, B.; Bouaziz, D.; Nadjo, L., Solvent Effects on the Redox Potentials of Potassium 12 Tungstosilicate and 18-Tungstodiphosphate. *J. Electrochem. Soc.* **1988,** *135*, 87-91.
- 46. Robin, M. B.; Day, P., Mixed Valence Chemistry-A Survey and Classification. 1968; pp 247-422.
- 47. Kozik, M.; Hammer, C. F.; Baker, L. C. W., Direct Determination by ¹⁸³W NMR of the Locations of Added Electrons in ESR-Silent Heteropoly Blues. Chemical Shifts and Relaxation Times in Polysite Mixed-Valence Transition-Metal Species. *J. Am. Chem. Soc.* **1986**, *108*, 2748-2749.
- 48. Duncan, D. C.; Hill, C. L., Synthesis and Characterization of the Mixed-Valence Diamagnetic Two-Electron-Reduced Isopolytungstate [W₁₀O₃₂]⁶. Evidence for an Asymmetric d-Electron Distribution over the Tungsten Sites. *Inorg. Chem.* **1996**, *35*, 5828-5835.
- 49. Yamase, T.; Ishikawa, E., "Mixed-Valence Decatungstates" Revisited: Crystal Structure and Aqueous Solution Chemistry of [W₁₀O₃₂]⁶⁻ and an ESR Study on Electron Delocalization. *Inorg. Chem.* **2022**, *61* (35), 13743-13755.
- 50. Papaconstantinou, E.; Pope, M. T., Heteropoly Blues. V. Electronic

- Spectra of One- to Six-Electron Blues of 18-Metallodiphosphate Anions. *Inorg. Chem.* **1970**, *9* (3), 667-669.
- 51. Varga, G. M.; Papaconstantinou, E.; Pope, M. T., Heteropoly Blues. IV. Spectroscopic and Magnetic Properties of Some Reduced Polytungstates. *Inorg. Chem.* **1970**, *9* (3), 662-667.
- 52. Jeannin, Y.; Launay, J. P.; Sedjadi, M. A. S., Crystal and Molecular Structure of the Six-Electron-Reduced Form of Metatungstate Rb₄H₈[H₂W₁₂O₄₀]*~18H₂O: Occurrence of a Metal-Metal Bonded Subcluster in a Heteropolyanion Framework. *Inorg. Chem.* **1980**, *19*, 2933-2935.
- 53. Piepgrass, K.; Baker, L. C. W., Heteropoly "Browns" as Class I Mixed Valence (W(IV,VI)) Complexes. Tungsten-183 NMR of W(IV) Trimers. *J. Am. Chem. Soc.* **1987**, *109*, 1586-1587.
- 54. Rausch, B.; Symes, M. D.; Chisholm, G.; Cronin, L., Decoupled catalytic hydrogen evolution from a molecular metal oxide redox mediator in water splitting. *Science* **2014**, *345*, 1326-1330.
- 55. Chen, J. J.; Symes, M. D.; Cronin, L., Highly reduced and protonated aqueous solutions of [P₂W₁₈O₆₂]⁶⁻ for on-demand hydrogen generation and energy storage. *Nat. Chem.* **2018**, *10* (10), 1042-1047.
- 56. Astruc, D.; Lu, F.; Aranzaes, J. R., Nanoparticles as recyclable catalysts: the frontier between homogeneous and heterogeneous catalysis. *Angew. Chem., Int. Ed.* **2005**, *44* (48), 7852-7872.
- 57. Talapin, D. V.; Lee, J.-S.; Kovalenko, M. V.; Shevchenko, E. V., Prospects of Colloidal Nanocrystals for Electronic and Optoelectronic Applications. *Chem. Rev.* **2010**, *110*, 389-458.
- 58. Linic, S.; Aslam, U.; Boerigter, C.; Morabito, M., Photochemical

- transformations on plasmonic metal nanoparticles. *Nat. Mater.* **2015,** *14* (6), 567-576.
- 59. Shi, Y.; Lyu, Z.; Zhao, M.; Chen, R.; Nguyen, Q. N.; Xia, Y., Noble-Metal Nanocrystals with Controlled Shapes for Catalytic and Electrocatalytic Applications. *Chem. Rev.* **2021**, *121* (2), 649-735.
- 60. van Deelen, T. W.; Hernández Mejía, C.; de Jong, K. P., Control of metal-support interactions in heterogeneous catalysts to enhance activity and selectivity. *Nat. Catal.* **2019**, *2* (11), 955-970.
- 61. Hu, P.; Chen, L.; Kang, X.; Chen, S., Surface Functionalization of Metal Nanoparticles by Conjugated Metal-Ligand Interfacial Bonds: Impacts on Intraparticle Charge Transfer. *Acc. Chem. Res.* **2016**, *49* (10), 2251-2260.
- 62. Erathodiyil, N.; Ying, J. Y., Functionalization of Inorganic Nanoparticles for Bioimaging Applications. *Acc. Chem. Res.* **2011**, *44*, 925-935.
- 63. Kango, S.; Kalia, S.; Celli, A.; Njuguna, J.; Habibi, Y.; Kumar, R., Surface modification of inorganic nanoparticles for development of organic—inorganic nanocomposites—A review. *Prog. Polym. Sci.* **2013**, *38* (8), 1232-1261.
- 64. Keita, B.; Liu, T.; Nadjo, L., Synthesis of remarkably stabilized metal nanostructures using polyoxometalates. *J. Mater. Chem.* **2009**, *19* (1), 19-33.
- 65. Wang, Y.; Weinstock, I. A., Polyoxometalate-decorated nanoparticles. *Chem. Soc. Rev.* **2012,** *41* (22), 7479-7496.
- 66. Keita, B.; Nadjo, L., Activation of electrode surfaces: Application to the lectrocatalysis of the hydrogen evolution reaction. *J. Electroanal. Chem.* **1985**, 191, 441-448.
- 67. Lin, Y.; Finke, R. G., Novel Polyoxoanion- and Bu4N+-Stabilized, Isolable,

- and Redissolvable, 20-30-A Ir~300-900 Nanoclusters: The Kinetically Controlled Synthesis, Characterization, and Mechanism of Formation of Organic Solvent-Soluble, Reproducible Size, and Reproducible Catalytic Activity Metal Nanoclusters. *J. Am. Chem. Soc.* **1994**, *116*, 8335-8353.
- 68. Watzky, M. A.; Finke, R. G., Transition Metal Nanocluster Formation Kinetic and Mechanistic Studies. A New Mechanism When Hydrogen Is the Reductant: Slow, Continuous Nucleation and Fast Autocatalytic Surface Growth. *J. Am. Chem. Soc.* **1997**, *119*, 10382-10400.
- 69. Aiken, J. D.; Finke, R. G., Nanocluster Formation Synthetic, Kinetic, and Mechanistic Studies.† The Detection of, and Then Methods To Avoid, Hydrogen Mass-Transfer Limitations in the Synthesis of Polyoxoanion- and Tetrabutylammonium-Stabilized, Near-Monodisperse 40 ± 6 Å Rh(0) Nanoclusters. *J. Am. Chem. Soc.* **1998**, *120*, 9545-9554.
- 70. Troupis, A.; Hiskia, A.; Papaconstantinou, E., Synthesis of Metal Nanoparticles by Using Polyoxometalates as Photocatalysts and Stabilizers. *Angew. Chem., Int. Ed.* **2002,** *41* (11), 1911-1914.
- 71. Mandal, S.; Selvakannan, P. R.; Pasricha, R.; Sastry, M., Keggin Ions as UV-Switchable Reducing Agents in the Synthesis of Au Core-Ag Shell Nanoparticles. *J. Am. Chem. Soc.* **2003**, *125*, 8440-8441.
- 72. Maayan, G.; Neumann, R., Direct aerobic epoxidation of alkenes catalyzed by metal nanoparticles stabilized by the H₅PV₋₂Mo₁₀O₄₀ polyoxometalate. *Chem. Commun.* **2005**, (36), 4595-4597.
- 73. Keita, B.; Zhang, G.; Dolbecq, A.; Mialane, P.; Secheresse, F.; Miserque, F.; Nadjo, L., Mo^V-Mo^{VI} Mixed Valence Polyoxometalates for Facile Synthesis of Stabilized Metal Nanoparticles: Electrocatalytic Oxidation of

- Alcohols. J. Phys. Chem. C. 2007, 111, 8145-8148.
- 74. Wang, Y.; Neyman, A.; Arkhangelsky, E.; Gitis, V.; Meshi, L.; Weinstock, I. A., Self-Assembly and Structure of Directly Imaged Inorganic-Anion Monolayers on a Gold Nanoparticle. *J. Am. Chem. Soc.* **2009**, *131*, 17412-17422.
- 75. Wang, Y.; Zeiri, O.; Sharet, S.; Weinstock, I. A., Role of the alkali-metal cation size in the self-assembly of polyoxometalate-monolayer shells on gold nanoparticles. *Inorg. Chem.* **2012**, *51* (14), 7436-7438.
- 76. Zhang, M.; Hao, J.; Neyman, A.; Wang, Y.; Weinstock, I. A., Influence of Polyoxometalate Protecting Ligands on Catalytic Aerobic Oxidation at the Surfaces of Gold Nanoparticles in Water. *Inorg. Chem.* **2017**, *56* (5), 2400-2408.
- 77. Leiser, S. S.; Polin, L.; Gan-Or, G.; Raula, M.; Weinstock, I. A., Hexaniobate Cluster Anion Monolayers on Gold Nanoparticles: A New Structural Role for Alkali Metal Countercations. *Inorg. Chem.* **2019**, *58* (2), 1012-1015.
- 78. Yonesato, K.; Ito, H.; Itakura, H.; Yokogawa, D.; Kikuchi, T.; Mizuno, N.; Yamaguchi, K.; Suzuki, K., Controlled Assembly Synthesis of Atomically Precise Ultrastable Silver Nanoclusters with Polyoxometalates. *J. Am. Chem. Soc.* **2019**, *141* (50), 19550-19554.
- 79. Yonesato, K.; Ito, H.; Yokogawa, D.; Yamaguchi, K.; Suzuki, K., An Ultrastable, Small {Ag₇⁵⁺} Nanocluster within a Triangular Hollow Polyoxometalate Framework. *Angew. Chem., Int. Ed.* **2020,** *59* (38), 16361-16365.
- 80. Yonesato, K.; Yamazoe, S.; Yokogawa, D.; Yamaguchi, K.; Suzuki, K., A Molecular Hybrid of an Atomically Precise Silver Nanocluster and

- Polyoxometalates for H₂ Cleavage into Protons and Electrons. *Angew. Chem., Int. Ed.* **2021,** *60* (31), 16994-16998.
- 81. Yonesato, K.; Yanai, D.; Yamazoe, S.; Yokogawa, D.; Kikuchi, T.; Yamaguchi, K.; Suzuki, K., Surface-exposed silver nanoclusters inside molecular metal oxide cavities. *Nat. Chem.* **2023**, *15*, 940-947.
- 82. Ernst, A. Z.; Sun, L.; Wiaderek, K.; Kolary, A.; Zoladek, S.; Kulesza, P. J.; Cox, J. A., Synthesis of Polyoxometalate-Protected Gold Nanoparticles by a Ligand-Exchange Method: Application to the Electrocatalytic Reduction of Bromate. *Electroanalysis* **2007**, *19* (19-20), 2103-2109.
- 83. Hsu-Yao, T.; Browne, K. P.; Honesty, N.; Tong, Y. J., Polyoxometalate-stabilized Pt nanoparticles and their electrocatalytic activities. *Phys. Chem. Chem. Phys.* **2011**, *13* (16), 7433-7438.
- 84. Guo, S. X.; Li, F.; Chen, L.; MacFarlane, D. R.; Zhang, J., Polyoxometalate-Promoted Electrocatalytic CO₂ Reduction at Nanostructured Silver in Dimethylformamide. *ACS Appl. Mater. Interfaces* **2018**, *10* (15), 12690-12697.
- 85. Martin, C.; Kastner, K.; Cameron, J. M.; Hampson, E.; Alves Fernandes, J.; Gibson, E. K.; Walsh, D. A.; Sans, V.; Newton, G. N., Redox-Active Hybrid Polyoxometalate-Stabilised Gold Nanoparticles. *Angew. Chem., Int. Ed.* **2020**, *59* (34), 14331-14335.
- 86. Sutter, S.; Trepka, B.; Siroky, S.; Hagedorn, K.; Theiss, S.; Baum, P.; Polarz, S., Light-Triggered Boost of Activity of Catalytic Bola-Type Surfactants by a Plasmonic Metal-Support Interaction Effect. *ACS Appl. Mater. Interfaces* **2019**, *11* (17), 15936-15944.
- 87. Li, S.; Yu, X.; Zhang, G.; Ma, Y.; Yao, J.; Keita, B.; Louis, N.; Zhao,

- H., Green chemical decoration of multiwalled carbon nanotubes with polyoxometalate-encapsulated gold nanoparticles: visible light photocatalytic activities. *J. Mater. Chem.* **2011**, *21* (7), 2282-2287.
- 88. Guo, W.; Lv, H.; Chen, Z.; Sullivan, K. P.; Lauinger, S. M.; Chi, Y.; Sumliner, J. M.; Lian, T.; Hill, C. L., Self-assembly of polyoxometalates, Pt nanoparticles and metal–organic frameworks into a hybrid material for synergistic hydrogen evolution. *J. Mater. Chem. A* **2016**, *4* (16), 5952-5957.
- 89. Kogan, V.; Aizenshtat, Z.; Popovitz-Biro, R.; Neumann, R., Carbon-Carbon and Carbon-Nitrogen Coupling Reactions Catalyzed by Palladium Nanoparticles Derived from a Palladium Substituted Keggin-Type Polyoxometalate. *Org. Lett.* **2002**, *4*, 3529-3532.
- 90. Maayan, G.; Neumann, R., Direct Aerobic Oxidation of Secondary Alcohols Catalysed by Pt(0) Nanoparticles Stabilized by PV₂Mo₁₀O₄₀⁵ Polyoxmetalate. *Catal. Lett.* **2008**, *123* (1-2), 41-45.
- 91. Mandal, S.; Das, A.; Srivastava, R.; Sastry, M., Keggin Ion Mediated Synthesis of Hydrophobized Pd Nanoparticles for Multifunctional Catalysis. *Langmuir* **2005**, *21*, 2408-2413.
- 92. Boujday, S.; Blanchard, J.; Villanneau, R.; Krafft, J. M.; Geantet, C.; Louis, C.; Breysse, M.; Proust, A., Polyoxomolybdate-stabilized Ru(0) nanoparticles deposited on mesoporous silica as catalysts for aromatic hydrogenation. *Chemphyschem* **2007**, *8* (18), 2636-2642.
- 93. Corma, A.; Iborra, S.; Llabrés i Xamena, F. X.; Montón, R.; Calvino, J. J.; Prestipino, C., Nanoparticles of Pd on Hybrid Polyoxometalate-Ionic Liquid Material: Synthesis, Characterization, and Catalytic Activity for Heck Reaction. *J. Phys. Chem. C.* **2010**, *114*, 8828-8836.

- 94. Chernousova, S.; Epple, M., Silver as antibacterial agent: ion, nanoparticle, and metal. *Angew. Chem., Int. Ed.* **2013,** *52* (6), 1636-1653.
- 95. Boisselier, E.; Astruc, D., Gold nanoparticles in nanomedicine: preparations, imaging, diagnostics, therapies and toxicity. *Chem. Soc. Rev.* **2009**, *38* (6), 1759-1782.
- 96. Bijelic, A.; Aureliano, M.; Rompel, A., The antibacterial activity of polyoxometalates: structures, antibiotic effects and future perspectives. *Chem. Commun.* **2018**, *54* (10), 1153-1169.
- 97. Daima, H. K.; Selvakannan, P. R.; Kandjani, A. E.; Shukla, R.; Bhargava, S. K.; Bansal, V., Synergistic influence of polyoxometalate surface corona towards enhancing the antibacterial performance of tyrosine-capped Ag nanoparticles. *Nanoscale* **2014**, *6* (2), 758-765.
- 98. Tomane, S.; Lopez-Maya, E.; Boujday, S.; Humblot, V.; Marrot, J.; Rabasso, N.; Castells-Gil, J.; Sicard, C.; Dolbecq, A.; Mialane, P.; Vallee, A., One-pot synthesis of a new generation of hybrid bisphosphonate polyoxometalate gold nanoparticles as antibiofilm agents. *Nanoscale Adv.* **2019**, *1* (9), 3400-3405.
- 99. Bastami, T. R.; Ghaedi, A.; Mitchell, S. G.; Javadian-Saraf, A.; Karimi, M., Sonochemical synthesis of polyoxometalate-stabilized gold nanoparticles for point-of-care determination of acetaminophen levels: preclinical study in an animal model. *RSC Adv.* **2020**, *10* (28), 16805-16816.
- 100. Umapathi, A.; Nagaraju, N. P.; Madhyastha, H.; Jain, D.; Srinivas, S. P.; Rotello, V. M.; Daima, H. K., Highly efficient and selective antimicrobial isonicotinylhydrazide-coated polyoxometalate-functionalized silver nanoparticles. *Colloids Surf. B* **2019**, *184*, 110522.

- 101. Gao, N.; Sun, H.; Dong, K.; Ren, J.; Qu, X., Gold-nanoparticle-based multifunctional amyloid-beta inhibitor against Alzheimer's disease. *Chem. Eur. J.* **2015**, *21* (2), 829-835.
- 102. Sun, K.; Shen, S.; Liang, Y.; Burrows, P. E.; Mao, S. S.; Wang, D., Enabling silicon for solar-fuel production. *Chem. Rev.* **2014**, *114* (17), 8662-8719.
- 103. White, J. L.; Baruch, M. F.; Pander Iii, J. E.; Hu, Y.; Fortmeyer, I. C.; Park, J. E.; Zhang, T.; Liao, K.; Gu, J.; Yan, Y.; Shaw, T. W.; Abelev, E.; Bocarsly, A. B., Light-Driven Heterogeneous Reduction of Carbon Dioxide: Photocatalysts and Photoelectrodes. *Chem. Rev.* 2015, 115 (23), 12888-12935. 104. Laurans, M.; Trinh, K.; Dalla Francesca, K.; Izzet, G.; Alves, S.; Derat, E.; Humblot, V.; Pluchery, O.; Vuillaume, D.; Lenfant, S.; Volatron, F.; Proust, A., Covalent Grafting of Polyoxometalate Hybrids onto Flat Silicon/Silicon Oxide: Insights from POMs Layers on Oxides. *ACS Appl. Mater. Interfaces* 2020, 12 (42), 48109-48123.
- 105. Laurans, M.; Dalla Francesca, K.; Volatron, F.; Izzet, G.; Guerin, D.; Vuillaume, D.; Lenfant, S.; Proust, A., Molecular signature of polyoxometalates in electron transport of silicon-based molecular junctions. *Nanoscale* **2018**, *10* (36), 17156-17165.
- 106. Gurrentz, J. M.; Rose, M. J., Covalent Attachment of Polyoxometalates to Passivated Si(111) Substrates: A Stable and Electronic Defect-Free Si|POM Platform. *J. Phys. Chem. C.* **2021**, *125* (26), 14287-14298.
- 107. Tourneur, J.; Fabre, B.; Loget, G.; Vacher, A.; Meriadec, C.; Ababou-Girard, S.; Gouttefangeas, F.; Joanny, L.; Cadot, E.; Haouas, M.; Leclerc-Laronze, N.; Falaise, C.; Guillon, E., Molecular and Material Engineering of

- Photocathodes Derivatized with Polyoxometalate-Supported Mo₃S₄ HER Catalysts. *J. Am. Chem. Soc.* **2019**, *141* (30), 11954-11962.
- 108. Kim, H.; Bae, S.; Jeon, D.; Ryu, J., Fully solution-processable Cu₂O–BiVO₄ photoelectrochemical cells for bias-free solar water splitting. *Green Chem.* **2018**, *20* (16), 3732-3742.
- 109. Fang, W.; Yan, D.; Tao, R.; Sun, Z.; Li, F.; Xu, L., Polyoxometalates acting as a hole-transfer mediator and crystallization accelerant in a perovskite photoanode for the photoelectrocatalytic oxidation of benzene into phenol. *Dalton Trans.* **2020**, *49* (29), 10084-10090.
- 110. Lewis, N. S.; Nocera, D. G., Powering the planet: Chemical challenges in solar energy utilization. *Proc. Natl Acad. Sci. USA* **2006**, *103*, 15729-15735.
- 111. Lauinger, S. M.; Sumliner, J. M.; Yin, Q.; Xu, Z.; Liang, G.; Glass, E. N.; Lian, T.; Hill, C. L., High Stability of Immobilized Polyoxometalates on TiO₂ Nanoparticles and Nanoporous Films for Robust, Light-Induced Water Oxidation. *Chem. Mater.* **2015**, *27* (17), 5886-5891.
- 112. Nandan, S. P.; Gumerova, N. I.; Schubert, J. S.; Saito, H.; Rompel, A.; Cherevan, A.; Eder, D., Immobilization of a [Co^{III}Co^{II}(H₂O)W₁₁O₃₉]⁷-Polyoxoanion for the Photocatalytic Oxygen Evolution Reaction. *ACS Mater. Au* **2022**, *2* (4), 505-515.
- 113. Lauinger, S. M.; Piercy, B. D.; Li, W.; Yin, Q.; Collins-Wildman, D. L.; Glass, E. N.; Losego, M. D.; Wang, D.; Geletii, Y. V.; Hill, C. L., Stabilization of Polyoxometalate Water Oxidation Catalysts on Hematite by Atomic Layer Deposition. *ACS Appl. Mater. Interfaces* **2017**, *9* (40), 35048-35056.
- 114. Xi, L.; Jin, Z.; Sun, Z.; Liu, R.; Xu, L., Enhanced photoelectrocatalytic performance for water oxidation by polyoxometalate molecular doping in BiVO₄

- photoanodes. Appl. Catal. Gen. 2017, 536, 67-74.
- 115. Raula, M.; Gan Or, G.; Saganovich, M.; Zeiri, O.; Wang, Y.; Chierotti, M. R.; Gobetto, R.; Weinstock, I. A., Polyoxometalate complexes of anatase-titanium dioxide cores in water. *Angew. Chem., Int. Ed.* **2015**, *54* (42), 12416-12421.
- 116. Chakraborty, B.; Gan-Or, G.; Raula, M.; Gadot, E.; Weinstock, I. A., Design of an inherently-stable water oxidation catalyst. *Nat. Commun.* **2018**, 9 (1), 4896.
- 117. Chakraborty, B.; Gan-Or, G.; Duan, Y.; Raula, M.; Weinstock, I. A., Visible-Light-Driven Water Oxidation with a Polyoxometalate-Complexed Hematite Core of 275 Iron Atoms. *Angew. Chem., Int. Ed.* **2019**, *58* (20), 6584-6589.
- 118. Kumar Tiwari, C.; Roy, S.; Tubul-Sterin, T.; Baranov, M.; Leffler, N.; Li, M.; Yin, P.; Neyman, A.; Weinstock, I. A., Emergence of Visible-Light Water Oxidation Upon Hexaniobate-Ligand Entrapment of Quantum-Confined Copper-Oxide Cores. *Angew. Chem., Int. Ed.* **2022**, e202213762.
- 119. Zhang, G.; Baranov, M.; Wang, F.; Poblet, J. M.; Kozuch, S.; Leffler, N.; Shames, A. I.; Clemente-Juan, J. M.; Neyman, A.; Weinstock, I. A., Soluble Complexes of Cobalt Oxide Fragments Bring the Unique CO₂ Photoreduction Activity of a Bulk Material into the Flexible Domain of Molecular Science. *J. Am. Chem. Soc.* **2021**, *143* (49), 20769-20778.
- 120. Zhang, G.; Wang, F.; Tubul, T.; Baranov, M.; Leffler, N.; Neyman, A.; Poblet, J. M.; Weinstock, I. A., Complexed Semiconductor Cores Activate Hexaniobate Ligands as Nucleophilic Sites for Solar-Light Reduction of CO₂ by Water. *Angew. Chem., Int. Ed.* **2022**, *61* (49), e202213162.

- 121. Zhou, H. C.; Long, J. R.; Yaghi, O. M., Introduction to metal-organic frameworks. *Chem. Rev.* **2012**, *112* (2), 673-674.
- 122. Furukawa, H.; Cordova, K. E.; O'Keeffe, M.; Yaghi, O. M., The chemistry and applications of metal-organic frameworks. *Science* **2013**, *341* (6149), 1230444.
- 123. Lee, J.; Farha, O. K.; Roberts, J.; Scheidt, K. A.; Nguyen, S. T.; Hupp, J. T., Metal-organic framework materials as catalysts. *Chem. Soc. Rev.* **2009**, 38 (5), 1450-1459.
- 124. Li, J. R.; Kuppler, R. J.; Zhou, H. C., Selective gas adsorption and separation in metal-organic frameworks. *Chem. Soc. Rev.* **2009**, *38* (5), 1477-1504.
- 125. Horcajada, P.; Gref, R.; Baati, T.; Allan, P. K.; Maurin, G.; Couvreur, P.; Ferey, G.; Morris, R. E.; Serre, C., Metal-organic frameworks in biomedicine. *Chem. Rev.* **2012**, *112* (2), 1232-1268.
- 126. Samaniyan, M.; Mirzaei, M.; Khajavian, R.; Eshtiagh-Hosseini, H.; Streb, C., Heterogeneous Catalysis by Polyoxometalates in Metal–Organic Frameworks. *ACS Catal.* **2019**, *9* (11), 10174-10191.
- 127. Buru, C. T.; Farha, O. K., Strategies for Incorporating Catalytically Active Polyoxometalates in Metal-Organic Frameworks for Organic Transformations. *ACS Appl. Mater. Interfaces* **2020**, *12* (5), 5345-5360.
- 128. Liu, Y.; Tang, C.; Cheng, M.; Chen, M.; Chen, S.; Lei, L.; Chen, Y.; Yi, H.; Fu, Y.; Li, L., Polyoxometalate@Metal-Organic Framework Composites as Effective Photocatalysts. *ACS Catal.* **2021**, *11* (21), 13374-13396.
- 129. Miras, H. N.; Vila-Nadal, L.; Cronin, L., Polyoxometalate based open-frameworks (POM-OFs). *Chem. Soc. Rev.* **2014**, *43* (16), 5679-5699.

- 130. Chui, S. S.-Y.; Lo, S. M.-F.; Charmant, J. P. H.; Orpen, A. G.; Williams, I. D., A Chemically Functionalizable Nanoporous Material [Cu₃(TMA)₂(H₂O)₃]_n. *Science* **1999**, 283, 1148-1150.
- 131. Song, J.; Luo, Z.; Britt, D. K.; Furukawa, H.; Yaghi, O. M.; Hardcastle, K. I.; Hill, C. L., A multiunit catalyst with synergistic stability and reactivity: a polyoxometalate-metal organic framework for aerobic decontamination. *J. Am. Chem. Soc.* **2011**, *133* (42), 16839-16846.
- 132. Sun, C. Y.; Liu, S. X.; Liang, D. D.; Shao, K. Z.; Ren, Y. H.; Su, Z. M., Highly Stable Crystalline Catalysts Based on a Microporous Metal-Organic Framework and Polyoxometalates. *J. Am. Chem. Soc.* **2009**, *131*, 1883-1888.
- 133. Yang, L.; Naruke, H.; Yamase, T., A novel organic/inorganic hybrid nanoporous material incorporating Keggin-type polyoxometalates. *Inorg. Chem. Commun.* **2003**, *6* (8), 1020-1024.
- 134. Xu, X.; Chen, S.; Chen, Y.; Sun, H.; Song, L.; He, W.; Wang, X., Polyoxometalate Cluster-Incorporated Metal-Organic Framework Hierarchical Nanotubes. *Small* **2016**, *12* (22), 2982-2990.
- 135. Gao, Y.; Lv, Z.; Gao, R.; Zhang, G.; Zheng, Y.; Zhao, J., Oxidative desulfurization process of model fuel under molecular oxygen by polyoxometalate loaded in hybrid material CNTs@MOF-199 as catalyst. *J. Hazard. Mater.* **2018**, 359, 258-265.
- 136. Zhong, X.; Lu, Y.; Luo, F.; Liu, Y.; Li, X.; Liu, S., A Nanocrystalline POM@MOFs Catalyst for the Degradation of Phenol: Effective Cooperative Catalysis by Metal Nodes and POM Guests. *Chem. Eur. J.* **2018**, *24* (12), 3045-3051.

Chapter 2:

Polyoxometalate-Stabilized Platinum Nanoparticles for Photochemical Alkane Dehydrogenation

Abstract

The development of cost-effective systems for alkene production by direct alkane dehydrogenation is of scientific and commercial interest. The irradiation of hexachloroplatinic acid, sodium decatungstate, and 2-propanol as a reducing agent, in a deaerated aqueous solution under 365 nm LED light forms Na₄W₁₀O₃₂-stabilized Pt(0) nanoparticles (**W₁₀-PtNPs**) in high yield. Irradiation of W₁₀-PtNPs suspended in acetonitrile (MeCN) solutions of alkanes produces alkenes in ~85% selectivity and hydrogen with quantum yields ~0.20 and turnover numbers ~100. This reverse process of catalytic hydrogenation is endothermic and endoergic thus converts light into chemical energy. Several arguments are consistent with the decatungstate adsorbed on the Pt NPs and not freely diffusing decatungstate as the photochemically active entity including the fact that neither Na₄W₁₀O₃₂ nor Pt(0) alone under these conditions is inactive. The W₁₀-PtNPs can be isolated and re-used. Transient absorption spectroscopy indicates that Pt perturbs the Na₄W₁₀O₃₂ excited state properties. Computational models display a charge-neutralizing solvated (Na-3MeCN)₄W₁₀O₃₂ structure where MeCN forms a well-defined hydrogen bonded network involving the bridging oxygens of decatungstate. The UV-Vis spectrum of this solvated decatungstate is simulated based on its molecular orbitals and is consistent with the experimental results. Calculations of the dyadic structure, (Na-3MeCN)₄W₁₀O₃₂/Pt₁₉ reveal that the decatungstate is strongly bound to the Pt(0) nanoparticles and that this interaction involves heretofore unrecognized multiple Ptto-POM d-d transitions in the infrared region.

2.1 Introduction

The dehydrogenation of alkanes to alkenes is one of the most investigated areas in organic synthesis and has received considerable attention from the petrochemical industry because of the increasing global demand for light alkenes.^{1, 2} The majority of research has

focused on thermal alkane dehydrogenation with metal and metal oxide catalysts, which suffer from harsh reaction conditions and low conversion rate. For example, the Pt/TiO₂-Al₂O₃ catalyst for propane dehydrogenation operates at 873 K and results in only a ca. 50% conversion to propene.³ Homogenous catalysts such as iridium pincer complexes, i.e., (fBu4PCP)Ir, drive reactions at lower temperature and are more efficient for alkene production, but these processes require a sacrificial alkene reagent, M, as the hydrogen acceptor, eq 1, to overcome the unfavorable thermodynamics.⁴⁻⁷ The direct photocatalytic dehydrogenation of hydrocarbons, eq 2, is highly desirable, but the unfavorable thermodynamics and kinetics (cleavage of unactivated C-H bonds) makes it as difficult to achieve as it is attractive. There are reports of photocatalytic alkane dehydrogenation, eq 2, but these have limitations. One system uses Vaska-type rhodium complexes, [RhCl(CO)(PR₃)₂] (R = Me, Et, and Ph), as alkane photodehydrogenation catalysst.⁸⁻¹⁰ However, the recyclability of these photocatalysts is poor and key features of the mechanisms remain unclear.

alkane + M
$$\rightarrow$$
 alkene + MH₂ (1)

alkane + light
$$\rightarrow$$
 alkene + H₂ (2)

Our group reported that polyoxometalates (POMs), metal-oxo clusters of high-valent early-transition metals (V, Mo, W, Nb, and Ta),¹¹ including decatungstate, W₁₀O₃₂⁴⁻, photocatalyze alkane C-H bond cleavage with the platinum cocatalyst,¹²⁻¹⁵ a process that has been used quite recently by several groups in C-H bond functionalization chemistry.¹⁶⁻²¹ Decatungstate has also been combined with cobaloxime pyridine chloride to achieve cooperative hydrogen atom transfer for photochemical alkane dehydrogenation²² although the yield was lower than that in the decatungstate/platinum system. All these applications demonstrate the important role of decatungstate in alkane dehydrogenation.

While POMs in the absence of a hydrogen evolution catalyst such as Pt(0) are very poor at evolving H₂, we reasoned that having intimate and molecular communication between the

photocatalyst (light-absorber and hydrogen-atom abstractor, namely, W₁₀O₃₂⁴⁻) and a hydrogen evolution catalyst (HEC) would significantly facilitate eq 2. This process constitutes an alternative route to solar fuel (H₂) complementing conventional artificial photosynthesis (photoreduction of H₂O and/or CO₂) given that eq 2 is thermodynamically uphill. Since platinum metal is a well-known catalyst for hydrogen evolution and POMs are well studied stabilizers of some metal(0) nanoparticles,²³⁻²⁶ we sought conditions under which the POM photocatalyst and the HEC could remain in intimate contact during photo-driven alkane dehydrogenation. After several different trials, we successfully prepared Na₄W₁₀O₃₂-stabilized Pt(0) nanoparticles (NPs) (20 nm), **W**₁₀-PtNPs, by a facile one-pot photochemical synthesis, and that this hybrid nanosystem photo-dehydrogenates alkanes, eq 2, at ambient temperature with near-UV light and can be re-used.

2.2 Experimental

2.2.1 General Materials and Methods

All chemical reagents were purchased from Sigma-Aldrich Chemical Co. (St. Louis, MO) and were used directly without further purification. UV-Vis spectra were recorded with an Agilent 8453 spectrophotometer equipped with a diode array detector using a 1.0 cm optical path length quartz cuvette. Infrared spectra (2% sample in KBr pellet) were recorded on a Nicolet TM 6700 Fourier transform infrared (FT-IR) spectrometer. Transmission electron microscopy (TEM) measurements were conducted on a Hitachi H-7500 transmission electron microscope at an accelerating voltage of 80 kV in the Robert P. Apkarian Integrated Electron Microscopy Core at Emory University. SEM-EDX data were collected on a HITACHI SU8230 FE-SEM at an accelerating voltage of 10 kV in Institute of Electronics and Nanotechnology at Georgia Institute of Technology. X-ray photoelectron spectroscopy (XPS) were conducted on a thermos K-ALPHA XPS instrument. The TGA data were collected on a Mettler Toledo

TGA instrument. Dynamic light scattering (DLS) data were acquired on a NanoPlus DLS Particle Size Analyzer instrument (Particulate Systems, Norcross, GA). 1 H nuclear magnetic resonance (NMR) spectra were acquired on a Varian INOVA 400 spectrometer using deuterated chloroform (δ 7.24) as an external standard. Gas chromatography (GC) analysis of the gas phase was analyzed using an Agilent 7890 gas chromatograph with a 5 Å molecular sieve column, a thermal conductivity detector, and argon carrier gas.

2.2.2 Synthesis of Na₄W₁₀O₃₂-stabilized Pt nanoparticles (W₁₀-PtNPs):

Na₄W₁₀O₃₂·12H₂O was synthesized according to previous reports¹² and the water content was determined by thermogravimetric analysis (TGA) (Figure 2.2). A 5 mL aqueous solution of 0.70 mM Na₄W₁₀O₃₂, 0.17 mM H₂PtCl₆, and 0.50 M 2-propanol was put into a 1-cm path length cell deareated with argon and covered with a plastic cap. The solution was stirred and irradiated with 365 nm LED light, the intensity of which on the cell was measured by a radiometer as 100 mW/cm². The color of the solution quickly turned into dark blue and then gradually changed to dark brown after exposure to air. The dark brown solution was centrifuged at 5,500 rpm for 30 min, the resulting supernatant decanted via pipette, and the remaining solids redissolved in water.

2.2.3 Photocatalytic alkane dehydrogenation:

W₁₀-**PtNPs** (5 mg) were dispersed in 5 mL of CH₃CN containing 50 mM alkane in a 1 cm path length cell deareated with argon and covered with a plastic cap. The solution was stirred and irradiated with 365 nm LED light, the intensity of which on the cell was measured by a radiometer to be 100 mW/cm². Control experiments were conducted using (a) Na₄W₁₀O₃₂ and platinum black mixture (the ratio of Na₄W₁₀O₃₂ to platinum black equals that of **W**₁₀-**PtNPs**) with light, (b) only Na₄W₁₀O₃₂(s) with light, (c) only platinum black (s) with light, and

(d) **W**₁₀-**PtNPs** without light. The reaction conversion and selectivity for alkene product were determined by nuclear magnetic resonance (NMR) spectroscopy. The amount of the hydrogen gas was quantified by gas chromatography (GC). The difference between the moles of alkene and hydrogen was within 5% throughout the experiment, thus validating equation 2. The quantum efficiency (QE) was measured using the following equation: QE = 2 × *N*(alkene) / *N*(photons). To assess the recyclability of **W**₁₀-**PtNPs**, the solution after the initial catalytic photodehydrogenation was centrifuged at 5,500 rpm for 30 minutes; the **W**₁₀-**PtNPs** were collected and re-dispersed in a fresh 5 mL CH₃CN solution of 50 mM alkane for subsequent runs.

2.3 Results and Discussion

2.3.1 Synthesis and characterization of W₁₀-PtNPs.

This binary nanosystem is prepared using a one-pot photoredox reaction and is characterized by a range of physical methods under heterogeneous conditions, meaning there is no detectable dissocation of Na₄W₁₀O₃₂ from the Pt NPs surfaces. The synthesis involves mixing hexachloroplatinic acid (0.20 mM), sodium decatungstate (0.70 mM), and the reducing agent 2-propanol (0.50 M) in a deaerated aqueous solution under 365 nm LED light illumination. The decatungstate excited state after light absorption is first reduced by 2-propanol producing an equivalent quantity of acetone, and the resulting dark-blue reduced POM then reduces Pt(IV) to Pt(0) NPs, which associate the decatungstate molecules stabilizing the NPs to aggregation and forming quite robust **W₁₀-PtNPs**. The platinum reduction returns decatungstate to the ground electronic state of its resting oxidation state with all four tungsten centers in the +6 (d⁰) state. The decatungstate immediately bond to the surfaces of the nascent Pt(0) NPs stabilizing them as **W₁₀-PtNPs**.²⁴ The UV-Vis spectra of reduced Na₄W₁₀O₃₂ and Na₄W₁₀O₃₂-stabilized Pt nanoparticles are shown in Figure 2.1. The

reduced sodium decatungstate has a relatively weak O-to-W charge-transfer absorption band at 360 nm. Two strong absorption peaks at 650 nm and 770 nm are assigned to inter-valence charge transfer bands in $W_{10}O_{32}^{6-}$ and $W_{10}O_{32}^{5-}$ respectively.²⁷ The final solution of Na₄W₁₀O₃₂-stabilized Pt nanoparticles is dark-brown. Importantly, a similar attempted preparation using tetra-*n*-butylammonium (TBA) decatungstate in acetonitrile does not produce decatungstate-stabilized Pt nanoparticles because the sterically large organic counter cations likely prevent the close POM-Pt interaction seen in the case of **W**₁₀-PtNPs. The solution of **W**₁₀-PtNPs can be centrifuged, decanted off the supernatant to remove residual $W_{10}O_{32}^{4-}$ and $PtCl_6^{2-}$, and the remaining solids, effectively the **W**₁₀-PtNPs, readily redissolve in water. This process is repeated several times to prepare the purified **W**₁₀-PtNP powder and the corresponding solution for subsequent characterizations.

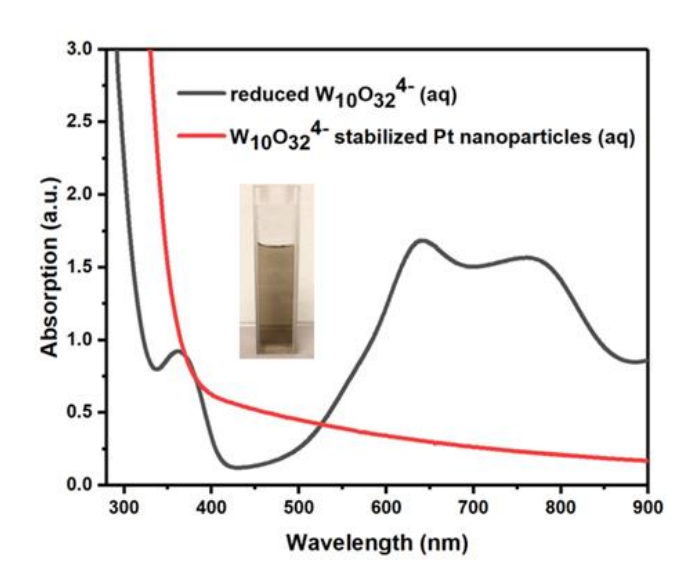


Figure 2.1. UV-Vis spectra of aqueous solutions of reduced Na₄W₁₀O₃₂ (black) and the **W**₁₀-**PtNPs** (red). Inset: Photograph of aqueous solution of the **W**₁₀-**PtNPs** in a 1 cm quartz cuvette.

It is important to note that W_{10} -PtNPs can be dissolved in a CH₃CN/H₂O (v/v = 9/1) mixed solvent and catalyze alkane dehydrogenation as described in the experimental section. Under these conditions, $W_{10}O_{32}^{4-}$ is fairly effective at preventing rapid aggregation of Pt(0) particles to microscale or macroscale ones. However, $W_{10}O_{32}^{4-}$ does dissociate form the Pt(0) surfaces generating the POM in solution after the catalytic reaction. This is proved by the

zeta potential of the solution, which changes from -36.2 mV (indicates moderate stability) before the reaction to -12.5 mV (indicates incipient instability) after the reaction. Since the anionic polyoxometalates contribute to most of the zeta potential, the notable change suggests that a significant number of POMs dissociate from the Pt(0) NP surfaces. The average size of W10-PtNPs doesn't change much after the reaction because the ~20 nm Pt nanoparticles are still protected by the remaining decatungstate molecules. As a consequence, all W10-PtNPs-catalyzed reactions are conducted in pure acetonitrile where Na4W10O32 is insoluble preventing any detectable dissociation of the POM from the Pt surfaces. Moreover, the redox potentials for decatungstates shift positively as the water content in the mixed solvent increases,^{27, 28} while decatungstates in pure organic solvents such as acetonitrile or dimethylformamide exhibit the most negative potential that is favorable for the hydrogen evolution reaction (Figure 2.3).

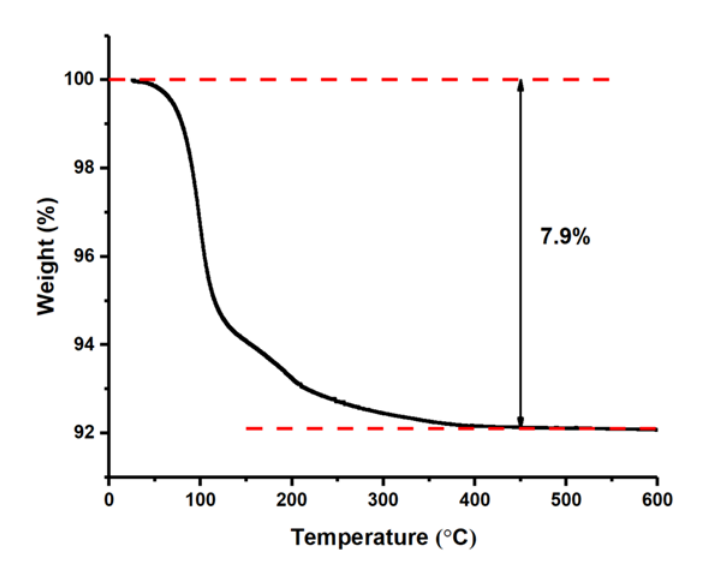


Figure 2.2. Thermogravimetric analysis (TGA) of Na₄W₁₀O₄₀·12H₂O.

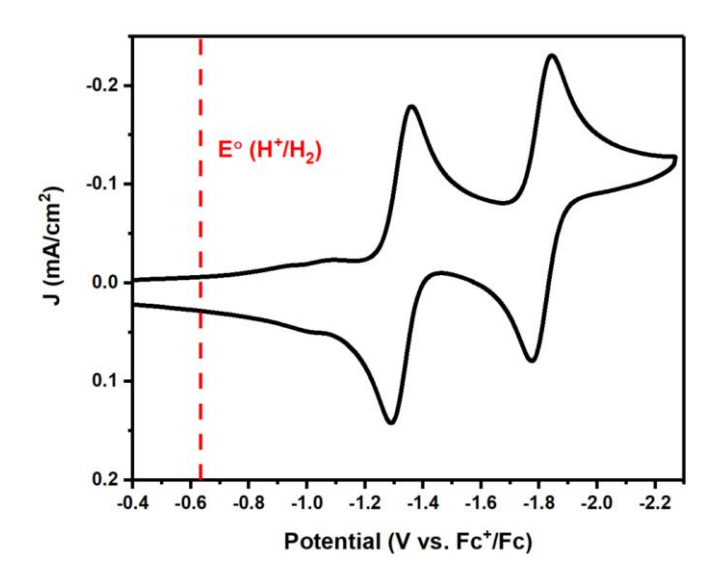


Figure 2.3. Cyclic voltammogram of 1.0 mM TBA₄W₁₀O₄₀ in CH₃CN. The cyclic voltammogram was measured at the scan rate of 100 mV/s on the glassy carbon electrode. The red vertical dash line indicates the potential of hydrogen evolution reaction.

The transmission electron microscopy (TEM) image (Figure 2.4) and dynamic light scattering (DLS) data (Figure 2.5) reveal that the average size of **W**₁₀-**PtNPs** is around 20 nm, which is similar to the size of other POM-stabilized Pt(0) nanoparticles.^{24, 29} The scanning electron microscope (SEM) images (Figure 2.6) display a comparable particle size and the energy dispersive X-ray spectroscopy (EDX) (Figure 2.7 and Figure 2.8) confirms the existence of decatungstate surrounding the platinum NPs.

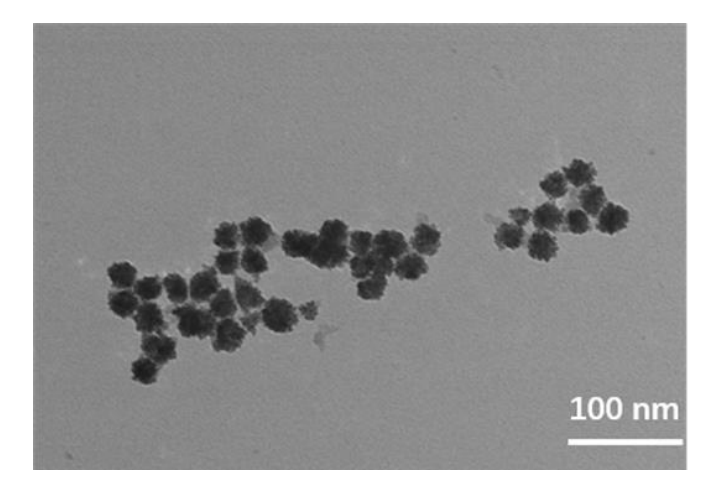


Figure 2.4. Transmission electron microscopy (TEM) image of W₁₀-PtNPs.

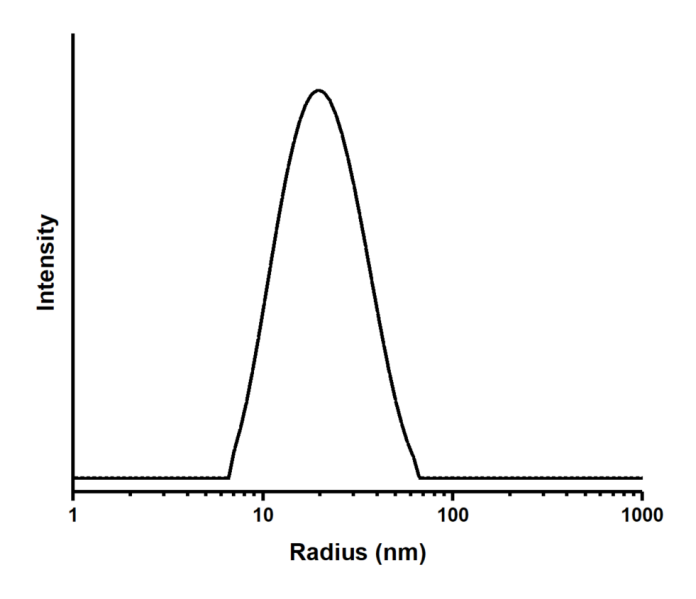


Figure 2.5. Dynamic light scattering (DLS) data of W_{10} -PtNPs.

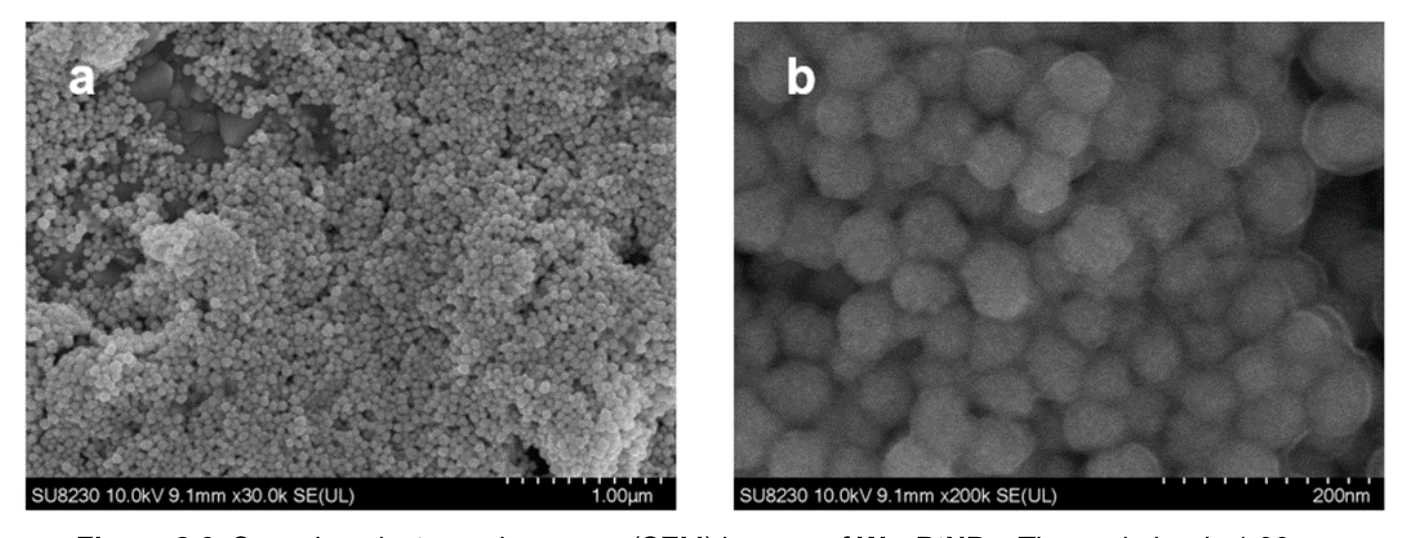


Figure 2.6. Scanning electron microscopy (SEM) images of W_{10} -PtNPs. The scale bar is 1.00 μ m for Figure a and 200 nm for Figure b.

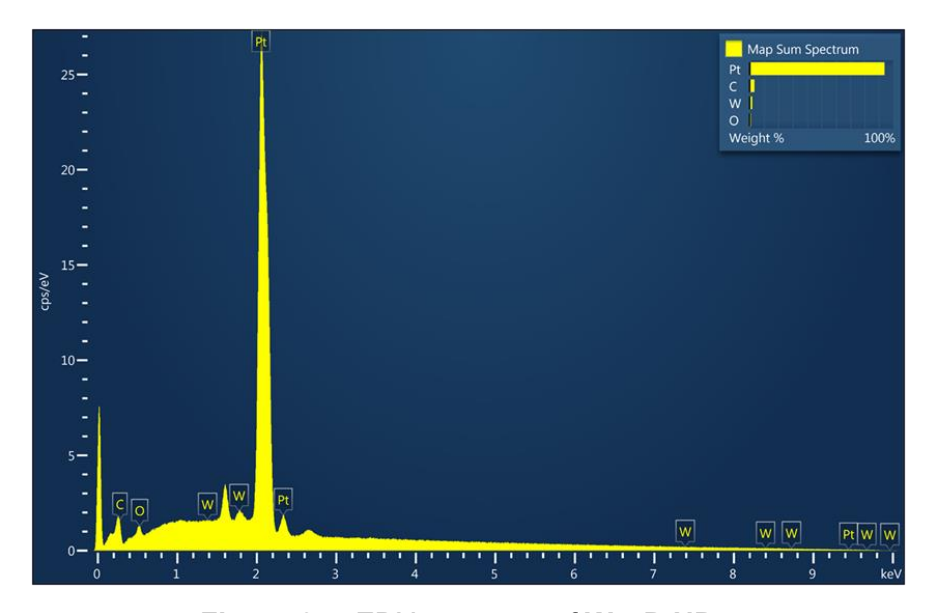


Figure 2.7. EDX spectrum of W₁₀-PtNPs.

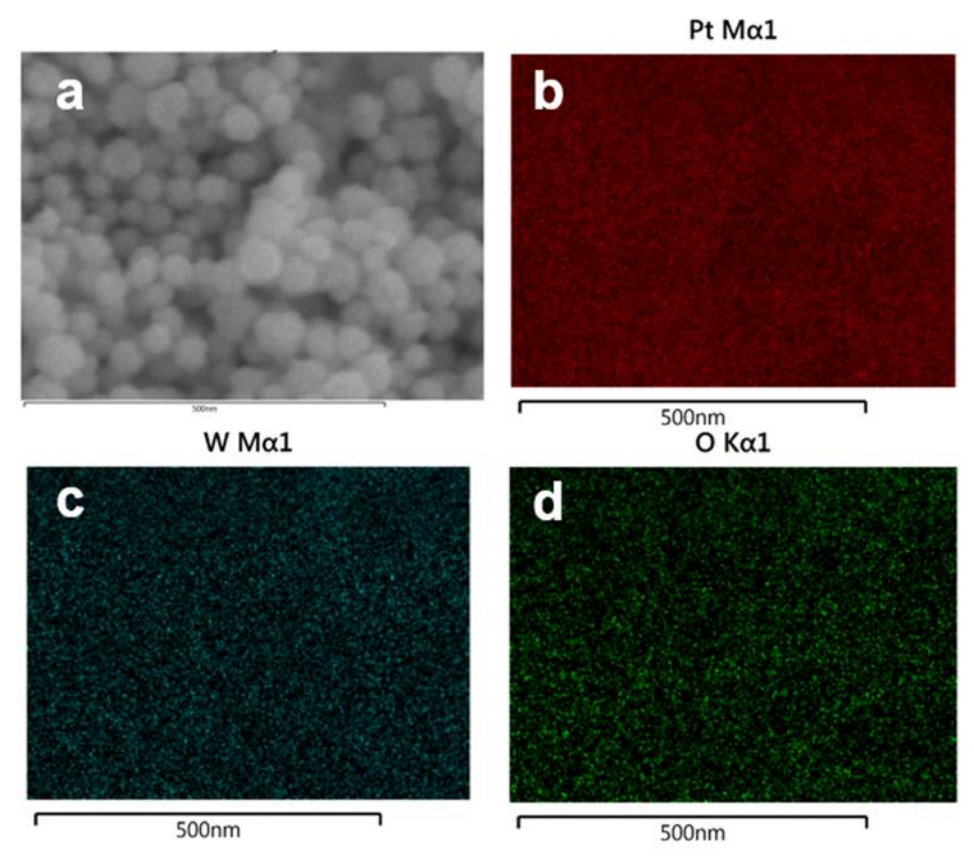


Figure 2.8. SEM of (a) W_{10} -PtNPs with elemental mapping of (b) Pt, (c) W, and (d) O.

The X-ray photoelectron spectroscopy (XPS) (Figure 2.9) of **W**₁₀-**PtNPs** in powder form was then conducted to establish the ratio of POM to Pt. The asymmetric XPS spectrum of Pt 4f (Figure 2.10a) has well separated spin-orbit components (Δ_{metal} =3.35 eV) with the Pt 4f_{7/2} peak and the Pt 4f_{5/2} peak located at 71.23 eV and 74.58 eV, respectively. The XPS spectrum

of W 4f (Figure 2.10b) shows the binding energy of 36.08 eV (4f_{7/2}) and 38.28 eV (4f_{5/2}), which corresponds to the W (VI) chemical state. The loss feature for W(VI) at 42 eV is also observed. The POM: Pt ratio in \mathbf{W}_{10} -PtNPs, based on the atomic ratio of W to Pt in the XPS spectra and the number of tungsten atoms in decatungstate is calculated to be 0.06.

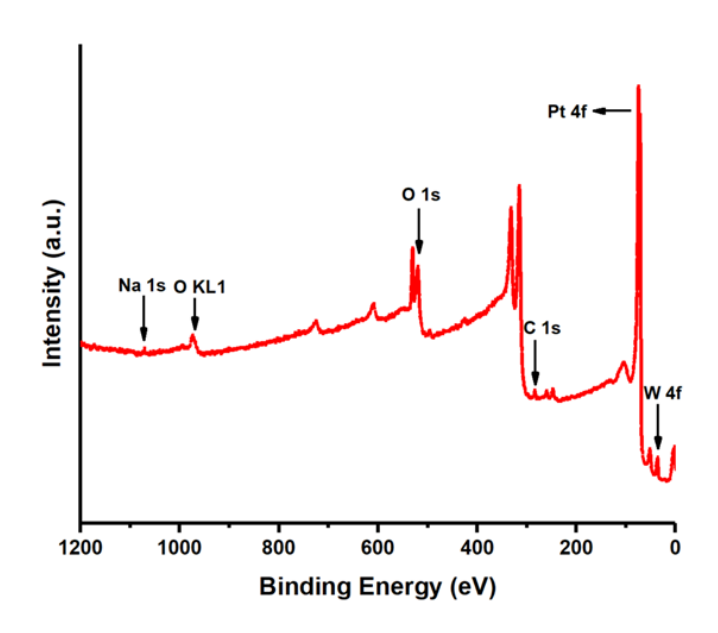
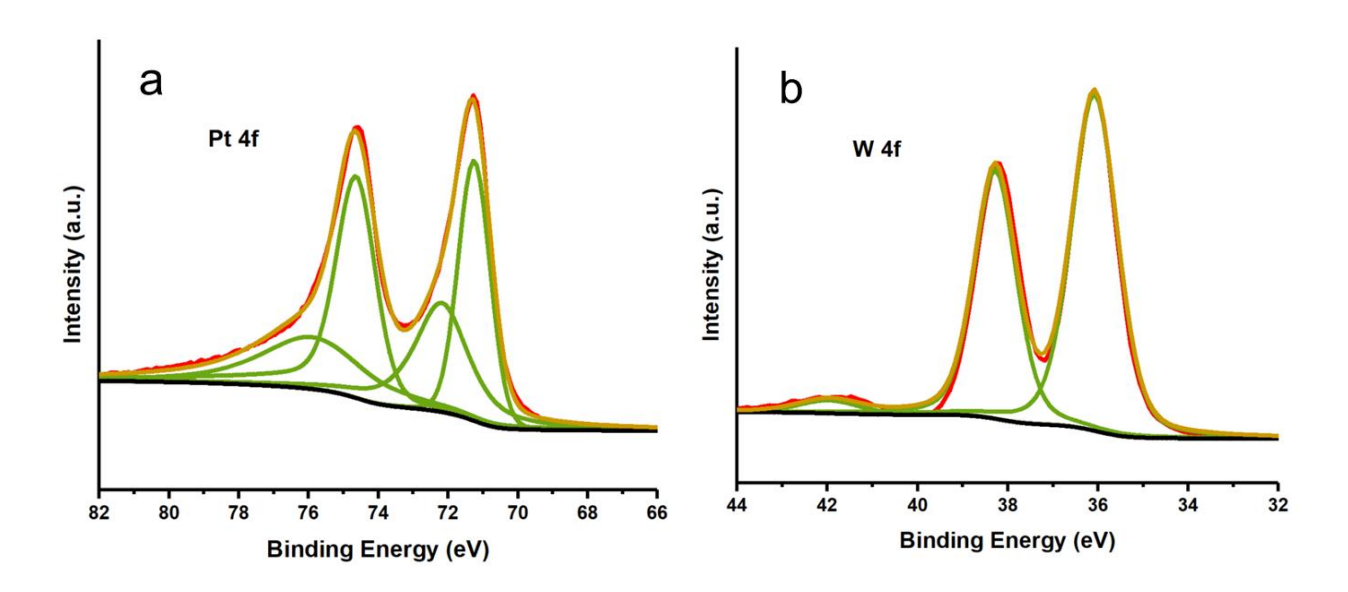


Figure 2.9. X-ray Photoelectron spectroscopy (XPS) of W₁₀-PtNPs.



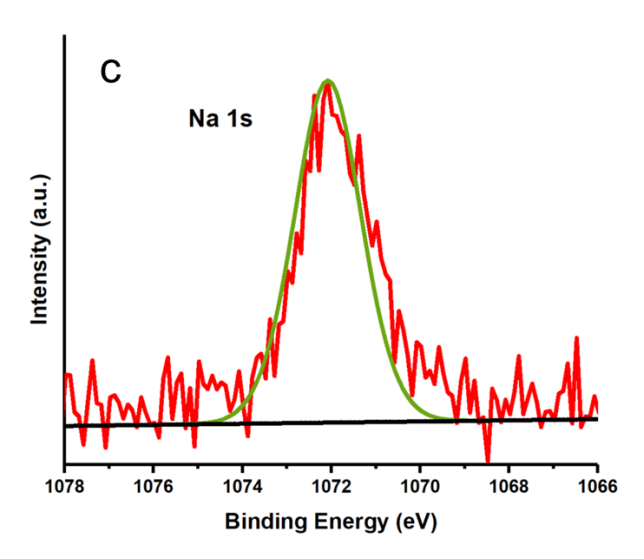


Figure 2.10. XPS of (a) Pt 4f, (b) W 4f, and (c) Na 1s in \mathbf{W}_{10} -PtNPs.

The POM: Pt ratio is also quantified by adding 1.0 g of solid KCl to 3.0 mL of **W**₁₀-**PtNP** solution. The addition of KCl salt precipitates the Pt(0) nanoparticles and frees the Pt-surface-bound decatungstate anions, resulting in a colorless solution with black Pt solids in the bottom. The weight of the precipitated black Pt solids after vacuum drying is 0.010 g. Understandably, these Pt solids could not be redissolved in fresh water because decatungstates are no longer present on their surfaces. The concentration of decatungstate in the colorless solution is then determined to be 1.3 mM based on its UV-Vis spectrum and the decatungstate UV-Vis standardization curves (Figure 2.11). Therefore, the POM: Pt ratio for **W**₁₀-**PtNPs** is calculated to be 0.08, which is in good agreement with the XPS-determined POM: Pt ratio (0.06) considering the potential uncertainties related to such small amounts of precipitated Pt solids.

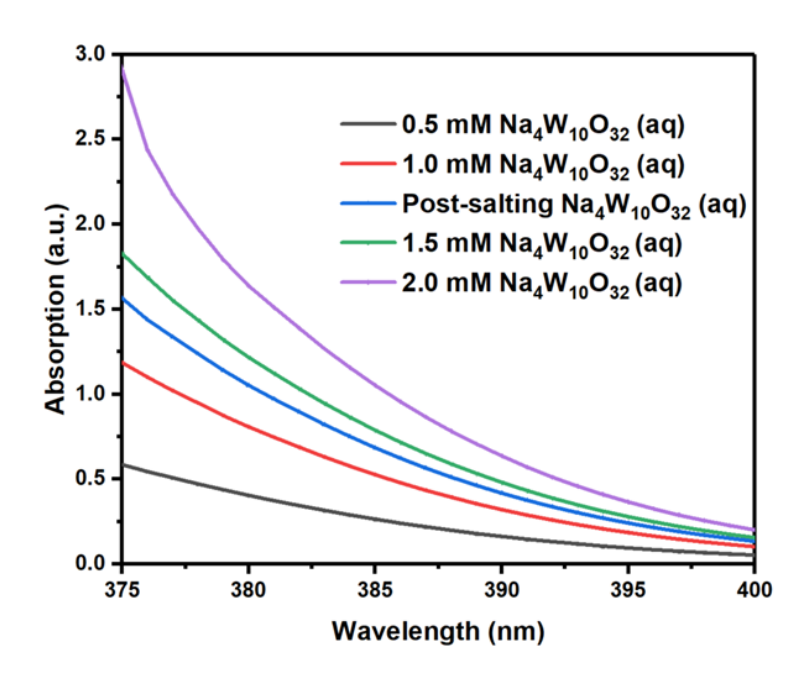


Figure 2.11. UV-Vis spectra of post-salting and standard decatungstate aqueous solution.

2.3.2 Reactivity and stability of W₁₀-PtNPs.

The photodehydrogenation of alkanes by **W**₁₀-**PtNPs** is conducted with these nanoparticles suspended in a solution of acetonitrile and alkane in which Na₄W₁₀O₃₂ is insoluble. This prevents dissociation of W₁₀O₃₂⁴⁻ from the Pt(0) surfaces. This lack of W₁₀O₃₂⁴⁻ dissociation is readily detected by UV-Vis spectroscopy because decatungstate has a very high absorbance in the UV region (see Figure 2.1). In contrast, Na₄W₁₀O₃₂ does dissociate from Pt when **W**₁₀-**PtNPs** are dissolved in an acetonitrile/water mixed solvent. Characterization of the latter system is given in the synthesis and characterization section. The experimental details of photocatalytic alkane dehydrogenation are described in the experimental section and Figure 2.12 shows the reactivity and recyclability of **W**₁₀-**PtNPs** for 2,3-dimethylbutane dehydrogenation to 2,3-dimethylbutene and hydrogen gas. As shown in Figure 2.12a, Na₄W₁₀O₃₂-stabilized Pt nanoparticles achieve over 40% alkane conversion rate while Na₄W₁₀O₃₂ and platinum black mixture only transforms ~10% of the alkane. Alkene and hydrogen are not detected for experiments without either Na₄W₁₀O₃₂ or platinum or light. The known side reaction of tetra-*n*-butyl ammonium cation oxidation to 1-butene and

tributylamine³⁰ is noticeably avoided in our system by using the sodium salt of decatungstate. These results demonstrate the superior alkane dehydrogenation activity of **W**₁₀-**PtNPs** and the indispensable role of Na₄W₁₀O₃₂, platinum, and light in the photocatalysis. The specific mechanism of the reaction will be discussed in the next section.

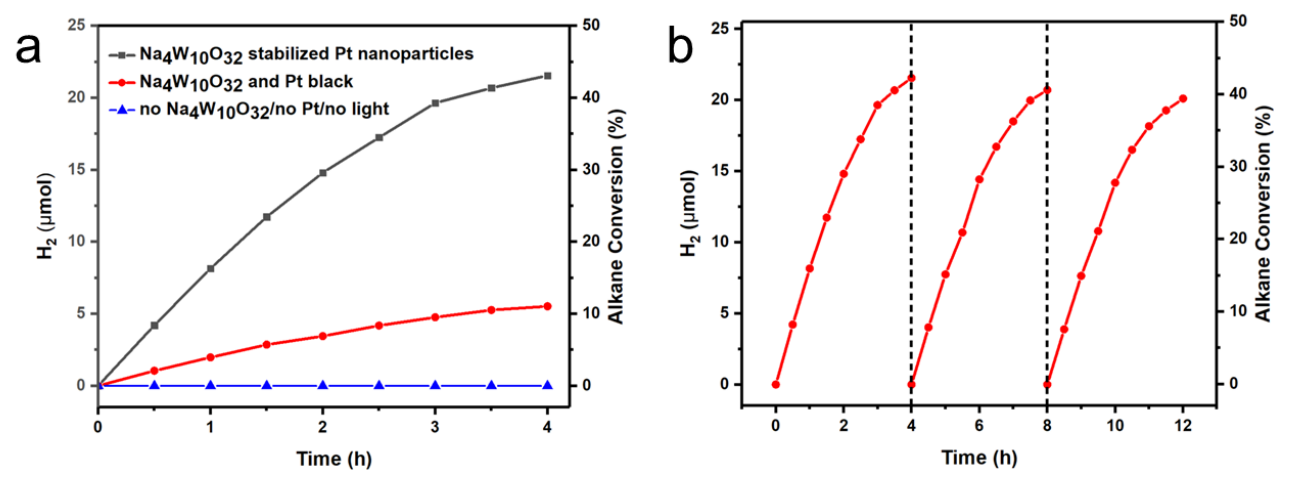


Figure 2.12. (a) Hydrogen evolution kinetics from photocatalytic dehydrogenation of 50 mM 2,3-dimethylbutane by W_{10} -PtNPs (black), a mixture of Na₄W₁₀O₃₂ and Pt black (red), and experiments without Na₄W₁₀O₃₂, Pt, and light, respectively (blue) in CH₃CN solution. (b) Recyclability test of W_{10} -PtNPs for photocatalytic 2,3-dimethylbutane dehydrogenation.

Stability of the **W**₁₀-**PtNP** solution was assessed by multiple methods. First, an acetonitrile-alkane solution of **W**₁₀-**PtNPs** shows no change after several months. There are no signs of aggregation. Second, we evaluated the recyclability of **W**₁₀-**PtNPs** after sequential photochemical alkane dehydrogenation reactions. Figure 2.12b shows that after 12 hours of continuous reactions, the activity of **W**₁₀-**PtNPs** remains almost the same. The small diminution in activity can be ascribed to catalyst loss during recycling. Third ,fourth, and fifth, TEM images (Figure 2.13), Fourier-transform infrared (FT-IR) spectra (500 to 1000 cm⁻1; Figure 2.14) , and XPS spectra (Figure 2.15) of **W**₁₀-**PtNPs** before and after photocatalytic alkane dehydrogenation showed no change, which indicates the integrity of decatungstates absorbed on the Pt surface.

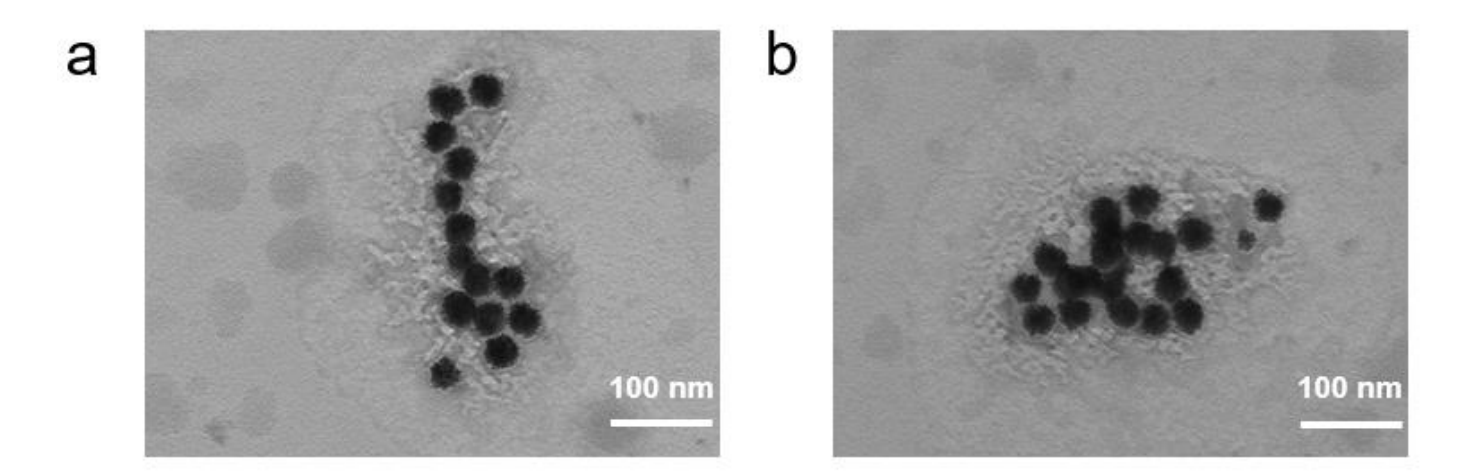


Figure 2.13. TEM images of **W**₁₀**-PtNPs** (a) before and (b) after 12 hours of continuous photochemical alkane dehydrogenation in acetonitrile.

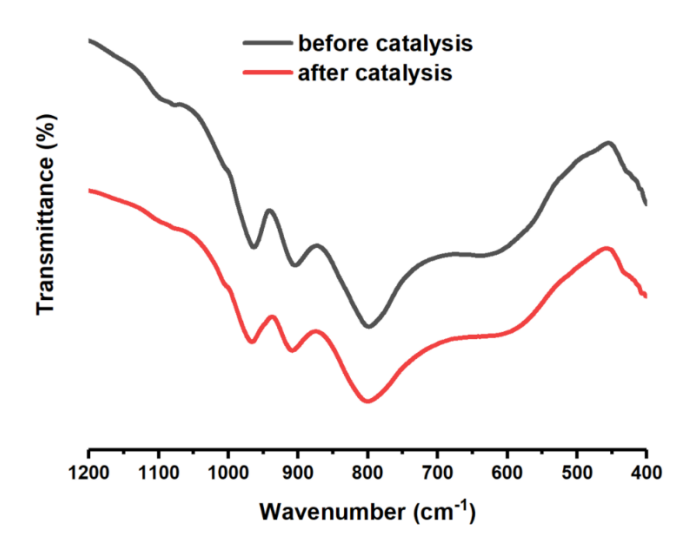
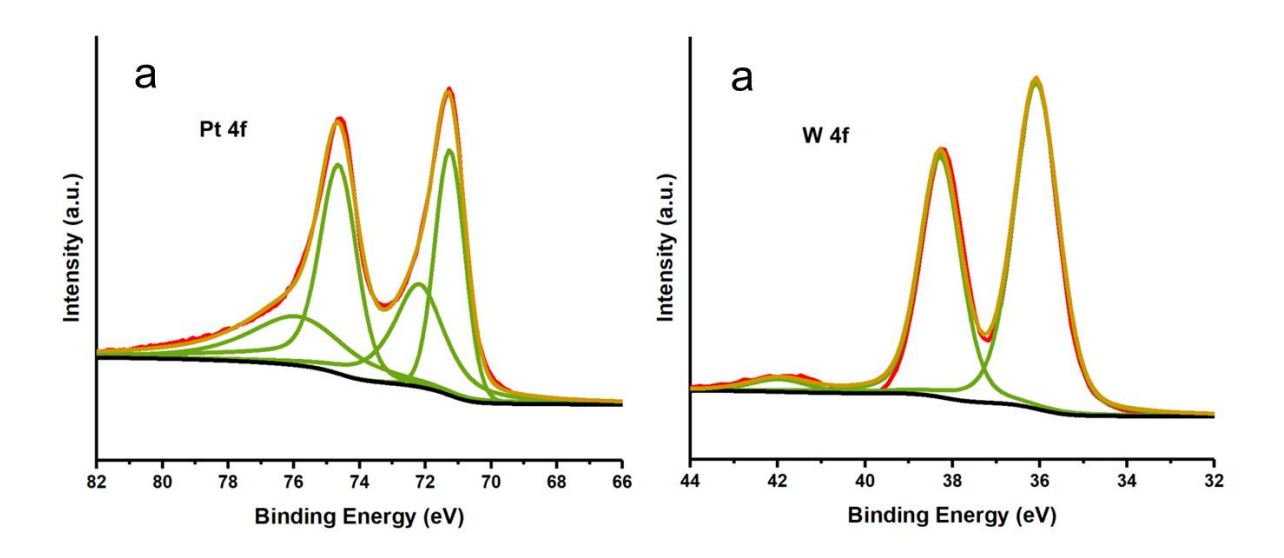


Figure 2.14. FT-IR spectra of **W**₁₀-**PtNPs** before (black) and after (red) 12 hours of continuous photochemical alkane dehydrogenation in acetonitrile.



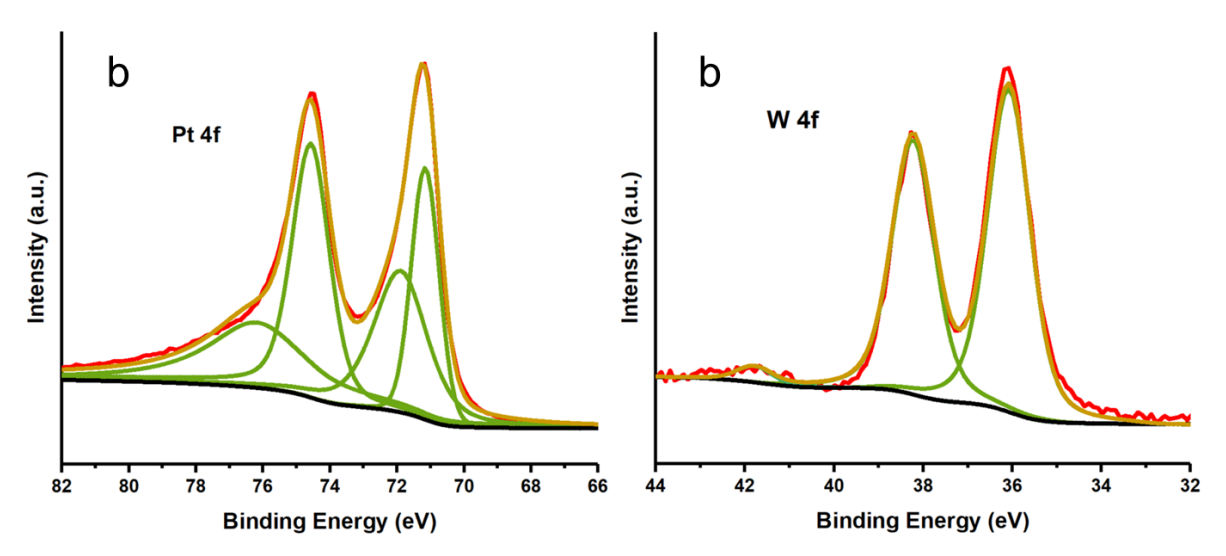


Figure 2.15. XPS spectra of Pt 4f and W 4f in **W**₁₀-**PtNPs** (a) before and (b) after 12 hours of continuous photochemical alkane dehydrogenation in acetonitrile.

Table 2.1 summarizes the product yields and quantum efficiencies for photocatalytic dehydrogenation of other alkanes by **W**₁₀-**PtNPs**. The alkene products were established by nuclear magnetic resonance (NMR) spectroscopies (Figure 2.16-18) and the quantum efficiencies and yields were calculated as described in the previous section. Significantly, the major products of alkane dehydrogenation are the non-thermodynamic (less-substituted) 1-alkenes. The logical explanation for these products is a kinetically-controlled alkane radical disproportionation reaction, where steric hindrance dictates that the hydrogen atom on the less substituted carbon atom is more likely to be abstracted. ¹² The quantum efficiencies and yields decrease in the order 2,3-dimethylbutane > cycloalkanes > n-alkanes, which is consistent with the decreasing disproportionation rates for tertiary, secondary, and primary radicals. ³¹ The higher yield of cyclooctene than cyclohexene can be explained by the lower heat of dehydrogenation of cyclooctane (+23.53 kcal/mol) than cyclohexane (+28.59 kcal/mol). ³²

Table 2.1. Photodehydrogenation of different alkanes catalyzed by **W**₁₀-**PtNPs** at ambient temperature with 365-nm light.

Substrate	Product	Quantum Efficiency	Yield
2,3-dimethylbutane	2,3-dimethyl-1-butene	0.20	42%
cyclohexane	cyclohexene	0.06	12%
cyclooctane	cyclooctene	0.10	21%
n-hexane	1-hexene	N/A	N/A
n-octane	1-octene	N/A	N/A

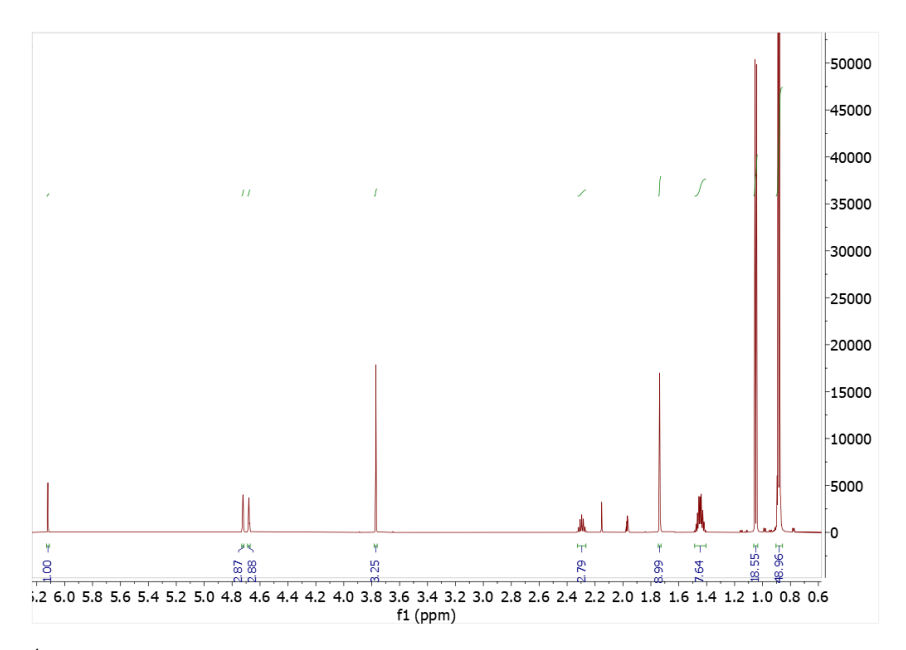


Figure 2.16. ¹H NMR spectrum of the acetonitrile-d₃ solution after 3 hours of photochemical dehydrogenation of 2,3-dimethylbutane. Internal standard: 1,3,5-trimethoxybenzene.

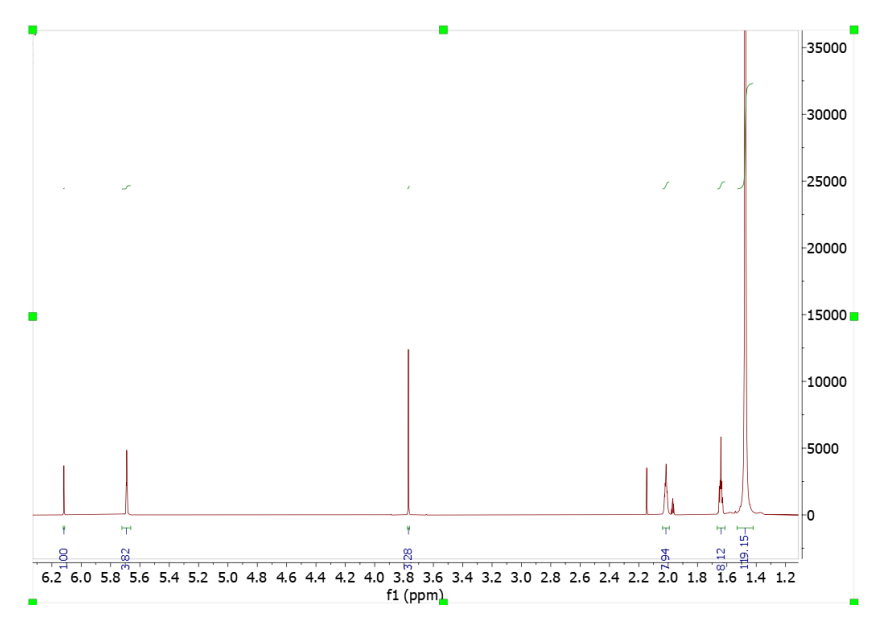


Figure 2.17. ¹H NMR spectrum of the acetonitrile-d₃ solution after 3 hours of photochemical dehydrogenation of cyclohexane. Internal standard: 1,3,5-trimethoxybenzene.

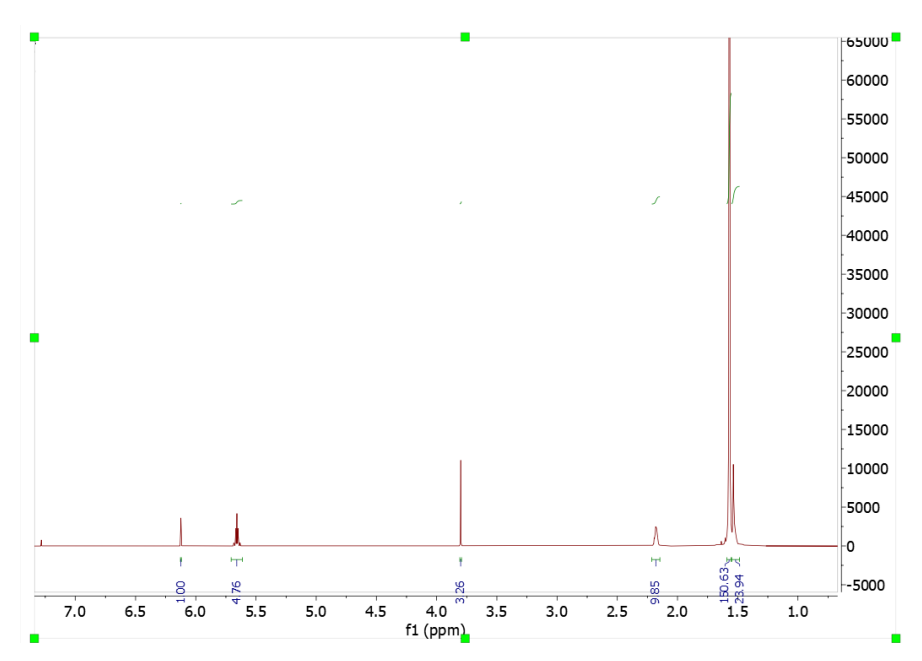


Figure 2.18. ¹H NMR spectrum of the chloroform-d solution after 3 hours of photochemical dehydrogenation of cyclooctane. Internal standard: 1,3,5-trimethoxybenzene.

2.3.3 Transient absorption spectroscopy

The mechanism of decatungstate anion ($W_{10}O_{32}^{4-}$) for photocatalysis has been discussed in our initial papers and subsequently by other groups. ³³⁻³⁵ In general, $W_{10}O_{32}^{4-}$ first absorbs ultraviolet light (i.e., 365 nm light) forming a ligand-to-metal charge transfer (LMCT) excited state ($[W_{10}O_{32}^{4-}]^*$). This excited state survives for ca. 30 ps and then decays with a quantum yield of around 0.5 to generate an oxyradical-like triplet state (termed as **wO**). This intermediate triplet state **wO** has a strong absorption around 780 nm and the lifetime for **wO** is measured to be 55 ± 20 ns. **wO** is chemically active and interacts with organic substrates, which leads to the one-electron-reduced form (H⁺)[$W_{10}O_{32}^{5-}$] and the corresponding organic radical.

2.3.4 Calculations

To properly describe the $Na_4W_{10}O_{32}$ complex (POM) and its interaction with a Pt nanoparticle computationally, we first modeled the solvent effects on the former by placing 12 acetonitrile (MeCN) molecules around $Na_4W_{10}O_{32}$ with three MeCN per Na^+ counterion.

The structures and complexation energies of these MeCN-solvated sodium cations are given in Figure 2.21. We used the long-range corrected B3LYP-GD3/6-31G(d)[Na-LANL2DZ] level of theory,³⁶ while all the electronic structure calculations were performed with Gaussian 16. It is evident that Na⁺ can coordinate up to six MeCN molecules at room temperature, yet for practical purposes. we find it efficient to use a three-coordinated Na⁺ ion that allows Na⁺ to bind with POM sites and permits large scale excited state calculations.

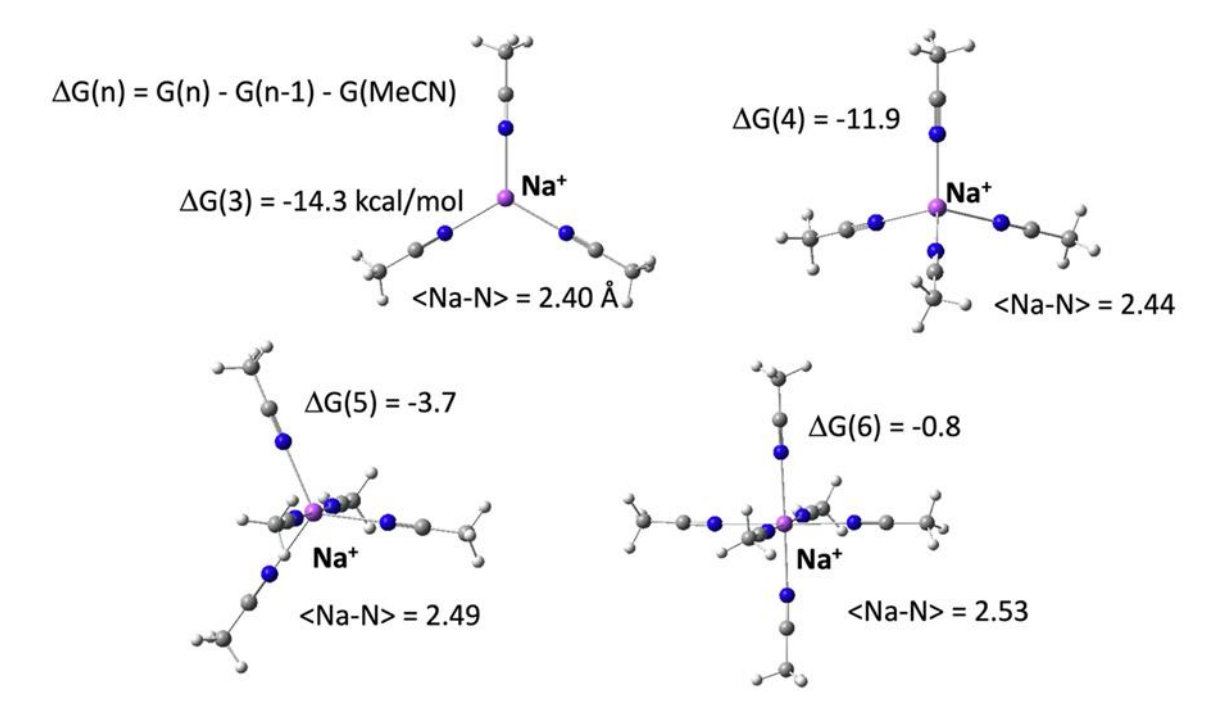


Figure 2.21. Graphic illustration of structures along with free energies of complexation (in kcal/mol) calculated at T = 298 K and 1 atm. The average Na-N distances (Å) are for a thermally stable solvated Na⁺ ion in explicit acetonitrile: Na⁺(MeCN)_n for n = 3 – 6. The level of electronic structure theory is B3LYP-GD3/6-31G(d)[Na-LANL2DZ].

Figure 2.22 shows the optimized structures of a "bare" $W_{10}O_{32}^{4-}$ POM and a charge neutral solvated (Na-3MeCN)₄W₁₀O₃₂. These were calculated by unconstrained energy minimization followed by a vibrational frequency analysis to confirm stability. We first analyzed the different oxygen types of the POM including their electron density distribution: the inner oxygens, O^{IN}, have -0.86 |e| charge; the O^{T1} and O^{T2} oxygens carry -0.63 and -0.60 charge, respectively; and the O^{B1}, O^{B2} and O^{B3} oxygens have -0.79, -0.81 and -0.87 charges,

respectively. Thus, the inner and the bridging oxygens carry an appreciably higher charge density than the terminal ones. Secondly, we note that in the POM structure complete with, MeCN-solvated Na+ counterions, the MeCN molecules remain fully attached to their respective Na+ centers with the average Na-N distance increasing from 2.40 to 2.45 Å. The Na-POM distances, as measured by the shortest Na-O distances, range from 2.3 to 2.7 Å. At the present level of solvation treatment, the Na+ counterions are in relatively close contact with the POM. Furthermore, the acetonitrile molecules form a well-defined hydrogen bonded network involving mainly the bridging oxygens with the various H...OB distances which span a range of 2.2 - 2.7 Å (dashed lines in Figure 2.22B). These interactions are consistent with the higher negative charges of the OB bridging oxygens than the OT terminal oxygens.

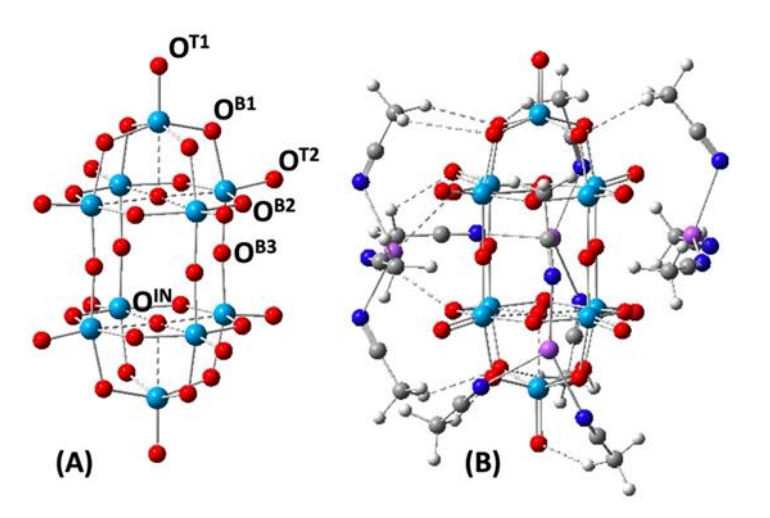


Figure 2.22. The optimized structures of the (**A**) "bare" $W_{10}O_{32}^{4-}$ POM (oxygen in red, tungsten in blue), and (**B**) charge neutralized solvated (Na-3MeCN)₄W₁₀O₃₂ complex. The POM oxygens are classified as follows: two internal O^{IN} (bonded to W by dashed lines); two axial terminal O^{T1}; eight lateral O^{T2}; eight type-1 and type-2 bridging O^{B1} and O^{B2}, respectively; and four central bridging O^{B3}. Notable features in (**B**) include the shortest Na-O distances, ranging from 2.3 to 2.7 Å. The level of theory is B3LYP-GD3/6-31G(d)[W,Na-LANL2DZ].

Following this step, molecular orbitals (MOs) and a UV-Vis spectrum of (Na-3MeCN)₄W₁₀O₃₂ were calculated and characterized. A brief inspection of the MOs reveals

the following; the few leading Lowest Unoccupied MOs, LUMO to LUMO-8, are pure W(5*d*) based orbitals. In contrast as expected, the few Highest Occupied MOs, HOMO to HOMO-3 are oxygen *p*-orbital in character: HOMO is comprised of O^{IN}, O^{B1}, O^{B3} with some contribution from O^{T1}/O^{T2}, while O^{B2} is not involved at all. HOMO-1 is dominated by O^{B2} and O^{B3} with a minor involvement of O^{IN} and O^{B1}. HOMO-2 is another case of a major O^{IN} centered MO with a small contribution from O^{B1} and O^{T1}, and HOMO-3 is primarily an O^{B1}/O^{B3}-based orbital. Therefore, as expected from the charge density, the occupied frontier MOs are dominated by the more charge negative (the inner and bridging) oxygens. A few representative MOs are presented in Figure 2.23.

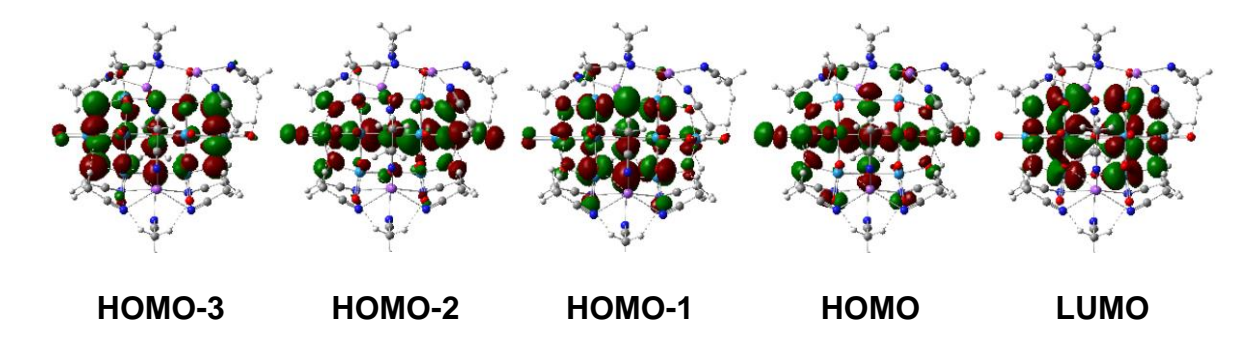
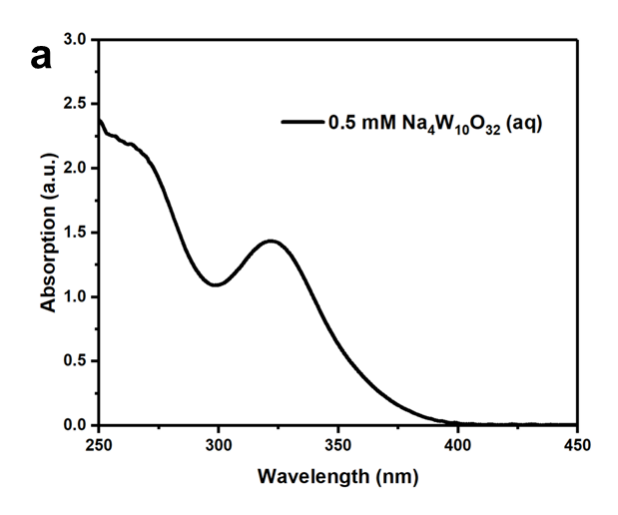


Figure 2.23. Orientation horizontal: the lowest four HOMO and LUMO orbitals of (Na-3MeCN)₄W₁₀O₃₂ calculated at the B3LYP-GD3/6-31G(d)[W,Na-LANL2DZ] level of theory.

The aforementioned UV-Vis spectrum, shown in Figure 2.24b, was calculated over a broad wavelength region, up to ~200 nm, using the time-dependent DFT formalism.³⁷ The line-shape exhibits two clearly separate bands: the weaker one appearing at ~340-360 nm, and the stronger one originating at ~300 nm and extending to the UV region below 220 nm (the cutoff threshold applied in the present calculations). The weak band is mainly a $O^{B1}(p)/O^{B3}(p)$ to W(5d) transition, while the strong band may best be characterized by mixed $O^{B1}(p)/O^{B2}(p)/O^{IN}(p)$ to W(5d) transitions. The laboratory measurement of aqueous $Na_4W_{10}O_{32}$ solution (Figure 2.24a) displays a band of 300-340 nm in reasonable agreement with the calculations.



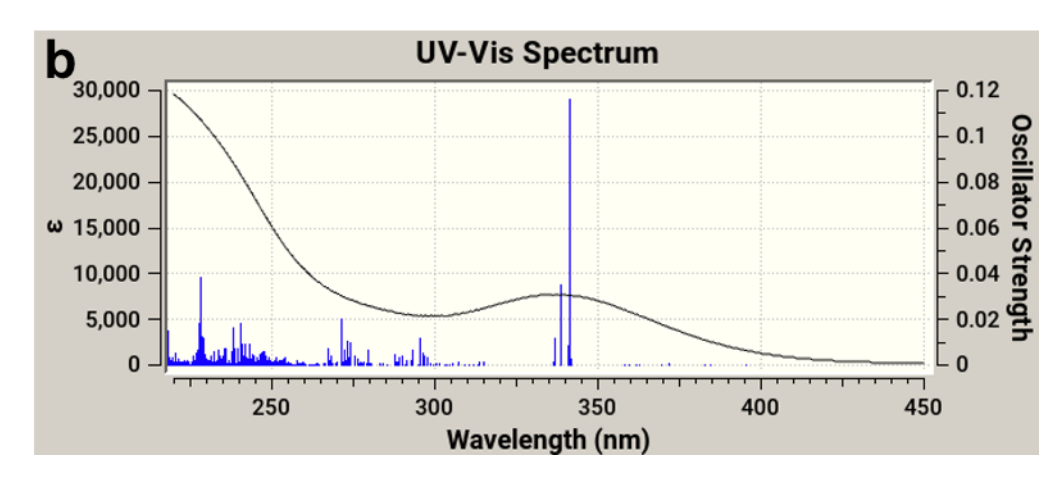


Figure 2.24. The UV-Vis spectrum of (a) 0.5 mM $Na_4W_{10}O_{32}$ aqueous solution in a 2 mm quartz cuvette and (b) (Na-3MeCN) $_4W_{10}O_{32}$ calculated with 600 singlets at the TD-B3LYP-GD3/6-31G(d)[W,Na-LANL2DZ] level of theory. The vertical blue lines are the optical S_0 -> S_n (n=1-600) intensities, and the smooth black line is a convoluted Lorentzian line-shape.

Interaction of the solvated POMs with the Pt nanoparticle was modeled using a number of small Pt_n clusters for n=12 - 79. Having exhausted most of our options after many exploratory calculations, we found it both computationally practical and physically realistic to use Pt_{19} given its size of ~8 Å. This is comparable to the "bare" POM, which is approximately a 6x6x12 Å cuboid. We note that others have observed recently that small Pt_n clusters with an average size n=12 are viable as interacting partners with MOFs. ³⁸ After initially relaxing Pt_{19} from its bulk structure, a series of geometry optimizations with the solvated POM produced an extremely stable complex, depicted in Figure 2.25. The electronic energy of

interaction relative to the separated (Na-3MeCN)₄W₁₀O₃₂ and Pt₁₉ fragments is ~5 eV. Ths is explained in part by a fairly close approach of Pt₁₉ to the O^{B3}, O^{B2} and O^{T2} centers of the POM, with the average Pt-O contact distance of ~2.2 Å. Additional interaction arises from the displaced MeCN solvent molecules that partly envelope Pt₁₉, which we presently consider as an artifact of the small nanoparticle model. Nevertheless, these findings support our experimental suppositions of a strong POM absorption on the Pt nanoparticle surfaces. Further information of the POM/Pt interaction can be extracted from an analysis of the frontier orbitals and the density of states, provided in Figures 2.26 and 2.27, respectively. There is a fair amount of orbital mixing in the HOMO (a Pt orbital) where a sizable density on an OB3 site is clearly visible. Similarly, the LUMO, which is a POM W(5d) orbital shares an appreciable overlap with Pt(5d). The density of states (DOS) spectra show that the addition of solvated counter-cations shifts the DOS down by ~10 eV without significantly changing the band gap (HOMO-LUMO gap), i. e. from 3.89 to 3.96 eV. The interaction with Pt₁₉ introduces a large block of 5d Pt orbitals in the gap region, thus formally reducing the gap to ~0.5 eV. This leads to multiple Pt-to-POM d-d transitions in the longer wavelength regions of the UV-Vis spectrum, as may be inferred from Figure 2.27.

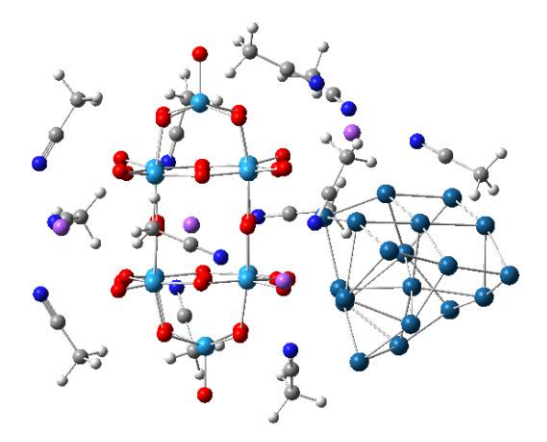


Figure 2.25. An optimized geometry of the strongly bound complex, $(Na-3MeCN)_4W_{10}O_{32}/Pt_{19}$, calculated using B3LYP-GD3/6-31G(d)[Pt,W,Na-LANL2DZ] level of theory. The interaction energy is ~5 eV, and the average Pt-O contact distance is ~2.2 Å.

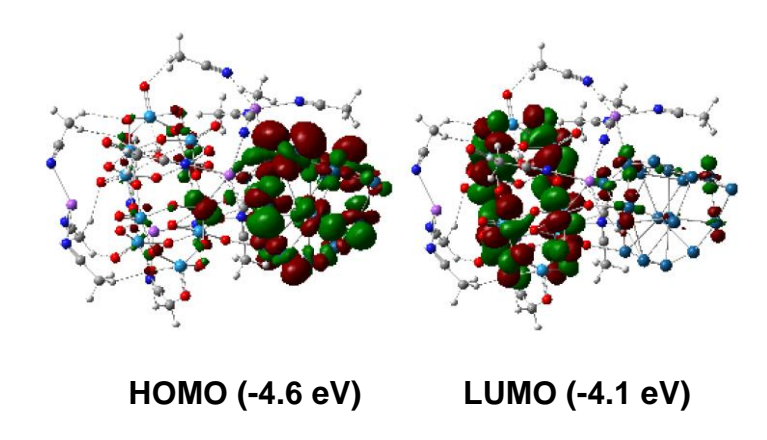


Figure 2.26. The two frontier orbitals of the $(Na-3MeCN)_4W_{10}O_{32}/Pt_{19}$ complex, calculated at the B3LYP-GD3/6-31G(d)[Pt,W,Na-LANL2DZ] level of theory.

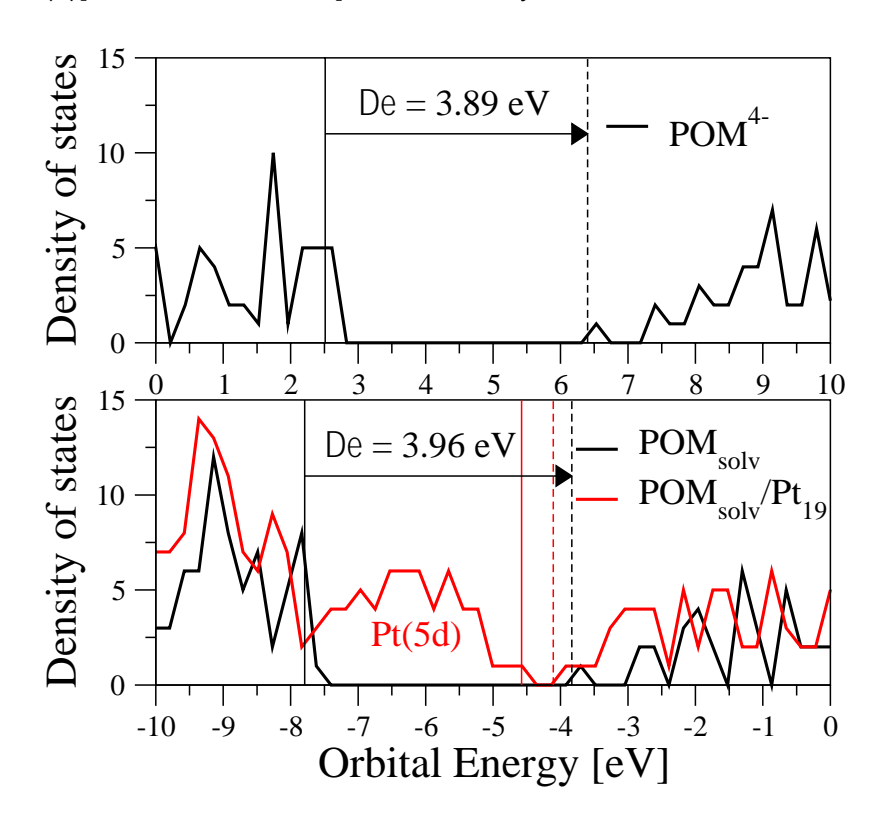


Figure 2.27. Density of MO states of the "bare" POM⁴⁻ (upper panel) and charge neutral and solvated (Na-3MeCN)₄W₁₀O₃₂ and its Pt complex (Na-3MeCN)₄W₁₀O₃₂/Pt₁₉ (lower panel). The vertical lines indicate the energy of the HOMO (solid line) and LUMO (dashed line). The bandgap $\Delta \varepsilon$ is given as the HOMO-LUMO energy difference.

2.4 Conclusions

1. Na₄W₁₀O₃₂-stabilized (~20 nm) Pt(0) nanoparticles (**W**₁₀-PtNPs) have been synthesized

through a photochemical method and characterized by UV-Vis spectroscopy, FT-IR spectroscopy, transmission electron microscopy, dynamic light scattering, and X-ray photoelectron spectroscopy. These W_{10} -PtNPs work as photocatalysts for alkane dehydrogenation at room temperature and are quite stable under turnover conditions.

2. W_{10} -PtNPs exhibit higher quantum efficiency and higher yield than a simple combination of Na₄W₁₀O₃₂ and platinum black for photochemical alkane dehydrogenation at room temperature. The transient absorption spectroscopy reveals that Pt perturbs the Na₄W₁₀O₃₂ excited state properties and calculations suggest strong interactions between decatung states and platinum clusters. The superior activity of **W**₁₀-PtNPs demonstrates the huge potential of polyoxometalate-stabilized metal nanoparticles for photocatalytic reactions.

2.5 References

- 1. Chen, S.; Chang, X.; Sun, G.; Zhang, T.; Xu, Y.; Wang, Y.; Pei, C.; Gong, J., Propane dehydrogenation: catalyst development, new chemistry, and emerging technologies. *Chem. Soc. Rev.* **2021**, *50* (5), 3315-3354.
- 2. Docherty, S. R.; Rochlitz, L.; Payard, P. A.; Coperet, C., Heterogeneous alkane dehydrogenation catalysts investigated via a surface organometallic chemistry approach. *Chem. Soc. Rev.* **2021**, *50* (9), 5806-5822.
- 3. Jiang, F.; Zeng, L.; Li, S.; Liu, G.; Wang, S.; Gong, J., Propane Dehydrogenation over Pt/TiO2–Al2O3 Catalysts. *ACS Catal.* **2015**, *5* (1), 438-447.
- 4. Goldman, A. S.; Roy, A. H.; Huang, Z.; Ahuja, R.; Schinski, W.; Brookhart, M., Catalytic Alkane Metathesis by Tandem Alkane Dehydrogenation— Olefin Metathesis. *Science* **2006**, *312*, 257-261.
- 5. Ahuja, R.; Punji, B.; Findlater, M.; Supplee, C.; Schinski, W.; Brookhart, M.; Goldman, A. S., Catalytic dehydroaromatization of n-alkanes by pincer-ligated iridium

- complexes. Nat. Chem. 2011, 3 (2), 167-171.
- 6. Yao, W.; Zhang, Y.; Jia, X.; Huang, Z., Selective catalytic transfer dehydrogenation of alkanes and heterocycles by an iridium pincer complex. *Angew. Chem., Int. Ed.* **2014,** *5*3 (5), 1390-1394.
- 7. Wang, Y.; Huang, Z.; Leng, X.; Zhu, H.; Liu, G.; Huang, Z., Transfer Hydrogenation of Alkenes Using Ethanol Catalyzed by a NCP Pincer Iridium Complex: Scope and Mechanism. *J. Am. Chem. Soc.* **2018**, *140* (12), 4417-4429.
- 8. Nomura, K.; Saito, Y., n-Alkene and Dihydrogen Formation from n-Alkanes by Photocatalysis using Carbonyl(chloro)phosphine-Rhodium Complexes. *J. Chem. Soc., Chem. Commun.* **1988**, 161-162.
- 9. Maguire, J. A.; Boese, W. T.; Goldman, A. S., Photochemical Dehydrogenation of Alkanes Catalyzed by trans-Carbonylchlorobis(trimethylphosphine)rhodium: Aspects of Selectivity and Mechanism. *J. Am. Chem. Soc.* **1989**, *111*, 7088-7093.
- 10. Chowdhury, A. D.; Weding, N.; Julis, J.; Franke, R.; Jackstell, R.; Beller, M., Towards a practical development of light-driven acceptorless alkane dehydrogenation. *Angew. Chem., Int. Ed.* **2014**, *53* (25), 6477-6481.
- 11. Lv, H.; Geletii, Y. V.; Zhao, C.; Vickers, J. W.; Zhu, G.; Luo, Z.; Song, J.; Lian, T.; Musaev, D. G.; Hill, C. L., Polyoxometalate water oxidation catalysts and the production of green fuel. *Chem. Soc. Rev.* **2012**, *41* (22), 7572-7589.
- 12. Renneke, R. F.; Pasquali, M.; Hill, C. L., Polyoxometalate Systems for the Catalytic Selective Production of Nonthermodynamic Alkenes from Alkanes. Nature of Excited-State Deactivation Processes and Control of Subsequent Thermal Processes in Polyoxometalate Photoredox Chemistry. *J. Am. Chem. Soc.* **1990**, *112*, 6585-6594.
- 13. Renneke, R. F.; Kadkhodayan, M.; Pasquali, M.; Hill, C. L., Roles of Surface

- Protonation on the Photodynamic, Catalytic, and Other Properties of Polyoxometalates

 Probed by the Photochemical Functionalization of Alkanes. Implications for Irradiated

 Semiconductor Metal Oxides. *J. Am. Chem. Soc.* **1991**, *113*, 8357-8367.
- 14. Renneke, R. F.; Hill, C. L., Homogeneous Catalytic Photochemical Functionalization of Alkanes by α-Dodecatungstophosphate. Rate Behavior, Energetics, and General Characteristics of the Processes. *J. Am. Chem. Soc.* **1988**, *110*, 5461-5470.
- 15. Renneke, R. F.; Hill, C. L., Selective Photochemical Dehydrogenation of Saturated Hydrocarbons with Quantum Yields Approaching Unity. *Angew. Chem., Int. Ed.* **1988,** 27, 1526-1527.
- 16. Schultz, D. M.; Levesque, F.; DiRocco, D. A.; Reibarkh, M.; Ji, Y.; Joyce, L. A.; Dropinski, J. F.; Sheng, H.; Sherry, B. D.; Davies, I. W., Oxyfunctionalization of the Remote C-H Bonds of Aliphatic Amines by Decatungstate Photocatalysis. *Angew. Chem., Int. Ed.* **2017**, *56* (48), 15274-15278.
- 17. Perry, I. B.; Brewer, T. F.; Sarver, P. J.; Schultz, D. M.; DiRocco, D. A.; MacMillan, D. W. C., Direct arylation of strong aliphatic C-H bonds. *Nature* **2018**, *560*, 70-75.
- 18. Sarver, P. J.; Bacauanu, V.; Schultz, D. M.; DiRocco, D. A.; Lam, Y. H.; Sherer, E. C.; MacMillan, D. W. C., The merger of decatungstate and copper catalysis to enable aliphatic C(sp³)-H trifluoromethylation. *Nat. Chem.* **2020**, *12* (5), 459-467.
- 19. Laudadio, G.; Deng, Y.; van der Wal, K.; Ravelli, D.; Nuño, M.; Fagnoni, M.; Guthrie, D.; Sun, Y.; Noël, T., C(sp³)–H functionalizations of light hydrocarbons using decatungstate photocatalysis in flow. *Science* **2020**, *369*, 92-96.
- 20. Sarver, P. J.; Bissonnette, N. B.; MacMillan, D. W. C., Decatungstate-Catalyzed C(sp³)-H Sulfinylation: Rapid Access to Diverse Organosulfur Functionality. *J. Am. Chem.* Soc. **2021**, *143* (26), 9737-9743.
- 21. Musgrave, C. B.; Olsen, K.; Liebov, N. S.; Groves, J. T.; Goddard, W. A.; Gunnoe,

- T. B., Partial Oxidation of Methane Enabled by Decatungstate Photocatalysis Coupled to Free Radical Chemistry. *ACS Catal.* **2023**, 6382-6395.
- 22. West, J. G.; Huang, D.; Sorensen, E. J., Acceptorless dehydrogenation of small molecules through cooperative base metal catalysis. *Nat. Commun.* **2015**, *6*, 10093.
- 23. Wang, Y.; Weinstock, I. A., Polyoxometalate-decorated nanoparticles. *Chem. Soc. Rev.* **2012**, *41* (22), 7479-7496.
- 24. Troupis, A.; Hiskia, A.; Papaconstantinou, E., Synthesis of Metal Nanoparticles by Using Polyoxometalates as Photocatalysts and Stabilizers. *Angew. Chem., Int. Ed.* **2002,** *41* (11), 1911-1914.
- 25. Maayan, G.; Neumann, R., Direct aerobic epoxidation of alkenes catalyzed by metal nanoparticles stabilized by the H₅PV₋₂Mo₁₀O₄₀ polyoxometalate. *Chem. Commun.* **2005,** (36), 4595-4597.
- 26. Guo, W.; Lv, H.; Chen, Z.; Sullivan, K. P.; Lauinger, S. M.; Chi, Y.; Sumliner, J. M.; Lian, T.; Hill, C. L., Self-assembly of polyoxometalates, Pt nanoparticles and metal–organic frameworks into a hybrid material for synergistic hydrogen evolution. *J. Mater. Chem. A* **2016**, *4* (16), 5952-5957.
- 27. Yamase, T.; Ishikawa, E., "Mixed-Valence Decatungstates" Revisited: Crystal Structure and Aqueous Solution Chemistry of [W₁₀O₃₂]⁶- and an ESR Study on Electron Delocalization. *Inorg. Chem.* **2022**, *61* (35), 13743-13755.
- 28. Chemseddine, A.; Sanchez, C.; Livage, J.; Launay, J. P.; Fournier, M., Electrochemical and Photochemical Reduction of Decatungstate: A Reinvestigation. *Inorg. Chem.* **1984**, 23, 2609-2613.
- 29. Hsu-Yao, T.; Browne, K. P.; Honesty, N.; Tong, Y. J., Polyoxometalate-stabilized Pt nanoparticles and their electrocatalytic activities. *Phys. Chem. Chem. Phys.* **2011**, *13* (16), 7433-7438.

- 30. Yamase, T.; Takabayashi, N.; Kaji, M., Solution Photochemistry of Tetrakis(tetrabutylammonium) Decatungstate(VI) and Catalytic Hydrogen Evolution from Alcohols. *J. Chem. Soc. Dalton Trans.* **1984**, 793-799.
- 31. Fischer, H.; Paul, H., Rate Constants for Some Prototype Radical Reactions in Liquids by Kinetic Electron Spin Resonance. *Acc. Chem. Res.* **1987,** *20*, 200-206.
- 32. Turner, R. B.; Meador, W. R., Heats of Hydrogenation. IV. Hydrogenation of Some cisand trans-Cycloolefins. *J. Am. Chem. Soc.* **1957,** *79*, 4133-4136.
- 33. Tzirakis, M. D.; Lykakis, I. N.; Orfanopoulos, M., Decatungstate as an efficient photocatalyst in organic chemistry. *Chem. Soc. Rev.* **2009**, *38* (9), 2609-2021.
- 34. Ravelli, D.; Protti, S.; Fagnoni, M., Decatungstate Anion for Photocatalyzed "Window Ledge" Reactions. *Acc. Chem. Res.* **2016**, *49* (10), 2232-2242.
- 35. Waele, V. D.; Poizat, O.; Fagnoni, M.; Bagno, A.; Ravelli, D., Unraveling the Key Features of the Reactive State of Decatungstate Anion in Hydrogen Atom Transfer (HAT) Photocatalysis. *ACS Catal.* **2016**, *6* (10), 7174-7182.
- 36. Grimme, S.; Antony, J.; Ehrlich, S.; Krieg, H., A consistent and accurate ab initio parametrization of density functional dispersion correction (DFT-D) for the 94 elements H-Pu. *J. Chem. Phys.* **2010**, *132* (15), 154104.
- 37. Bauernschmitt, R.; Ahlrichs, R., Treatment of electronic excitations within the adiabatic approximation of time dependent density functional theory. *Chem. Phys. Lett.* **1996,** *256*, 454-464.
- 38. Kratzl, K.; Kratky, T.; Gunther, S.; Tomanec, O.; Zboril, R.; Michalicka, J.; Macak, J. M.; Cokoja, M.; Fischer, R. A., Generation and Stabilization of Small Platinum Clusters Pt_{12±x} Inside a Metal-Organic Framework. *J. Am. Chem. Soc.* **2019**, *141* (35), 13962-13969.

Chapter 3:

Polyoxometalate-Stabilized Gold Nanoparticles for Electrochemical Carbon Dioxide Reduction

Abstract

The electrochemical carbon dioxide reduction reaction (CO2RR) is an attractive and sustainable method for storage of renewable energy in fuels or value-added chemicals, such as carbon monoxide (CO), hydrocarbons, and alcohols. In this chapter, phosphotungstate (PW₁₂O₄₀³⁻) stabilized gold nanoparticles (PW₁₂-AuNPs) are synthesized by a photochemical method and deposited on electrodes for electrochemical CO2RR. Citrate stabilized gold nanoparticles (citrate-AuNPs) are also synthesized and tested for comparison. The electrocatalytic performance of PW₁₂/citrate-AuNPs for CO₂ reduction is evaluated in a CO₂ saturated acetonitrile (CH₃CN) solution containing 0.10 M [n-Bu₄N]PF₆ and 0.5% (v/v) H₂O. The results show that PW₁₂-AuNPs can catalyze the reduction of CO₂ to CO with an onset potential of -1.70 V versus Fc^{+/0}, which is 0.60 V more negative than the estimated reversible potential (-1.10 V) for this process. Faradaic efficiencies of around 70% for CO are obtained over a wide range of applied potentials. Cyclic voltammograms of TBA₃PW₁₂O₄₀ in acetonitrile under argon and CO2 atmosphere reveal no difference and citrate-AuNPs exhibit similar activity for CO2 reduction under the same condition. Other POM-stabilized gold nanoparticles have also been examined with no obvious enhancement compared to citrate-AuNPs. These results suggest that POMs may not act as efficient electrocatalysts for CO₂RR.

3.1 Introduction

The world economy has depended on fossil fuel energy sources since the Industrial Revolution. The accompanying sharp increase of carbon dioxide (CO₂) emission triggers serious environmental and climate problems (extreme weather, ocean acidification, species

extinction, etc.). According to recent reports, global CO₂ emission currently is ca. 37 Gt with 30.4 Gt related to fossil fuels and is predicted to increase to 36~43 Gt by 2035.¹ The atmospheric level of CO₂ has risen from 270 ppm in the preindustrial era to nearly 425 ppm in 2023, which far exceeds its natural fluctuation (d = 180~300 ppm) over the past millions of years.² Consequently, there is an urgent need to reduce the deep dependence on fossil fuels and achieve zero-carbon emissions without hurting economic growth. Since the "Paris Agreement" set a goal of net zero emissions, more and more countries are transforming this paradigm into national strategies. For example, China has pledged to cut net carbon emissions to zero by 2060. The European Union, Japan, and India have set similar targets. At the same time, the growing domination and falling price of renewable electricity make the electrocatalytic carbon dioxide reduction reaction (CO₂RR) a promising option to address the increasing CO₂ crisis. Its use could not only help close the carbon cycle by mitigating CO₂ emissions, but also allow storage of electrical energy in the form of chemical feedstocks and fuels.³

Since CO₂ is a linear molecule with relatively high thermodynamic stability due to its much higher bond energy of C=O (750 kJ/mol) compared with that of C-C (336 kJ/mol), C-O (327 kJ/mol), and C-H (411 kJ/mol), the CO₂ reduction reaction usually demands multiple energy inputs to break the C=O bonds. Tremendous efforts have been made to achieve efficient electrocatalytic CO₂ reduction processes⁴⁻¹¹ and POMs are attractive candidates to promote the multi-proton/multielectron reduction of CO₂ to useful chemicals due to their proton- and electron-storage properties. In 1998, Kozik and co-workers studied the interaction of CO₂ with transition-metal-substituted heteropolyanions in nonpolar solvents.¹²

It was found that the α-Keggin structure could reversibly form complexes with CO₂ when substituted with Co(II), Ni(II), and Mn(II) and traces of water are necessary for the reactions to take place. On basis of these previous fragmented research works, Proust et al. proposed the first systematic investigation of electrocatalytic CO2 reduction by a POM homogeneous catalyst, $(TOA)_6[\alpha-SiW_{11}O_{39}Co(\cdot)]$ (TOA = tetraoctyl ammonium), in 2015. The "(\(\text{ }\)" denotes a vacant coordination position on the cobalt center. 13 It was demonstrated that the electrolysis of a CO₂-saturated dichloromethane solution in the presence of the (TOA)₆[α-SiW₁₁O₃₉Co()] could lead to the formation of CO. By adding acid and water into POM solution for electrolysis under CO₂, CO was produced continuously to reach 37 µmol after 66 h of electrolysis. In addition, formaldehyde could be detected without H2 or other CO2 reduction products. Although the proposed POM catalyst showed low faradic yield, this research suggested that (TOA)₆[α-SiW₁₁O₃₉Co(_)] was capable of fairly selective electrocatalytic reduction of CO₂ to CO with simultaneous four-electron/four-proton reduction to formaldehyde. Proust et al. also studied a new organometallic derivative of POMs, (TBA)₃[α-H₂PW₁₁O₃₉-{Rh^{III}Cp*(OH₂)}], presenting an accessible coordination site on the Rh^{III} center, for electrocatalytic reductions.¹⁴ The electro-assisted reduction of CO₂ in the presence of water as a proton source mainly led to the catalytic formation of hydrogen, with formic acid being a minor product. Very recently, Neumann et al. synthesized several tri-lacunary polyoxometalates with three first-row transition metals Fe^{III}, Ni^{II}, and Cu^{II} in various combinations placed in nearest neighbor positions. The metal centers in these polyoxometalates mimicked natural carbon monoxide dehydrogenase (CODH) enzymes. All of the studied polyoxometalates displayed both CO2 reduction and CO oxidation activity while the tri-copper-substituted compound, {SiCu₃W₉},

was most active for CO₂-to-CO reduction in acetonitrile with the highest turnover frequency (TOF) and lowest overpotential.¹⁵ UV/Vis spectroelectrochemical measurements confirmed the reduction of Cu(II) to Cu(I) instead of W(VI) to W(V) in these POMs at negative potentials and Raman spectroscopy further revealed the carbonyl intermediates during electrochemical CO₂ reduction.

POMs constitute a well-defined library of inorganic nanoscale building blocks with oxygen-rich surfaces. As such they are attractive candidates for the design and construction of tailored framework materials. 16 Based on previous research findings, Lan and co-workers developed a series of precisely designed polyoxometalate-metalloporphyrin organic frameworks for electrocatalytic CO₂ reduction. The special structural design involving the integration of {ε-PMo₈VMo₄VIO₄₀Zn₄} and the metalloporphyrin endowed the proposed M-PMOFs (M = Co, Fe, Ni, Zn) with excellent electron collection and donation properties that are vital to multiple-electron CO2 reduction processes. The Co-PMOF catalyst exhibited a remarkable faradaic efficiency of 94% over a wide potential range from -0.8 to -1.0 V with the faradaic efficiency reaching 99%, the highest in reported metal organic frameworks to date. The Co-PMOF also showed a high TOF of 1656 h⁻¹ and excellent catalysis stability up to 36 h of continuous testing. DFT calculations were performed to understand the highly active as well as selective reaction mechanism of Co-PMOF. The assembly of Zn-ε-Keggin POM and Co-TCPP resulted in the decreased ΔG for the rate-determining steps with the formation of adsorbed intermediates *COOH and *CO during CO2 reduction. The computational results proved that the Co atom in Co-TCPP and not POM ligand was the active site, in addition to establishing that a synergy exists between the POM and the porphyrin metal center with respect to electron transfer.

At the same time, the photocatalytic reduction of CO₂ to carbonaceous fuels is appealing because solar energy is clean and inexhaustible. Major research has revealed many effective photocatalysts and their corresponding systems. 18-22 In addition, POMs have been integrated into such systems because of their fast, reversible, stepwise and largely controllable electrontransfer reactions without degradation of the POM structure. Neumann and co-workers first polyoxometalate Keggin structure substituted with Rull, reported а of the $\{(C_6H_{13})_4N\}_5[Ru^{|||}(H_2O)SiW_{11}O_{39}],$ that catalyzed the photoreduction of CO₂ to CO in 2010.²³ This study demonstrated that in the presence of (CH₃CH₂)₃N, the mildly nucleophilic O atom of CO₂ coordinates to the Ru(III) center of the POM leading to formation of a O₂C-NMe zwitterion stabilized by both Ru-O and C-N interactions. The amine has a promotional effect on the activation of CO₂ by [Ru^{III}(H₂O)SiW₁₁O₃₉]⁵. The detailed mechanistic pathway for photoreduction of CO₂ was also predicted and provided, in which the POM took part in the activation of both CO2 and (CH3CH2)3N. Subsequently, Poblet and co-workers performe detailed DFT and TD-DFT calculations on the mechanism of photoreduction of CO2 to CO by the Re-organic hybrid POMs $\{NaH[PW_{12}O_{40}]^3-Re^{I}L(CO)_3DMA\}^{n-}$ (L = 15-crown-5phenanthroline, DMA = N,N-dimethylacetamide).²⁴ The proposed reaction mechanism can be divided into several steps, including photoexcitation and charge transfer, DMA release, CO₂ addition, protonation, CO release then recoordination of DMA. The charge transfer states in the POM-Re complex, involve metal-centered excitations occurring in the reduced POM that lead to one-electron transfer to the organometallic unit from the excited POM, then Re can bind and activate the CO₂ substrate. No quantum yields were measured. Subsequent steps involving protonation of CO₂ and CO release are thermodynamically favorable and are induced by a second electron transfer from the POM to the *Re* complex. In this system, the POM acts as the photosensitizer, electron reservoir, as well as electron donor. More recently, Lan et al. reported the synthesis of two phosphate (PO₄³-)-centered polyoxo-titanium clusters (PTCs), PTi₁₆ and PTi₁₂, which display the classic heteroatom-centered Keggin structure and its trivacant structures, respectively.²⁵ These POMs absorb UV light and catalyze CO₂ reduction by triethanolamine (TEOA) as the electron donor in acetonitrile. HCOOH was the main reaction product generated with a selectivity of 93.4% and 83.9% for PTi₁₆ and PTi₁₂, respectively. The electron spin resonance (ESR) spectra confirmed the existence of Ti³⁺ during UV irradiation, which suggested that the Ti⁴⁺ within titanium—oxo clusters was reduced to Ti³⁺ by receiving photoexcited electrons transferred from O²⁻ centers while the corresponding photo-generated holes were quenched by TEOA. Subsequently, the Ti³⁺ donated electrons to the absorbed CO₂ for HCOOH production regenerating Ti⁴⁺.

The idea of POM acting as an electron "shuttle" during photochemical CO₂ reduction reaction has been explored with well-known photocatalysts. For example, Wang and Su et al. reported a noble-metal-free POM (Na₁₀Co₄(H₂O)₂(PW₃O₃₄)₂, Co₄) with oxidative ability that was combined with g-C₃N₄ to form inexpensive hybrid materials (Co₄@g-C₃N₄). The resulting composite catalysts showed a higher activity for CO₂ reduction to CO than bare g-C₃N₄ with a highest yield reaching 107 μmol g⁻¹ h⁻¹ under visible-light irradiation (λ≥₄20 nm) as well as high selectivity for CO production (9⁴%). After 10 h of visible-light irradiation, the yield of CO reached 896 μmol g⁻¹. Mechanistic analysis revealed that Co₄ facilitates charge transfer involving g-C₃N₄ and increases the catalytic oxidative ability of the surface.²6 Neumann et al.

prepared a three-component construct including g-C₃N₄ as a visible-light photoactive semiconductor, a polyoxometalate (H₃PW₁₂O₄₀) that functions as an electron acceptor to improve hole-electron charge separation and an electron donor to a rhenium-based CO₂ reduction catalyst.²⁷ Upon photoactivation of g-C₃N₄, a cascade is initiated by dehydrogenation of hydrocarbons coupled to the reduction of the polyoxometalate. Visiblelight photoexcitation of the reduced polyoxometalate enables electron transfer to the rheniumbased catalyst which selectively reduces of CO₂ to CO. As in electrocatalytic CO₂RR, the POM-incorporated framework materials have shown remarkable photocatalytic activity for CO₂RR. Lan et al. designed and synthesized a polyoxometalate metal organic framework (NNU-29) with a hydrophobic ligand and ε-{Zn₄PMo₁₂O₄₀} as a heterogeneous catalyst for photocatalytic reduction of CO₂.²⁸ NNU-29 after 16 h illumination in the water selectively produces formic acid in 97.9% yield with the hydrophobic group hindering the competitive hydrogen generation reaction. Lan's group further developed a covalent organic framework (COF) with uniformly dispersed POMs through confining POM cluster in the regular nanopores of the COF by covalent linkages. These COF-POM composites combine the properties of light absorption, electron transfer, and catalysis at well-defined active sites. The best COF-POM photocatalyst achieved a CO yield of 37.25 µmol g⁻¹ h⁻¹ with ca. 100% selectivity.29

Based on the above research, I initially assessed whether dicopper-substituted POMs might be effective for CO₂ reduction because there were reports of binuclear copper organometallic CO₂RR catalysts generating oxalates products.^{30, 31} These products are noteworthy considering most homogenous CO₂RR catalysts only form C₁ products (CO,

HCOOH, CH₃OH, CH₄, etc.).^{32, 33} I synthesized a dicopper-substituted silicotungstate ([y- $H_2SiW_{10}O_{36}Cu_2(\mu-1,1-N_3)_2]^{4-}$) using a literature procedure^{34, 35} and tested its catalytic activity for CO₂RR. The results were negative, and I found a study by another group that couldn't reproduce the experiments in reference 30. Recently, reference 31 was also retracted by the original authors because they demonstrated that the true origin of the claimed oxalate product involved oxidation of ascorbate by oxygen. These further developments suggest that dicopper-substituted POMs may not be able to reduce CO₂ to oxalate or any other product. Then I prepared and evaluated the molecular thiomolybdate ([Mo₃S₁₃]²⁻) as a possible CO₂RR catalyst since its heterogeneous form, i.e. molybdenum sulfide, is a well-established CO₂RR electrocatalyst. 36-38 Unfortunately, both electrochemical and photochemical experiments failed to yield CO₂ reduction products likely due to the high activity of [Mo₃S₁₃]²- for the hydrogen evolution reaction (HER).^{39, 40} The latter almost always competes with CO₂ reduction. also checked the **POMs** copper-containing $([\{Cu_2(OH_2)_2\}_2\{Cu(OH_2)_2\}_4P_8W_{48}O_{176}(OCH_3)_8]^{16-}$ and $([Cu_{20}CI(OH)_{24}(H_2O)_{12}(P_8W_{48}O_{184})]^{25-})^{41,}$ ⁴² and the niobium-containing POMs, [Nb₄V₂O₁₉]⁸⁻ and [Nb₂V₄O₁₉]⁸⁻, and all these failed to catalyze CO2RR as well. As a consequence, I discontinued the above exploration and focused on polyoxometalate-stabilized metal nanoparticles (POM-Metal NPs) as these metals (e.g., Au, Ag, and Cu) are well-known electrocatalysts for CO₂RR.⁴³⁻⁴⁷ To the best of our knowledge, such POM-Metal NPs have never been reported as electrocatalysts for CO₂RR and warrant extensive study.

3.2 Experimental

3.2.1 General Materials and Methods

Materials and solvents were purchased as ACS analytical or reagent grade and used as received. The purity of the H₃PW₁₂O₄₀·12H₂O (PW₁₂) was verified by the Fourier transform infrared (FT-IR) (Figure 3.12) and the water content was determined by thermogravimetric analysis (TGA) (Figure 3.13). The FT-IR spectra were collected on a Nicolet TM 600 FT-IR spectrometer by the attenuated total reflectance (ATR) sampling technique. UV-vis spectra were collected with an Agilent 8453 spectrophotometer using a 1.0 cm optical path length quartz cuvette. Dynamic light scattering (DLS) data were acquired on a NanoPlus DLS Particle Size Analyzer instrument (Particulate Systems, Norcross, GA). Transmission electron microscopy (TEM) measurements were conducted on a Hitachi H-7500 transmission electron microscope at an accelerating voltage of 80 kV in the Robert P. Apkarian Integrated Electron Microscopy Core at Emory University. SEM-EDX data were collected on a HITACHI SU8230 FE-SEM at an accelerating voltage of 10/30 kV in the Institute of Electronics and Nanotechnology at Georgia Institute of Technology. The thermogravimetric analysis (TGA) data were collected on a Mettler Toledo TGA instrument. X-ray photoelectron spectroscopy (XPS) were conducted on a thermos K-ALPHA XPS instrument. Gas chromatography (GC) analysis of the gas phase was performed using an Agilent 7890 gas chromatograph with a 5 Å molecular sieve column, a thermal conductivity detector, and argon carrier gas. Gas chromatography (GC) analysis of the liquid phase was performed on a Hewlett-Packard 6890 instrument with a 5% phenyl methyl silicone capillary column, a flame ionization detector, a Hewlett-Packard 3390A series integrator using N₂ as the carrier gas.

3.2.2 Electrochemistry

Cyclic voltammograms (CVs) and bulk electrolysis data were obtained using a BAS CV-50W electrochemical analyzer and conducted at room temperature (25 ± 2 °C). CVs were recorded in a standard three-electrode electrochemical cell with a glassy carbon disk working electrode, a platinum wire counter electrode and Ag/Ag⁺ (0.01 M AgNO₃ in CH₃CN) reference electrode using 0.1 M tetrabutylammonium hexafluorophosphate (n-Bu₄NPF₆) as the supporting electrolyte. PW₁₂-AuNPs/Citrate-AuNPs were mixed with Nafion solution and dispersed in ethanol to prepare the catalyst ink that was drop-coated on the working electrode. The scan rate used in voltametric experiments was 100 mV/s. The measured potential was converted to the Fc⁺/Fc⁰ scale using data measured from CV for 1.0 mM ferrocene (Fc). PW₁₂-AuNPs/Citrate-AuNPs deposited glassy carbon electrode/carbon paper electrode was used as a working electrode in bulk electrolysis and the working and counter electrodes were separated by porous glass frits. Bulk electrolysis was conducted in a three-necked 50 mL round bottom flask equipped with airtight adapters and purged with argon gas prior to use. The headspace and solution phase after bulk electrolysis was then analyzed by GC as described in the method section.

3.3 Results and Discussion

3.3.1 Synthesis and characterization of PW₁₂-AuNPs/Citrate-AuNPs.

The synthesis of the PW₁₂-AuNPs is similar to the synthesis of W₁₀-PtNPs (Chapter 2 of this thesis), which involves preparing 15 mL deaerated aqueous solution of 0.20 mM AuCl₃, 0.70 mM H₃PW₁₂O₄₀, and 0.50 M reducing agent 2-propanol which was then irradiated with a 365 nm LED light. The phosphotungstate (PW₁₂O₄₀³-) absorbs light to the excited state,

which oxidizes the 2-propanol to produce dark-blue reduced POM. The reduced phosphotungstate then reacts with Au (III), forming Au (0) nanoparticles which immediately absorb the unreacted/re-oxidized ground state phosphotungstate (PW₁₂O₄₀³⁻). The pH of the solution stays at 2 throughout the synthesis so that the integrity of PW₁₂O₄₀³⁻ is maintained because PW₁₂O₄₀³⁻ is known to hydrolyze at higher pH to form the well-defined lacunary phosphotungstate such as PW₁₁O₃₉⁷⁻ (PW₁₁), PW₁₀O₃₇⁹⁻ (PW₁₀), and PW₉O₃₄⁹⁻ (PW₉). The UV-Vis spectra of H₃PW₁₂O₄₀, one-electron reduced H₃PW₁₂O₄₀, and H₃PW₁₂O₄₀-stabilized Au nanoparticles (PW₁₂-AuNPs) are shown in Figure 3.1. The one-electron reduced H₃PW₁₂O₄₀ has two strong absorption bands located at around 500 nm and 750 nm, which correspond to inter-valence charge transfer transitions.^{48, 49} The H₃PW₁₂O₄₀-stabilized Au nanoparticles (PW₁₂-AuNPs) have a characteristic surface plasmon resonance (SPR) with the absorption maximum at 526 nm. The transmission electron microscopy (TEM) image (Figure 3.2) and the dynamic light scattering data (Figure 3.3) reveal that the average size of PW₁₂-AuNPs is around 20 nm.

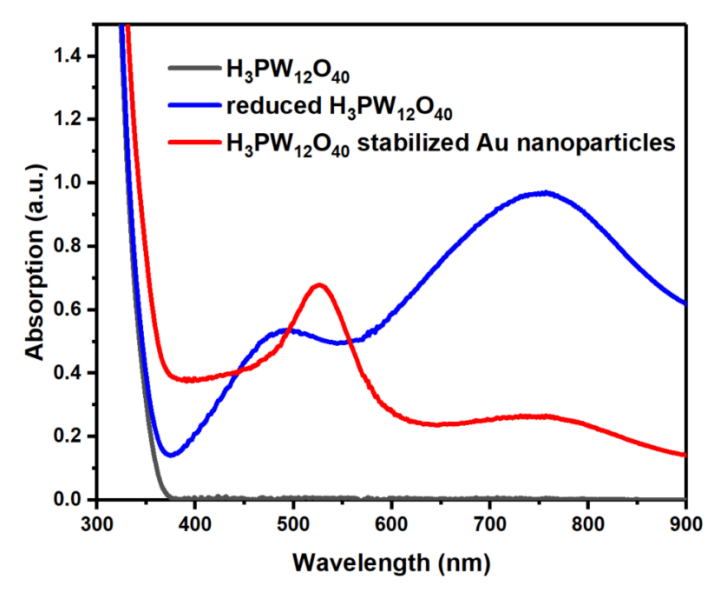


Figure 3.1. UV-Vis spectra of 0.70 mM aqueous solutions of $H_3PW_{12}O_{40}$ (black), one-electron reduced $H_3PW_{12}O_{40}$ (blue), and the PW_{12} -AuNPs (red).

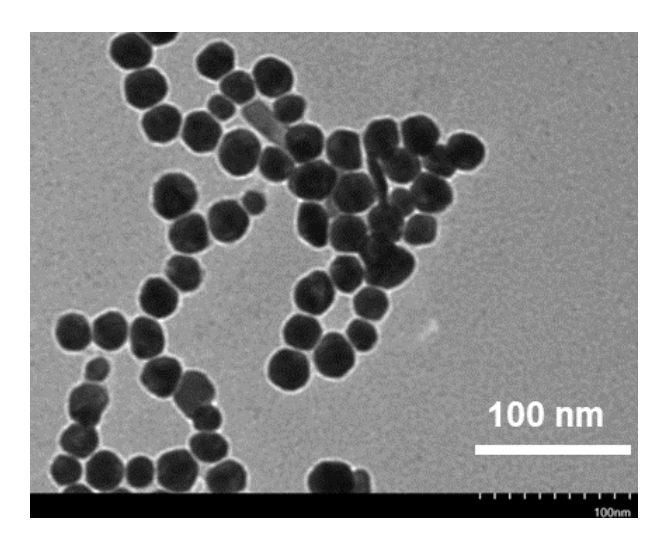


Figure 3.2. Transmission electron microscopy (TEM) image of PW₁₂-AuNPs.

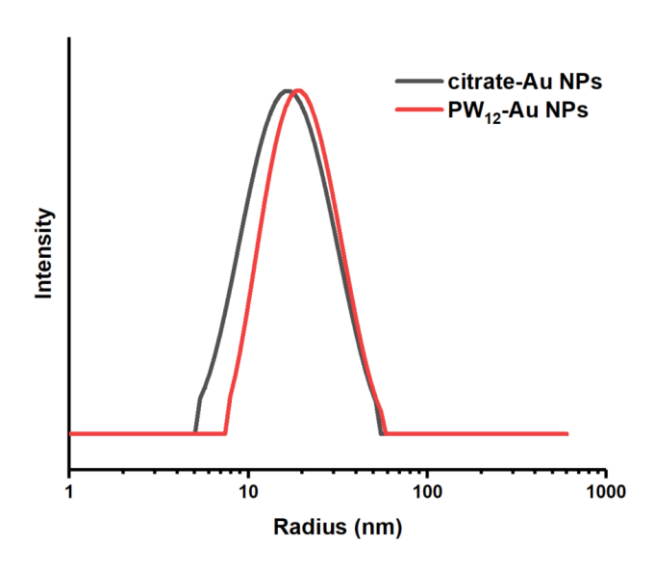


Figure 3.3. Dynamic light scattering (DLS) data of citrate-AuNPs and PW₁₂-AuNPs.

The synthesis of Citrate-AuNPs is based on the Turkevich method⁵⁰ after minor modification. After heating 100 mL of 0.50 mM AuCl₃ to boiling on a hotplate, 0.20 mL of 1.0 M trisodium citrate is added quickly with vigorous stirring. The faint yellowish color of AuCl₃ disappears immediately because of the citrate reduction reaction. After about 5 min, the color of the solution changes to wine-red indicating the formation of Au nanoparticles. The solution is heated with stirring for another 25 min to ensure complete conversion of AuCl₃ to Au (0), removed from the hot plate, and allowed to cool to room temperature. After the addition of

water to restore the volume to 100 mL, the solution is stored in the dark at room temperature. Figure 3.4 shows the UV-Vis spectra of citrate-stabilized Au nanoparticles (citrate-AuNPs), which have a surface plasmon resonance (SPR) with the absorption maximum shifted to 520 nm compared with the PW₁₂-AuNPs. This difference is detectable by human eyes as demonstrated by the inset photographs of citrate-AuNP and PW₁₂-AuNP aqueous solution in Figure 3.4. According to the transmission electron microscopy (TEM) image (Figure 3.5) and the dynamic light scattering data (Figure 3.3), the average size of citrate -AuNPs is around 16 nm, which is very similar to that of the PW₁₂-AuNPs. Therefore, the absorption maximum difference of the surface plasmon resonance (SPR) between the citrate-AuNPs and the PW₁₂-AuNPs is not the result of different particle size but different ligand (citrate vs. H₃PW₁₂O₄₀), which is consistent with previous reports.⁵¹

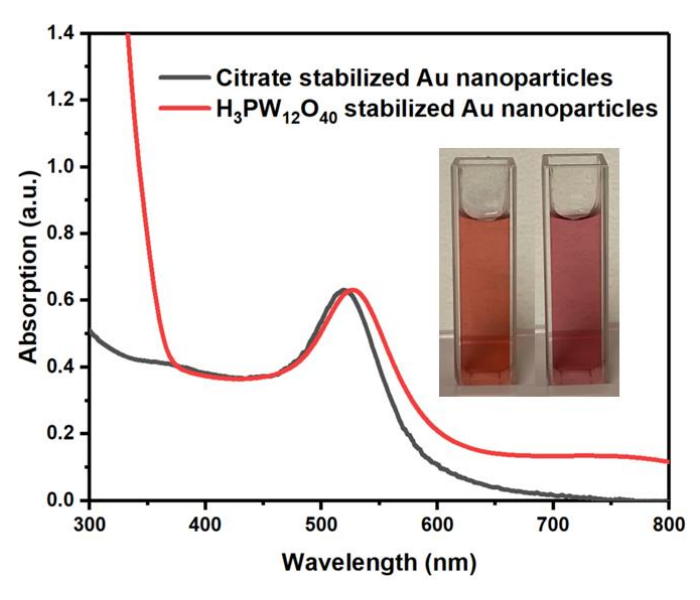


Figure 3.4. UV-Vis spectra of 0.70 mM aqueous solutions of citrate-AuNPs (black) and the PW₁₂-AuNPs (red). Inset: Photograph of 0.70 mM aqueous solution of citrate-AuNPs (left) and the PW₁₂-AuNPs (right) in a 1 cm quartz cuvette.

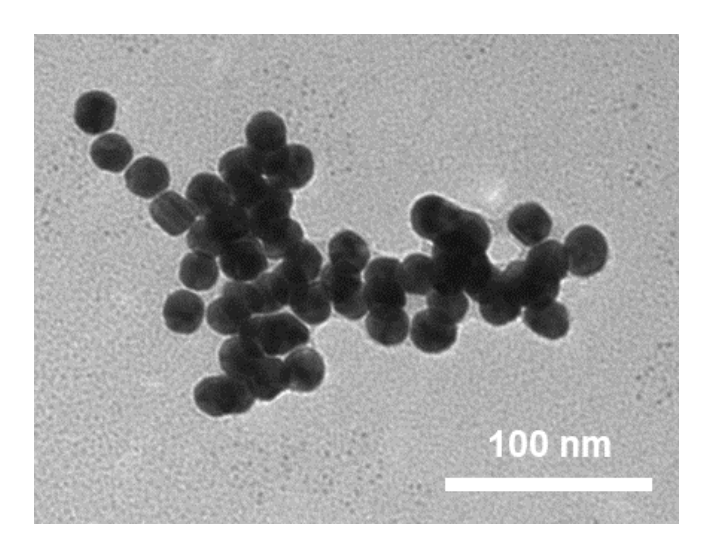


Figure 3.5. Transmission electron microscopy (TEM) image of citrate-AuNPs.

The X-ray photoelectron spectroscopy (XPS) (Figure 3.6) of the PW₁₂-AuNPs powder is then performed to analyze the ratio of POM to Au. The asymmetric XPS spectrum of Au 4f (Figure 3.7a) has well separated spin-orbit components ($\Delta_{metal} = 3.70 \text{ eV}$) with the Au 4f_{7/2} peak and the Au 4f_{5/2} peak are located at 84.18 eV and 87.88 eV, respectively. The XPS spectrum of W 4f (Figure 3.7b) shows that the binding energies are 36.08 eV (4f_{7/2}) and 38.28 eV (4f_{5/2}), which corresponds to the W (VI) chemical state. The loss feature for W(VI) at 42 eV is also observed. The POM: Au ratio in PW₁₂-AuNPs, based on the atomic ratio of W to Au in the XPS spectra and the number of the tungsten atoms in phosphotungstic acid is calculated to be 0.08. The POM: Au ratio is also quantified by adding 1.0 g of solid KCl to 3.0 mL of PW₁₂-AuNP solution. The addition of KCl salt precipitates the Au(0) nanoparticles and frees the Au-surface-bound phosphotungstate anions, resulting in a colorless solution with brown Au solids in the bottom. Understandably, these Au solids could not be redissolved in fresh water because phosphotungstates are no longer present on their surfaces. The weight of the precipitated brown Au solids after vacuum drying is 0.014 g. The concentration of phosphotungstate in the colorless solution is then determined to be 1.2 mM based on its

UV-Vis spectrum and the phosphotungstate UV-Vis standardization curves (Figure 3.11). The POM: Au ratio for PW₁₂-AuNPs is then calculated to be 0.05, which is in good agreement with the XPS-determined POM: Au ratio (0.03) considering the potential uncertainties related to such small amounts of precipitated Au solids. This POM: Au ratio for PW₁₂-AuNPs (0.05/0.03) is smaller than that of PW₁₁-AuNPs, SiW₁₁-AuNPs, and AlW₁₁-AuNPs reported in the literature because the binding affinities between POMs and Au nanoparticles increase with the POM-anion charge.⁵¹ It is important to point out here that the synthesis method (ligand exchange method) applied for PW₁₁-AuNPs, SiW₁₁-AuNPs, and AlW₁₁-AuNPs is different than our method (photochemical method) despite similar nanoparticle sizes. Moreover, PW₁₂-AuNPs couldn't be synthesized by the ligand exchange method possibly due to the lower binding strength of PW₁₂ with Au NPs than that of citrate. On the other hand, PW₁₁-AuNPs, SiW₁₁-AuNPs, and AlW₁₁-AuNPs couldn't be synthesized by the photochemical method because it is increasingly difficult to chemically reduce POMs as their negative charges increase.

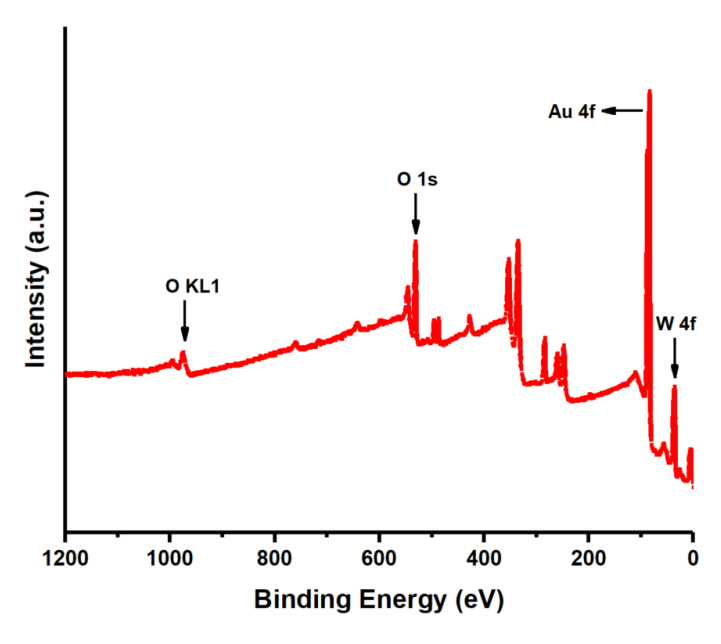


Figure 3.6. X-ray Photoelectron spectroscopy (XPS) of PW₁₂-AuNPs.

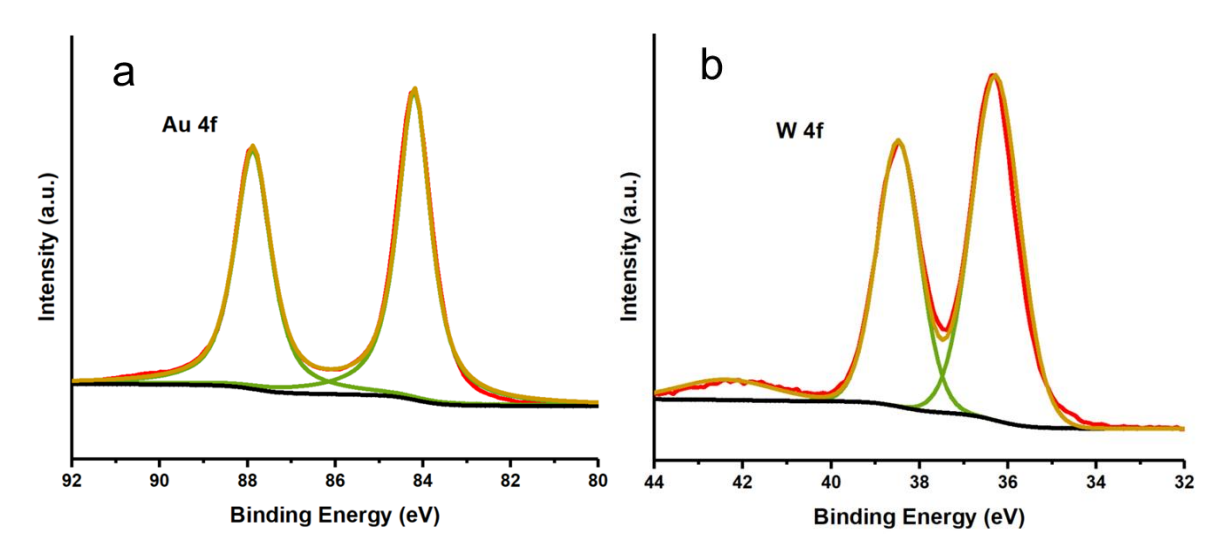


Figure 3.7. X-ray Photoelectron spectroscopy (XPS) of (a) Au 4f and (b) W 4f in PW₁₂-AuNPs.

The X-ray photoelectron spectroscopy (XPS) (Figure 3.8) of citrate-AuNPs powder was also performed. The asymmetric XPS spectrum of Au 4f (Figure 3.9a) has well-separated spin-orbit components (Δ_{metal} =3.70 eV) with the Au 4f_{7/2} peak and the Au 4f_{5/2} peaks located at 84.18 eV and 87.88 eV, respectively. The XPS spectrum of Na 1s (Figure 3.9b) shows a binding energy of 1071.68 eV. The XPS spectrum of C 1s (Figure 3.10) is fitted by three peaks at 284.8 eV, 286.5 eV, and 288.5 eV, which correspond to carbon atoms in the C-C, C-O, and C=O chemical environments, respectively.

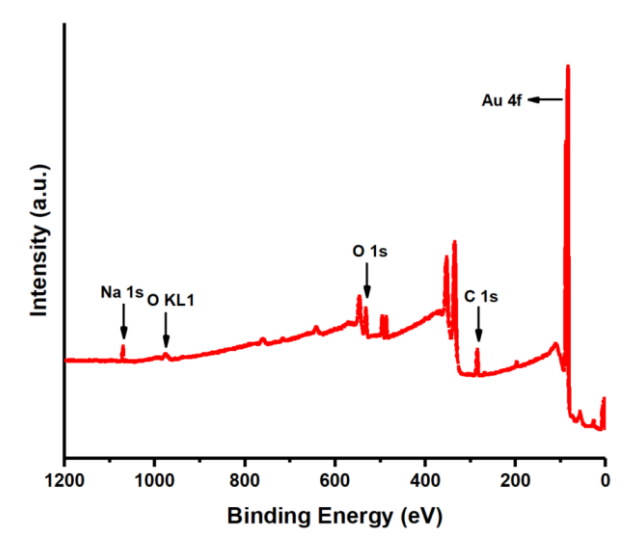


Figure 3.8. X-ray Photoelectron spectroscopy (XPS) of citrate-AuNPs.

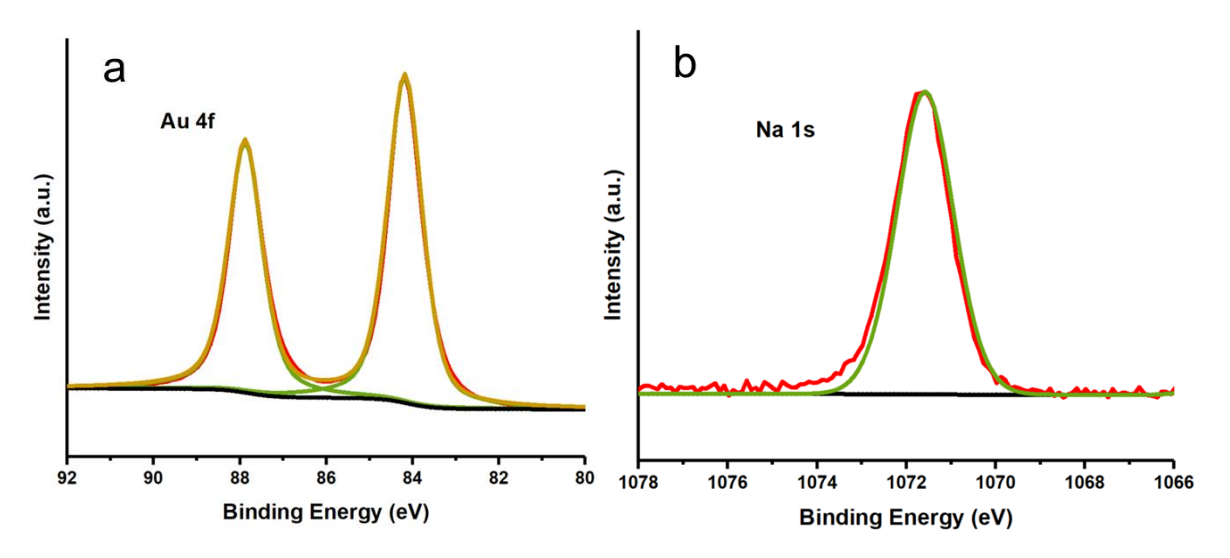


Figure 3.9. X-ray Photoelectron spectroscopy (XPS) of (a) Au 4f and (b) Na 1s in citrate-AuNPs.

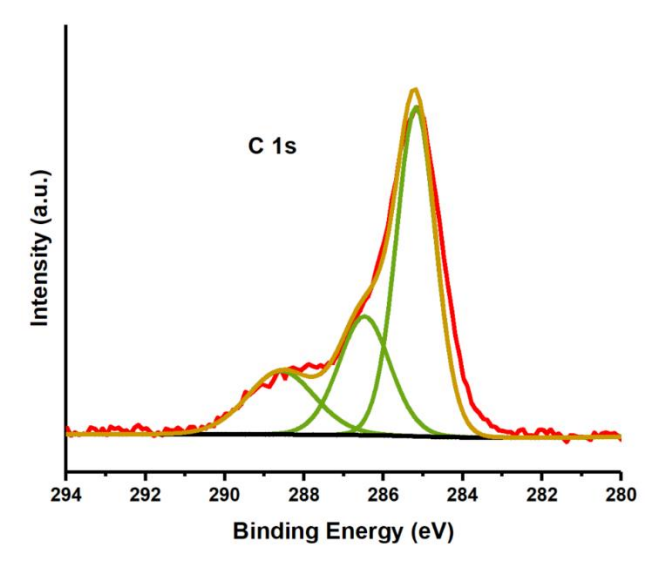


Figure 3.10. X-ray Photoelectron spectroscopy (XPS) of C 1s in citrate-AuNPs.

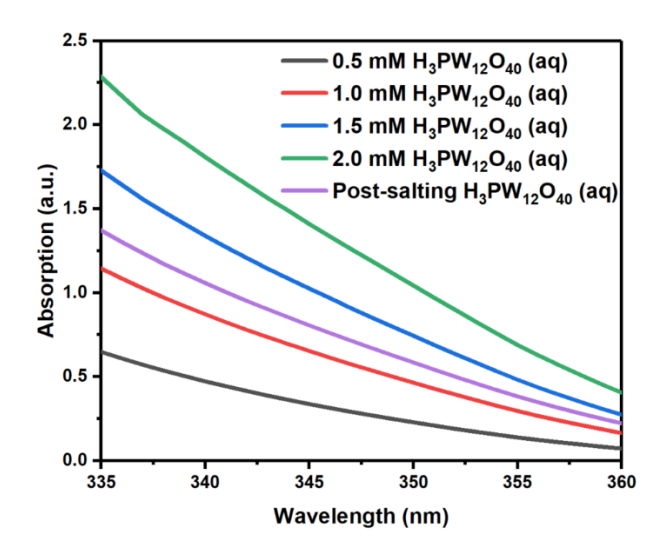


Figure 3.11. UV-Vis spectra of standard and post-salting H₃PW₁₂O₄₀ aqueous solution.

The FT-IR spectrum of PW₁₂-AuNPs is shown as the black curve in Figure 3.12. The peaks at 770 cm⁻¹ v(W-O_c-W, c = octahedral edge-sharing), 890 cm⁻¹ v(W-O_b-W, b = octahedral corner-sharing), 972 cm⁻¹ v(W-O_d, d = terminal), and 1071 cm⁻¹ v(P-O_a, a = tetrahedral) are consistent with the Keggin structure of [PW₁₂O₄₀]^{3-,52} which confirms the existence of [PW₁₂O₄₀]³⁻ in the nanoparticles. These peaks in the FT-IR spectrum remain the same (red curve) after 3 hours of continuous electrochemical CO₂ reduction in acetonitrile (the experimental detail will be discussed in the next section), which indicates the stability of [PW₁₂O₄₀]³⁻ during the catalysis. The formula of commercial phosphotungstic acid hydrate (H₃PW₁₂O₄₀·12H₂O) is determined by TGA as shown in Figure 3.13. The weight loss before 400 °C is 7.2%, which corresponds to 12 hydrated water molecules, and the weight loss after 400 °C is 0.9%, which results from the following decomposition reaction: $2H_3PW_{12}O_{40} \rightarrow P_2O_5 + 24WO_3 + 3H_2O$. This decomposition reaction is also verified by the color change of $H_3PW_{12}O_{40}$ ·12H₂O before heating (white) and after heating (yellow).

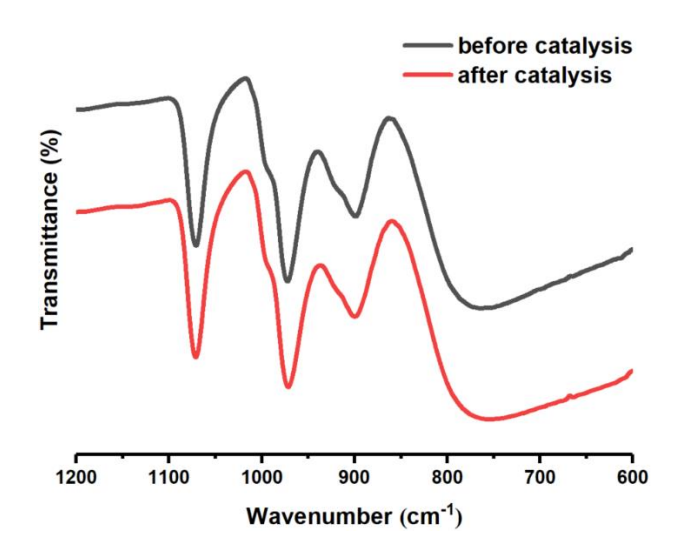


Figure 3.12. FT-IR spectra of PW₁₂-AuNPs before (black) and after (red) 3 hours of continuous electrochemical CO₂ reduction in acetonitrile.

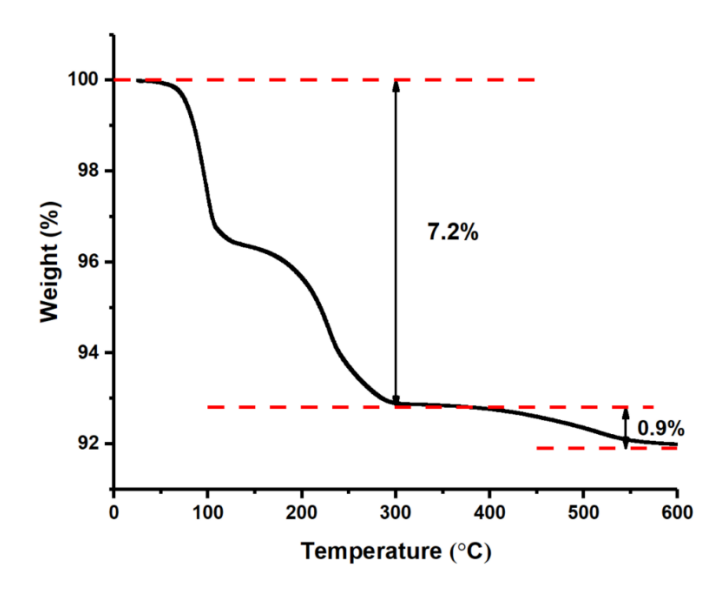


Figure 3.13. Thermogravimetric analysis (TGA) of H₃PW₁₂O₄₀·12H₂O (PW₁₂).

3.3.2 Reactivity of PW₁₂-AuNPs/Citrate-AuNPs.

The electrocatalytic activity of PW₁₂-AuNPs for CO₂ reduction was investigated in CH₃CN in the presence of 0.5% (v/v) H₂O. CH₃CN was chosen as the solvent medium for CO₂ reduction in our study, because (1) the solubility of CO₂ in CH₃CN is high (~ 0.28 M at 1 atm), ⁵³ (2) the proton source can be readily controlled in CH₃CN, so that the competing HER can be minimized, and (3) PW₁₂ is not stable in aqueous solutions at neutral pH where most of the aqueous CO₂ reduction reactions are conducted.⁷ The amount of added H₂O of 0.5% (v/v) was chosen to provide adequate proton source because its molar concentration is 0.275 M, which is comparable to that of CO₂ concentration (~ 0.28 M) in CO₂ saturated CH₃CN⁵³ and is generally the optimal amount for the CO₂ reduction reaction.³³ The measured potential was converted to the Fc⁺/Fc⁰ scale using data measured from CV for 1.0 mM ferrocene (Fc) (Figure 3.14). Under an argon atmosphere, three surface-confined redox processes are observed at potentials of about -0.75 V, -1.15 V, and -1.8 V versus Fc⁺/Fc⁰ (Figure 3.15 inset black curve). These are the characteristic redox processes of PW₁₂, which again confirm the

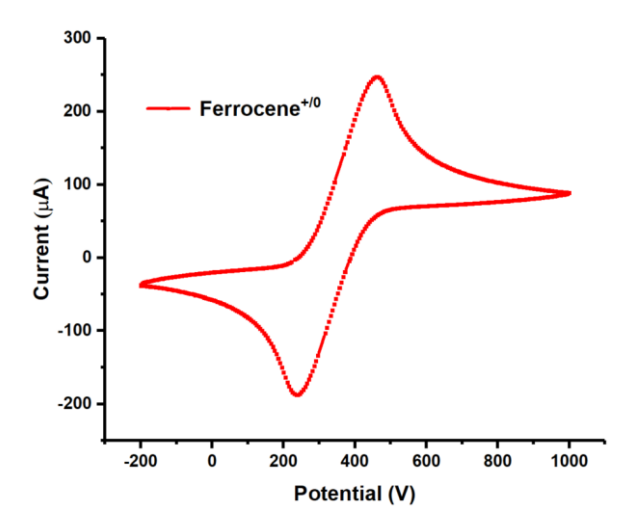


Figure 3.14. CV of 1.0 mM ferrocene (Fc) in CH₃CN with 0.5% (v/v) added H₂O.

presence of PW₁₂ in the deposited film on the glassy carbon electrode and its stability in organic solvent-water mixtures. Under a CO₂ atmosphere, a larger current is observed when the potential is scanned to more negative than the onset potential of about -1.7 V versus Fc⁺/Fc⁰ (Figure 3.15 inset red curve). This enhanced current is even more pronounced when the potential reaches -2.3 V versus Fc⁺/Fc⁰ (Figure 3.15 red curve), which is assigned to the reduction of CO₂ catalyzed by PW₁₂-AuNPs. To explore the potential role of PW₁₂ in the electrocatalytic reduction of CO₂, cyclic voltammograms of TBA₃PW₁₂O₄₀ in acetonitrile under

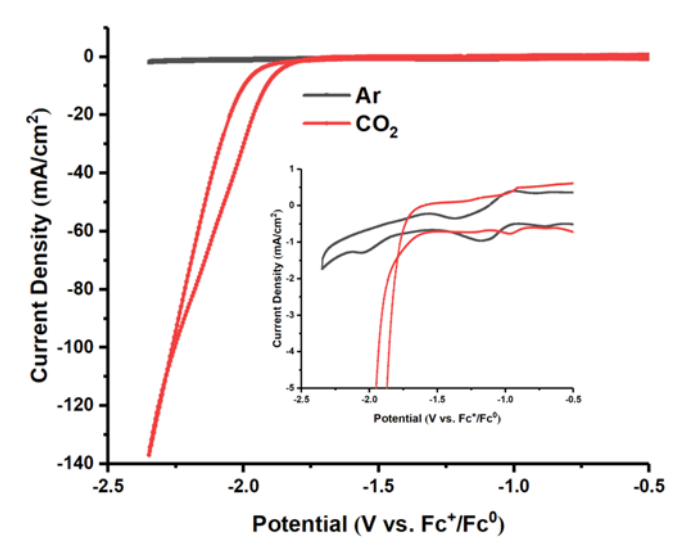


Figure 3.15. CVs of PW₁₂-AuNPs deposited on glassy carbon electrode in CH₃CN with 0.5% (v/v) added H₂O under an argon atmosphere (black) and a CO₂ atmosphere (red).

argon and CO₂ atmosphere are conducted for comparison. Cyclic voltammograms obtained under a N₂ atmosphere (Figure 3.16 black curves) show three well-defined chemically reversible redox processes in the potential range of 0 to -2.0 V, with the reversible potentials of -0.60 V (one electron), -1.20 V (one electron), and -1.80 V (two electron), respectively.⁵⁴ Some small peaks observed may be attributed to the acid-base chemistry of PW₁₂ in the presence of 0.5% added water. However, these peaks remain largely unchanged and no catalytic current is obtained under the CO₂ atmosphere, suggesting that PW₁₂ itself does not catalyze CO₂ reduction. Therefore, I tested the CO₂ reduction activity of citrate-AuNPs and found that it was almost the same as that of PW₁₂-AuNPs (Figure 3.17). I also checked other POM-stabilized gold nanoparticles that unfortunately all displayed comparable activities. The CO₂ reduction product with PW₁₂-AuNPs/citrate-AuNPs as the catalyst was measured by bulk electrolysis and determined to be only CO, which is not highly interesting. These findings indicate that POMs may not be able to assist metal electrocatalysts with CO₂ reduction, thus I stopped further study on PW₁₂-AuNPs.

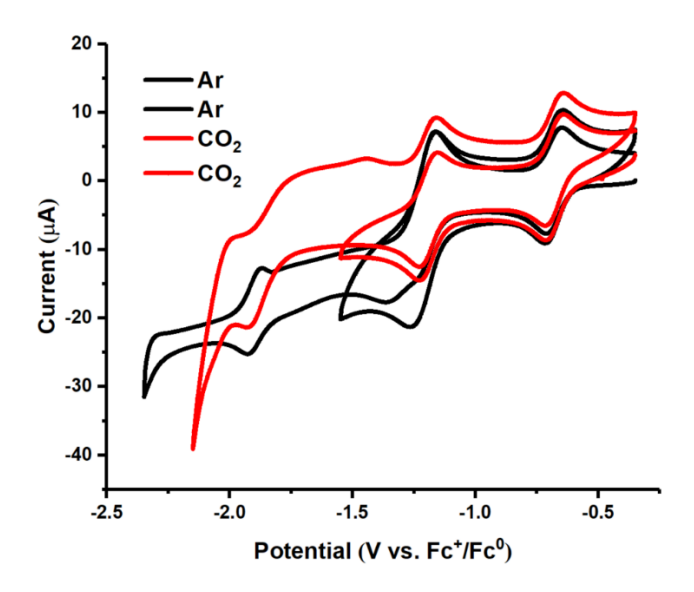


Figure 3.16. CVs of TBA₃PW₁₂ in CH₃CN with 0.5% (v/v) added H₂O under an argon atmosphere (black) and a CO₂ atmosphere (red).

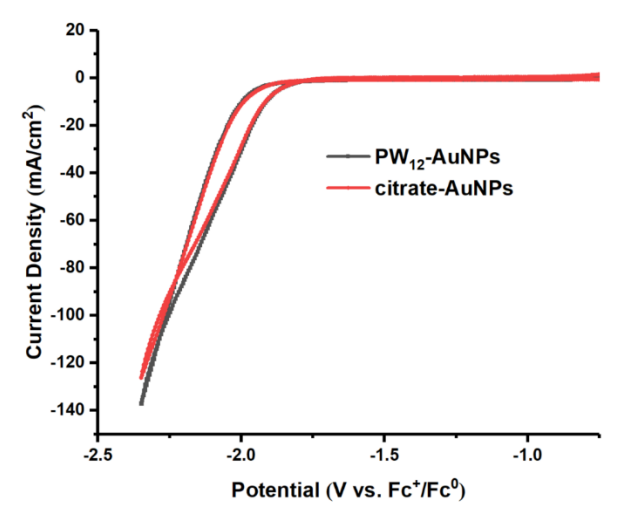


Figure 3.17. CVs of PW₁₂-AuNPs (black) and citrate-AuNPs (red) in CH₃CN with 0.5% (v/v) added H_2O under a CO_2 atmosphere.

3.4 Conclusions

- 1. Phosphotungstate (PW₁₂O₄₀³⁻) stabilized gold nanoparticles (PW₁₂-AuNPs) and citrate stabilized gold nanoparticles (citrate-AuNPs) were synthesized by the photochemical and thermochemical methods, respectively. They have similar particle sizes according to transmission electron microscopy (TEM) and dynamic light scattering (DLS) but have different absorption maxima of the surface plasmon resonance (SPR) and thus different colors. The composition of PW₁₂-AuNPs was determined by the X-ray photoelectron spectroscopy (XPS) and precipitation method.
- 2. PW₁₂-AuNPs and citrate-AuNPs are both tested for electrochemical CO₂ reduction reaction (CO₂RR) and exhibit almost the same activity. Cyclic voltammograms reveal that PW₁₂ does not catalyze CO₂RR and other POMs such as SiW₁₂, PW₁₁, and PW₉ couldn't promote CO₂RR when combined with Au nanoparticles as well. Besides, some copper and niobium containing POMs are also inactive for CO₂RR.

3.5 References

- 1. Ma, Y.; Wang, X.; Jia, Y.; Chen, X.; Han, H.; Li, C., Titanium dioxide-based nanomaterials for photocatalytic fuel generations. *Chem. Rev.* **2014**, *114* (19), 9987-10043.
- 2. Pearson, P. N.; Palmer, M. R., Atmospheric carbon dioxide concentrations over the past 60 million years. *Nature* **2000**, *406*, 695-699.
- 3. Seh, Z. W.; Kibsgaard, J.; Dickens, C. F.; Chorkendorff, I.; Norskov, J. K.; Jaramillo, T. F., Combining theory and experiment in electrocatalysis: Insights into materials design. *Science* **2017**, *355*, eaad4998.
- 4. Handoko, A. D.; Wei, F.; Jenndy; Yeo, B. S.; Seh, Z. W., Understanding heterogeneous electrocatalytic carbon dioxide reduction through operando techniques. *Nat. Catal.* **2018**, *1* (12), 922-934.
- 5. Birdja, Y. Y.; Pérez-Gallent, E.; Figueiredo, M. C.; Göttle, A. J.; Calle-Vallejo, F.; Koper, M. T. M., Advances and challenges in understanding the electrocatalytic conversion of carbon dioxide to fuels. *Nat. Energy* **2019**, *4* (9), 732-745.
- 6. Gao, D.; Arán-Ais, R. M.; Jeon, H. S.; Roldan Cuenya, B., Rational catalyst and electrolyte design for CO₂ electroreduction towards multicarbon products. *Nat. Catal.* **2019**, 2 (3), 198-210.
- 7. Ross, M. B.; De Luna, P.; Li, Y.; Dinh, C.-T.; Kim, D.; Yang, P.; Sargent, E. H., Designing materials for electrochemical carbon dioxide recycling. *Nat. Catal.* **2019**, *2* (8), 648-658.
- 8. Franco, F.; Rettenmaier, C.; Jeon, H. S.; Roldan Cuenya, B., Transition metal-based catalysts for the electrochemical CO₂ reduction: from atoms and molecules to nanostructured materials. *Chem. Soc. Rev.* **2020**, *49* (19), 6884-6946.

- 9. Nam, D. H.; De Luna, P.; Rosas-Hernandez, A.; Thevenon, A.; Li, F.; Agapie, T.; Peters, J. C.; Shekhah, O.; Eddaoudi, M.; Sargent, E. H., Molecular enhancement of heterogeneous CO₂ reduction. *Nat. Mater.* **2020**, *19* (3), 266-276.
- 10. Li, L.; Li, X.; Sun, Y.; Xie, Y., Rational design of electrocatalytic carbon dioxide reduction for a zero-carbon network. *Chem. Soc. Rev.* **2022**, *51* (4), 1234-1252.
- 11. Zhang, S.; Fan, Q.; Xia, R.; Meyer, T. J., CO₂ Reduction: From Homogeneous to Heterogeneous Electrocatalysis. *Acc. Chem. Res.* **2020**, *53* (1), 255-264.
- 12. Szczepankiewicz, S. H.; Ippolito, C. M.; Santora, B. P.; Van de Ven, T. J.; Ippolito, G. A.; Fronckowiak, L.; Wiatrowski, F.; Power, T.; Kozik, M., Interaction of Carbon Dioxide with Transition-Metal-Substituted Heteropolyanions in Nonpolar Solvents. Spectroscopic Evidence for Complex Formation. *Inorg. Chem.* **1998**, *37*, 4344-4352.
- 13. Girardi, M.; Blanchard, S.; Griveau, S.; Simon, P.; Fontecave, M.; Bedioui, F.; Proust, A., Electro Assisted Reduction of CO₂ to CO and Formaldehyde by (TOA)₆[α SiW₁₁O₃₉Co()] Polyoxometalate. *Eur. J. Inorg. Chem.* **2015**, *2015* (22), 3642-3648.
- 14. Girardi, M.; Platzer, D.; Griveau, S.; Bedioui, F.; Alves, S.; Proust, A.; Blanchard, S., Assessing the Electrocatalytic Properties of the {Cp*Rh^{|||}}²⁺ Polyoxometalate Derivative [H₂PW₁₁O₃₉{Rh^{|||}Cp*(OH₂)}]³⁻towards CO₂ Reduction. *Eur. J. Inorg. Chem.* **2018**, *2019* (3-4), 387-393.
- 15. Azaiza-Dabbah, D.; Vogt, C.; Wang, F.; Masip-Sanchez, A.; de Graaf, C.; Poblet, J. M.; Haviv, E.; Neumann, R., Molecular Transition Metal Oxide Electrocatalysts for the Reversible Carbon Dioxide-Carbon Monoxide Transformation. *Angew. Chem., Int. Ed.* **2022**, *61* (5), e202112915.

- 16. Du, D. Y.; Qin, J. S.; Li, S. L.; Su, Z. M.; Lan, Y. Q., Recent advances in porous polyoxometalate-based metal-organic framework materials. *Chem. Soc. Rev.* **2014**, *43* (13), 4615-4632.
- 17. Wang, Y. R.; Huang, Q.; He, C. T.; Chen, Y.; Liu, J.; Shen, F. C.; Lan, Y. Q., Oriented electron transmission in polyoxometalate-metalloporphyrin organic framework for highly selective electroreduction of CO₂. *Nat. Commun.* **2018**, 9 (1), 4466.
- 18. White, J. L.; Baruch, M. F.; Pander Iii, J. E.; Hu, Y.; Fortmeyer, I. C.; Park, J. E.; Zhang, T.; Liao, K.; Gu, J.; Yan, Y.; Shaw, T. W.; Abelev, E.; Bocarsly, A. B., Light-Driven Heterogeneous Reduction of Carbon Dioxide: Photocatalysts and Photoelectrodes. *Chem. Rev.* **2015**, *115* (23), 12888-12935.
- 19. Li, K.; Peng, B.; Peng, T., Recent Advances in Heterogeneous Photocatalytic CO₂ Conversion to Solar Fuels. *ACS Catal.* **2016**, *6* (11), 7485-7527.
- 20. Li, X.; Yu, J.; Jaroniec, M.; Chen, X., Cocatalysts for Selective Photoreduction of CO₂ into Solar Fuels. *Chem. Rev.* **2019**, *119* (6), 3962-4179.
- 21. Jiao, X.; Zheng, K.; Liang, L.; Li, X.; Sun, Y.; Xie, Y., Fundamentals and challenges of ultrathin 2D photocatalysts in boosting CO₂ photoreduction. *Chem. Soc. Rev.* **2020**, *49* (18), 6592-6604.
- 22. Wagner, A.; Sahm, C. D.; Reisner, E., Towards molecular understanding of local chemical environment effects in electro- and photocatalytic CO₂ reduction. *Nat. Catal.* **2020**, 3 (10), 775-786.
- 23. Khenkin, A. M.; Efremenko, I.; Weiner, L.; Martin, J. M.; Neumann, R., Photochemical reduction of carbon dioxide catalyzed by a ruthenium-substituted

- polyoxometalate. Chem. -Eur. J. 2010, 16 (4), 1356-1364.
- 24. Poblet, J. M., Photoreduction Mechanism of CO₂ to CO Catalyzed by a Rhenium(I)-Polyoxometalate Hybrid Compound. *ACS Catal.* **2016**, *6*, 6422-6428.
- 25. Li, N.; Liu, J.; Liu, J. J.; Dong, L. Z.; Li, S. L.; Dong, B. X.; Kan, Y. H.; Lan, Y. Q., Self-Assembly of a Phosphate-Centered Polyoxo-Titanium Cluster: Discovery of the Heteroatom Keggin Family. *Angew. Chem., Int. Ed.* **2019**, *58* (48), 17260-17264.
- 26. Zhou, J.; Chen, W.; Sun, C.; Han, L.; Qin, C.; Chen, M.; Wang, X.; Wang, E.; Su, Z., Oxidative Polyoxometalates Modified Graphitic Carbon Nitride for Visible-Light CO₂ Reduction. *ACS Appl. Mater. Interfaces* **2017**, *9* (13), 11689-11695.
- 27. Yu, H.; Haviv, E.; Neumann, R., Visible-Light Photochemical Reduction of CO₂ to CO Coupled to Hydrocarbon Dehydrogenation. *Angew. Chem., Int. Ed.* **2020,** *59* (15), 6219-6223.
- 28. Li, X. X.; Liu, J.; Zhang, L.; Dong, L. Z.; Xin, Z. F.; Li, S. L.; Huang-Fu, X. Q.; Huang, K.; Lan, Y. Q., Hydrophobic Polyoxometalate-Based Metal-Organic Framework for Efficient CO₂ Photoconversion. *ACS Appl. Mater. Interfaces* **2019**, *11* (29), 25790-25795.
- 29. Lu, M.; Zhang, M.; Liu, J.; Yu, T. Y.; Chang, J. N.; Shang, L. J.; Li, S. L.; Lan, Y. Q., Confining and Highly Dispersing Single Polyoxometalate Clusters in Covalent Organic Frameworks by Covalent Linkages for CO₂ Photoreduction. *J. Am. Chem. Soc.* **2022**, *144* (4), 1861-1871.
- 30. Angamuthu, R.; Byers, P.; Lutz, M.; Spek, A. L.; Bouwman, E., Electrocatalytic CO₂ Conversion to Oxalate by a Copper Complex. *Science* **2010**, *327*, 313-315.
- 31. Pokharel, U. R.; Fronczek, F. R.; Maverick, A. W., Reduction of carbon dioxide to oxalate by a binuclear copper complex. *Nat. Commun.* **2014,** *5*, 5883.

- 32. Takeda, H.; Cometto, C.; Ishitani, O.; Robert, M., Electrons, Photons, Protons and Earth-Abundant Metal Complexes for Molecular Catalysis of CO₂ Reduction. *ACS Catal.* **2016,** *7* (1), 70-88.
- 33. Francke, R.; Schille, B.; Roemelt, M., Homogeneously Catalyzed Electroreduction of Carbon Dioxide-Methods, Mechanisms, and Catalysts. *Chem. Rev.* **2018**, *118* (9), 4631-4701.

 34. Kamata, K.; Nakagawa, Y.; Yamaguchi, K.; Mizuno, N., 1,3-Dipolar Cycloaddition of Organic Azides to Alkynes by a Dicopper-Substituted Silicotungstate. *J. Am. Chem. Soc.* **2008**, *130*, 15304-15310.
- 35. Kamata, K.; Yamaguchi, S.; Kotani, M.; Yamaguchi, K.; Mizuno, N., Efficient oxidative alkyne homocoupling catalyzed by a monomeric dicopper-substituted silicotungstate. *Angew. Chem., Int. Ed.* **2008,** *47* (13), 2407-2410.
- 36. Asadi, M.; Kumar, B.; Behranginia, A.; Rosen, B. A.; Baskin, A.; Repnin, N.; Pisasale, D.; Phillips, P.; Zhu, W.; Haasch, R.; Klie, R. F.; Kral, P.; Abiade, J.; Salehi-Khojin, A., Robust carbon dioxide reduction on molybdenum disulphide edges. *Nat. Commun.* **2014**, *5*, 4470.
- 37. Hong, X.; Chan, K.; Tsai, C.; Nørskov, J. K., How Doped MoS₂ Breaks Transition-Metal Scaling Relations for CO₂ Electrochemical Reduction. *ACS Catal.* **2016**, *6* (7), 4428-4437.
- 38. Francis, S. A.; Velazquez, J. M.; Ferrer, I. M.; Torelli, D. A.; Guevarra, D.; McDowell, M. T.; Sun, K.; Zhou, X.; Saadi, F. H.; John, J.; Richter, M. H.; Hyler, F. P.; Papadantonakis, K. M.; Brunschwig, B. S.; Lewis, N. S., Reduction of Aqueous CO₂ to 1-Propanol at MoS₂ Electrodes. *Chem. Mater.* **2018**, *30* (15), 4902-4908.

- 39. Kibsgaard, J.; Jaramillo, T. F.; Besenbacher, F., Building an appropriate active-site motif into a hydrogen-evolution catalyst with thiomolybdate [Mo₃S₁₃]²⁻ clusters. *Nat. Chem.* **2014**, 6 (3), 248-253.
- 40. Lei, Y.; Yang, M.; Hou, J.; Wang, F.; Cui, E.; Kong, C.; Min, S., Thiomolybdate [Mo₃S₁₃]²⁻ nanocluster: a molecular mimic of MoS₂ active sites for highly efficient photocatalytic hydrogen evolution. *Chem. Commun.* **2018**, *54* (6), 603-606.
- 41. Mal, S. S.; Kortz, U., The wheel-shaped Cu₂₀ tungstophosphate [Cu₂₀Cl(OH)₂₄(H₂O)₁₂(P₈W₄₈O₁₈₄)]²⁵⁻ ion. *Angew. Chem., Int. Ed.* **2005,** 44 (24), 3777-3780.
- 42. Sasaki, S.; Yonesato, K.; Mizuno, N.; Yamaguchi, K.; Suzuki, K., Ring-Shaped Polyoxometalates Possessing Multiple 3d Metal Cation Sites: $[\{M_2(OH_2)_2\}_2\{M(OH_2)_2\}_4P_8W_{48}O_{176}(OCH_3)_8]^{16-} (M = Mn, Co, Ni, Cu, Zn). \textit{ Inorg Chem 2019, 58} (12), 7722-7729.$
- 43. Rosen, B. A.; Salehi-Khojin, A.; Thorson, M. R.; Zhu, W.; Whipple, D. T.; Kenis, P. J. A.; Masel, R. I., Ionic Liquid–Mediated Selective Conversion of CO₂ to CO at Low Overpotentials. *Science* **2011**, (334), 643-644.
- 44. Liu, M.; Pang, Y.; Zhang, B.; De Luna, P.; Voznyy, O.; Xu, J.; Zheng, X.; Dinh, C. T.; Fan, F.; Cao, C.; de Arquer, F. P.; Safaei, T. S.; Mepham, A.; Klinkova, A.; Kumacheva, E.; Filleter, T.; Sinton, D.; Kelley, S. O.; Sargent, E. H., Enhanced electrocatalytic CO₂ reduction via field-induced reagent concentration. *Nature* **2016**, *537* (7620), 382-386.
- 45. Mariano, R. G.; McKelvey, K.; White, H. S.; Kanan, M. W., Selective increase in CO₂ electroreduction activity at grain-boundary surface terminations. *Science* **2017**, *358*, 1187-

1192.

- 46. Dinh, C. T.; Burdyny, T.; Kibria, M. G.; Seifitokaldani, A.; Gabardo, C. M.; De Arquer, F. P.; Kiani, A.; Edwards, J. P.; Luna, P. D.; Bushuyev, O. S.; Zou, C.; Quintero-Bermudez, R.; Pang, Y.; Sinton, D.; Sargent, E. H., CO₂ electroreduction to ethylene via hydroxide-mediated copper catalysis at an abrupt interface. *Science* **2018**, *360*, 783-787.
- 47. Yang, Y.; Louisia, S.; Yu, S.; Jin, J.; Roh, I.; Chen, C.; Fonseca Guzman, M. V.; Feijoo, J.; Chen, P. C.; Wang, H.; Pollock, C. J.; Huang, X.; Shao, Y. T.; Wang, C.; Muller, D. A.; Abruna, H. D.; Yang, P., Operando studies reveal active Cu nanograins for CO₂ electroreduction. *Nature* **2023**, *614* (7947), 262-269.
- 48. Varga, G. M.; Pope, M. T., Heteropoly Blues. I. Reduction Stoichiometries and Reduction Potentials of Some 12-Tungstates. *Inorg. Chem.* **1966**, *5*, 1249-1254.
- 49. Varga, G. M.; Papaconstantinou, E.; Pope, M. T., Heteropoly Blues. IV. Spectroscopic and Magnetic Properties of Some Reduced Polytungstates. *Inorg. Chem.* **1970,** 9 (3), 662-667.
- 50. Kimling, J.; Maier, M.; Okenve, B.; Kotaidis, V.; Ballot, H.; Plech, A., Turkevich Method for Gold Nanoparticle Synthesis Revisited. *J. Phys. Chem. B.* **2006**, *110*, 15700-15707.
- 51. Wang, Y.; Neyman, A.; Arkhangelsky, E.; Gitis, V.; Meshi, L.; Weinstock, I. A., Self-Assembly and Structure of Directly Imaged Inorganic-Anion Monolayers on a Gold Nanoparticle. *J. Am. Chem. Soc.* **2009**, *131*, 17412-17422.
- 52. Ishiba, K.; Noguchi, T.; Iguchi, H.; Morikawa, M. A.; Kaneko, K.; Kimizuka, N.,

Photoresponsive Nanosheets of Polyoxometalates Formed by Controlled Self-Assembly Pathways. *Angew. Chem., Int. Ed.* **2017,** *56* (11), 2974-2978.

53. Costentin, C.; Drouet, S.; Robert, M.; Saveant, J. M., A Local Proton Source Enhances CO₂ Electroreduction to CO by a Molecular Fe Catalyst. *Science* **2012**, *338*, 90-94.

54. Himeno, S.; Takamoto, M.; Ueda, T., Synthesis, characterisation and voltammetric study of a β-Keggin-type [PW₁₂O₄₀]³⁻ complex. *J. Electroanal. Chem.* **1999**, *465*, 129-135.

Chapter 4:

Cobalt-polyoxometalate-TiO₂ Photoelectrode for Efficient
Oxygen Evolution Reaction in Acidic Media

Abstract

Renewable fuel generation by solar power is crucial to a low-carbon economy and eliminates CO₂ production from burning of fossil fuels. The oxygen evolution reaction (OER), a critical process in solar fuel production, has drawn significant research attention, with numerous (photo)electro-catalysts being identified and examined. 1-11 However, achieving OER, especially under acidic conditions, poses a challenge for metal oxide photoanodes, due to the sluggish four-hole oxidization process and the corrosive nature of an acidic environment. Here we report fabrication of amorphous n-type TiO₂ photoelectrodes by treatment of cationic 3-aminopropyltrimethoxysilane (APS)functionalized TiO₂ with Na₈K₈[Co₉(H₂O)₆(OH)₃(HPO₄)₂(PW₉O₃₄)₃] (**Co₉POM**). Compared to the unmodified TiO₂, the functionalized TiO₂ photoanode, TiO₂-APS-Co₃POM, exhibits an approximately three-fold OER enhancement of photocurrent in a sulfate buffer solution (pH = 2). X-ray photoelectron spectroscopy shows that the surface-bound Co₉POM retains its structural integrity throughout bulk electrolysis. We studied the catalytic effect of Co₉POM using open circuit photovoltage measurements and transient absorption spectroscopy in both the visible and mid-IR ranges. Mechanistic investigations indicate that Co₉POM serves as an efficient water oxidation catalyst, extracting photogenerated holes from TiO₂ at picosecond timescale. Moreover, by shifting the TiO₂ band edge, the functionalized catalytic layer creates a favorable interfacial electric field, which efficiently separates the photogenerated carriers and mitigates surface recombination.

4.1 Introduction

Solar energy is the most attractive renewable replacement for fossil fuels because it is plentiful, inexhaustible, and widely distributed. However, due to the diffuse and intermittent nature of solar irradiation, energy harvested from the sun must be efficiently converted into chemical fuels that are storable, transportable, and usable upon demand. This requirement has motivated the development of sustainable artificial photosynthetic processes, with the aim of mimicking natural photosynthesis to generate fuels from water and carbon dioxide utilizing solar energy. Therefore, a significant effort has been dedicated towards increasing the performance of solar-fuel-generating devices over the last few decades. 12-16 The oxygen evolution reaction (OER) is thus of great importance because it is the critical (photo)anode reaction for (photo)electrochemical production of solar fuels including H₂ from water and hydrocarbons from CO₂. ¹⁷⁻¹⁹ The multielectron transfer OER process involves multiple reaction intermediates, and a high overpotential is needed to overcome the sluggish kinetics. Among the different water splitting devices, acidic proton-exchange-membrane (PEM) water electrolyzers offer greater advantages such as high current density and high-purity hydrogen output. However, current anode OER electrocatalysts in PEM electrolyzers are limited to precious iridium and ruthenium oxides because of their high stability.²⁰ Therefore, the major challenge facing PEM electrolysis is minimizing Ir or Ru utilization due to their scarcity and thus high and volatile price. For example, Yan and co-workers report a novel strategy to prepare iridium singleatoms (Ir-SAs) on ultrathin NiCo₂O₄ porous nanosheets (Ir-NiCo₂O₄ NSs) by the coelectrodeposition method.²¹ The surface-exposed Ir-SAs couplings with oxygen vacancies (V₀) result in boosted catalytic OER activity and stability in acid media. They display superior OER performance with an ultralow overpotential of 240 mV at j = 10

mA/cm² and long-term stability of 70 h in acid media. The TOFs of 1.13 and 6.70 s⁻¹ at an overpotential of 300 and 370 mV also confirm their remarkable performance. Density functional theory (DFT) calculations reveal that the prominent OER performance arises from the surface electronic exchange and transfer activities facilitated by atomic Ir incorporation on the intrinsic Vo existed NiCo₂O₄ surface. More recently, Wang and coworkers synthesized a nickel-stabilized, ruthenium dioxide (Ni-RuO₂) catalyst, a promising alternative to iridium, with high activity and durability for acidic OER in PEM water electrolysis. While pristine RuO₂ showed poor acidic OER stability and degraded within a short period of continuous operation, the incorporation of Ni greatly stabilized the RuO₂ lattice and extended its durability by more than one order of magnitude.²² The Ni-RuO₂ catalyst was stable for >1,000 h stability at a water-splitting current of 200 mA/cm² when functioning as the anode of a PEM water electrolyzer.

To further eliminate the use of Ir or Ru oxides, Nocera and co-workers synthesized an electrodeposited manganese oxide (MnO_x) that could be functionally stable for OER in pH 2-2.5.²³ The intersection of the kinetic profile of deposition and that of water oxidation as a function of pH is found to define the region of kinetic stability for MnO_x and the electrocatalyst film is considered to be in a dynamic but functionally stable state. Moreover, this work suggests that a nonnoble metal oxide OER catalyst can be operated in acid by exploiting a "self-healing" process. In detail, the intrinsically unstable MnO_x films dissolved in the electrolyte near the electrode can regrow MnO_x films through an anodic electrodeposition process during the catalytic cycle, as long as MnO_x deposition occurs at potentials below those required for OER. The activity of this MnO_x catalyst can be further improved after activation by potential cycling protocols, as measured by Tafel

analysis from \approx 650 to \approx 90 mV/dec in acidic solutions.²⁴ During the activation process, the original birnessite-like manganese oxide (δ -MnO₂) undergoes a phase change to a hausmannite-like intermediate (α -Mn₃O₄). Subsequent anodic conditioning from voltage cycling or water oxidation produces a disordered δ -MnO₂ phase, which is highly active for oxygen evolution. At pH = 2.5, the current density of activated MnO_x (at an overpotential of 600 mV) is two orders of magnitude higher than that of the original MnO_x and begins to approach that of Ru and Ir oxides in acid.

While progress has been made toward achieving greater acid stability under devicerelevant conditions for manganese oxide OER catalysis, cobalt-based OER catalysts are known to be more active than manganese systems over a range of pH values. Hence the exploration of efficient and acid-compatible cobalt oxide OER catalysts is all the more imperative. Schaak et al. prepared crystalline cobalt oxide film deposited on fluorinated tin oxide (FTO) via calcination at 400 °C.²⁵ The Co₃O₄/FTO electrode can evolve oxygen with near-quantitative Faradaic yield and maintain a current density of 10 mA/cm² for over 12 h at an overpotential of 570 mV in 0.5 M H₂SO₄. Nocera and co-workers designed mixed metal oxide films (CoFePbO_x) by decoupling catalytic sites (CoO_x) and structural sites (FePbO_x) as separate components. The mixed metal oxides exhibited much enhanced stability compared with bare cobalt oxide in acidic media.²⁶ The optimized CoFePbO_x can oxidize water at an overpotential of ≈ 720 mV to maintain 1 mA/cm² in pH 2.0 solution for 50 h. Another similar CoFePbO_x mixed metal oxide was formed in situ during electrooxidation of acidic water containing cobalt, lead and iron precursors. Utilizing a stable Pt/Ti electrode as the substrate, the electrode-electrolyte system allows for a continuous water oxidation at temperatures up to 80 °C and rates up to 500 mA/cm²

at overpotentials below 0.7 V in 1 M H₂SO₄ containing metal precursors.²⁷ The robust operation of this CoFePbO_x catalyst is provided by the thermodynamically stable lead oxide matrix that accommodates homogeneously distributed catalytic dopants via a similar self-healing mechanism mentioned above. Galan-Mascaros et al. synthesized carbon-coated cobalt oxide (Co₃O₄@C) nanoparticles, starting from the thermal treatment of Co(blm)₂ (blm= 2-benzimidazolate), a metal-organic framework (MOF) precursor (ZIF-9). Co₃O₄@C was then mixed with graphite (G) and paraffin oil (PO) in the desired ratio to prepare a homogeneous composite (Co₃O₄@C/GPO) anode, which catalyzed stable oxygen formation with a 10 mA/cm² current density at overpotentials around 400 mV for > 40 h in 1 M H₂SO₄ solution.²⁸ Very recently, Liu et al. reported a nanofibrous cobalt spinel catalyst co-doped with lanthanum (La) and manganese (Mn) prepared from a zeolitic imidazolate framework embedded in electrospun polymer fiber. The catalyst demonstrated a low overpotential of 353 mV at 10 mA/cm² and a low degradation for OER over 360 hours in acidic electrolyte. A PEM water electrolyzer containing this catalyst at the anode achieved a current density of 2000 mA /cm² at 2.47 V (Nafion 115 membrane) or 4000 mA/cm² at 3.00 V (Nafion 212 membrane) and low degradation in an accelerated stress test.²⁹ The design concept is that the lanthanum ion (La³⁺) has a much larger radius compared with that of Co²⁺ (1.06 Å versus 0.72 Å) so it could generate strain, oxygen vacancy (Vo), and acid tolerance while the manganese ion (Mn²⁺) has a similar radius to Co²⁺ (0.8 Å versus 0.72 Å), which would be oxidized to Mn³⁺ (0.72 Å) during the oxidative conversion and uniformly distributed inside the cobalt spinel lattice to promote conductivity (via bandgap) and OER activity (via affinity OH or H group). In situ x-ray absorption spectroscopy (XAS) and density functional theory (DFT) supported the above

analysis of the La and Mn doping effects. Other cobalt related materials including Co-doped MoS₂³⁰ and polymetallic MoS₂/Co₉S₈/Ni₃S₂/Ni-foam composite³¹ were also investigated for OER in acidic media. It was demonstrated that cobalt-doping could enhance the OER activity of MoS₂ in acid, but its performance was still much lower than that of RuO₂.³⁰ The optimized hierarchical nano assembly of MoS₂/Co₉S₈/Ni₃S₂/Ni only needed an overpotential of 228 mV to reach 10 mA/cm² in acid due to the 3D structure and possible synergistic effects, but the long-term stability was unknown.³¹

Cobalt polyoxometalates (Co-POMs) have emerged as promising water oxidation catalysts (WOCs), with the added advantage of their molecular nature despite being metal oxide fragments.³²⁻⁴³ In comparison with metal oxides that do not offer well-defined active surfaces, POMs have a controlled, discrete structure that allows for precise correlations between experiment and computational analyses. Thus, beyond highly active WOCs, POMs are also model systems to gain deeper mechanistic understanding on the oxygen evolution reaction (OER). For instance, Hill and co-workers reported [Co₄(H₂O)₂(PW₉O₃₄)₂]¹⁰⁻ (Co₄POM) as the first POM WOC constituted solely by earthabundant elements using Ru(bpy)₃³⁺ as the oxidant³² and later using Ru(bpy)₃²⁺ and $S_2O_8^{2-}$ as the photosensitizer and the sacrificial agent, respectively, in pH = 8 borate buffer solution.⁴² Co₄POM is composed of a tetra cobalt-oxo core stabilized by two tri-lacunary Keggin moieties (PW₉O₃₄⁹⁻) forming the well-known Weakley sandwich structure. The integrity of the molecular Co₄POM during water oxidation reaction was confirmed³³, which ruled out the possibility of CoO_x formation from Co₄POM decomposition and consequent contribution to the catalytic activity. The vanadium derivative of Co₄POM, i.e., [Co₄(H₂O)₂(VW₉O₃₄)₂]¹⁰⁻ was also identified as an efficient and stable WOC.^{34, 41} In

addition, Cronin et al. synthesized Mo-doped Co₄POM, i.e., $[Co_4(H_2O)_2(PW_xMo_yO_{34})_2]^{10}$ (x + y = 9), which displayed a lower onset potential for OER in a pH = 7 potassium phosphate buffer solution compared with the pure Co₄POM.⁴³ Furthermore, Co₄POM has also been incorporated into a light-absorbing metal organic framework (MOF-545) to perform photocatalytic water oxidation reaction with S₂O₈²⁻ as the sacrificial agent in a pH = 8 borate buffer solution.³⁹

In addition to Co₄POM, Galan-Mascaros et al. reported another Co-POM, $[Co_9(H_2O)_6(OH)_3(HPO_4)_2(PW_9O_{34})_3]^{16}$ (Co_9POM), catalyzed efficient water oxidation reaction. This Co₉POM contains three triads of edge-sharing Co^{II}O₆ octahedra supported by three tri-vacant Keggin-type [PW₉O₃₄] units. The triads are interconnected through three OH⁻ and two HPO₄²⁻ bridges. Six of the Co ions complete their coordination sphere with terminal water molecules. When coated on a FTO electrode then applied with an anodic overpotential of ≈ 600 mV in a pH = 7 sodium phosphate buffer solution, Co₉POM evolved O₂ for weeks without sign of fatigue or decomposition.³⁷ By substituting the counter cations of Co₉POM with Ba²⁺, a water-insoluble Ba²⁺ salt formed, which acted as a very efficient WOC whose activity outperformed the state-of-the-art IrO₂ catalyst even at pH < 1, with an overpotential of 189 mV at 1 mA/cm². Subsequently, Galan-Mascaros et al. tested different Cs⁺ and Ba²⁺ salts of Co-POMs for water oxidation reaction in acidic media and concluded that the Keggin-derivatives of Co-POMs containing PV as the heteroatom and higher nuclearity of the cobalt cluster exhibited better stability and catalytic activity with Co₉POM being the best WOC.³⁶ Based on all of these research, I decided to use Co₉POM as the catalyst and immobilize it on the TiO₂ photoelectrode for the photoelectrochemical oxygen evolution reaction in acidic media.

4.2 Experimental

4.2.1 General Materials and Methods

Materials and solvents were purchased as ACS analytical or reagent grade and used as received. Na₈K₈[Co₉(H₂O)₆(OH)₃(HPO₄)₂(PW₉O₃₄)₃]-49H₂O (Co₉POM) was obtained following a synthesis described in the literature.44 The purity of the Co₉POM was confirmed by the Fourier transform infrared (FT-IR) (Figure 4.1a) and the water content was determined by thermogravimetric analysis (TGA) (Figure 4.1b). Infrared spectra (2% sample in KBr pellet) were recorded on a Nicolet TM 6700 Fourier transform infrared (FT-IR) spectrometer. UV-vis spectra were collected with an Agilent 8453 spectrophotometer using a 1.0 cm optical path length quartz cuvette. The Inductively Coupled Plasma (ICP) data were collected on a Thermo iCAP ICP-MS instrument in the Institute of Electronics and Nanotechnology at Georgia Institute of Technology. X-ray photoelectron spectroscopy (XPS) was conducted on a thermos K-ALPHA XPS instrument. The TGA data were collected on a Mettler Toledo TGA instrument. Diffuse reflectance spectroscopy was measured on a Cary 5000 UV-Vis/NIR instrument. Gas chromatography (GC) analysis of the gas phase was analyzed using an Agilent 7890 gas chromatograph with a 5 Å molecular sieve column, a thermal conductivity detector, and argon carrier gas. The Raman spectroscopy is measured in a home-built Raman setup as described in previous literature.45

4.2.2 Preparation of POM/Co-Pi modified TiO₂ Photoelectrodes

The preparation of TiO_2 and TiO_2 coated with Co_9POM photoelectrodes is based on our previous report with modifications.⁴⁶ The fluorine-doped tin oxide substrates, FTO (Pilkington TEC15, ~ 15 Ω /sq resistance), were cleaned by sonicating sequentially in

deionized water, acetone, and ethanol for 20 min each time, followed by blowing dry with nitrogen gas. Before coating, the top area of substrate was covered by one layer of adhesive tape (40 µm thickness) to provide a noncoated area for electrical conductance for the final electrode. The bottom area (smaller than the top area) was also covered by one layer of adhesive tape for the following Doctor blade coating process. The 20 nmsized TiO₂ paste (Dyesol, 90-T) was then applied in the center of the substrate and distributed with a glass rod sliding over the tape-covered substrates on the side. The substrates were sintered at 500 °C for 1 hour, yielding a ~10-20 µm thick nanostructured TiO₂ film. The noncoated area of TiO₂ electrodes which were covered by Teflon tape, anhydrous were treated with an toluene containing 6 weight% 3aminopropyltrimethoxysilane (APS) for 6 hours at 70 °C. The resulting films were washed with toluene, acetone, and ethanol before being suspended in a 1 mM aqueous solution of the Co₉POM. The electrodes were then rinsed three times with 5-mL portions of water and dried in air. Finally, the top area of the electrodes was connected with a conductive copper tape and sealed with Epoxy adhesive (Henkel Loctite Hysol 1C Epoxi). The attachment of H₃PW₁₂O₄₀ to the TiO₂ photoelectrode is the same as that of Co₉POM. The TiO₂ photoelectrode coated with cobalt-phosphate water oxidation catalyst (Co-Pi)⁴⁷ was prepared according to the literature. 48, 49 A three-electrode cell was used with a TiO2 working electrode, Ag/AgCl (1 M KCl) reference electrode, and Pt mesh counter electrode. A potential of 0.9 V vs. Ag/AgCl was applied to a solution of 0.5 mM cobalt nitrate in 0.1 M potassium phosphate buffer at pH 7. The Co-Pi deposition time is 300 s and the current densities was around 8 µA/cm².

4.2.3 Photoelectrochemical Studies

Cyclic voltammograms (CVs), linear sweep voltammograms (LSVs) and bulk electrolysis data were obtained using a BAS CV-50W electrochemical analyzer and conducted at room temperature (25 ± 2 °C) in a custom 50 mL quartz cell (C012-2, Gaoss Union) equipped with airtight adapters and purged with argon gas prior to use. Mott-Schottky and AC impedance measurements are performed with a CHI 660e electrochemical station in the same quartz cell. CVs and LSVs were recorded in a standard three-electrode configuration with a glassy carbon working electrode (S = 0.07 cm²) or a Co₉POM-coated FTO working electrode (S = 1.0 cm²), a platinum wire counter electrode and a 3 M KCl Ag/AgCl (+0.210 V vs. RHE) reference electrode in a 0.1 M pH = 2 sulfate buffer solution as determined by an Orion pH meter (model 230A). In this work, all potentials measured against Ag/AgCl were then converted to the reversible hydrogen electrode (RHE) scale using: E(potential, versus RHE) = E (versus Ag/AgCl) + 0.210 V + 0.0591xpH. The scan rate used in voltametric experiments was 100 mV/s. A 100 mW/cm² 365 nm LED light was focused on the photoelectrode. Bulk electrolysis was conducted in a 0.1 M pH = 2 sulfate buffer solution with the potential held at 0.73 V vs. RHE under 20 mW/cm² 365 nm LED UV illumination. TiO₂-Co₉POM photoanode was used as a working electrode in bulk electrolysis in a H-cell (C012-1, Gaoss Union) with a Nafion 115 proton exchange membrane platinum wire counter electrode from working and reference chamber. The headspace during bulk electrolysis was then analyzed by GC as described in the methods section. The number of electrons transferred during bulk electrolysis was calculated by Faraday's law of electrolysis Q = nFN, where Q is the number of coulombs, F = 96485 C/mol is Faraday's constant, N is the moles of substrate electrolyzed and n is

the stoichiometric number of electrons consumed (4 in the case of the oxygen evolution reaction). Incident photon-to-current efficiency (IPCE) of TiO₂ and TiO₂-Co₉POM are measured under chopped light illumination under 1.23 V_{RHE} applied potential and calculated using the following equation:

$$IPCE = \frac{J_{ph} \times 1239.8}{P \times \lambda} \times 100\%$$

where J_{ph} (mA/cm²) is the photocurrent; P (mW/cm²) is the power density of monochromatic incident light; λ (nm) is the wavelength of monochromatic light; and 1239.8 (V nm) is a coefficient from the multiplication of speed of light, reciprocal of unit charge and Planck's constant.

4.2.4 Transient Absorption (TA) Spectroscopy Studies

Both visible TA and mid-IR TA spectroscopy pump probe are derived from an amplified Ti:sapphire laser system (Coherent Astrella, 800 nm, 5 mJ/pulse, 35 fs, and1 kHz repetition rate).

In TA-vis experiments, 40% of 800 nm fundamental output (2 mJ) is used to pump a visible Optical Parametric Amplifier (OPA) (Opera, Coherent) to generate a visible light as a pump in TA-vis experiments. In visible OPA, two tunable near-IR pulses, signal and idler, from 1.1 to 2.5 µm are generated. Signal and idler beams were separated with a dichroic mirror to generate tunable visible pump beam by sum-frequency generation with 800 nm or second-harmonic generation on a BBO crystal. In our study, 350 nm pump beam was generated by fourth-harmonic generation of 1400 nm signal beam. A continuously variable neutral-density filter wheel was used to adjust the power of the pump beam. The pump beam was focused on the sample with a beam waist of about 420

μm. 10% of 5mJ/pulse output is used to generate a white light continuum from 380 to 700 nm on a single crystal CaF₂ as a probe of TA-vis experiments. The WLC was split into a probe and reference beam. The probe beam was focused with an Al parabolic mirror on the sample with a beam waist of 150 μm. After passing the sample, the probe beam was focused on a fiber-coupled multichannel spectrometer with complementary metal-oxide-semiconductor (CMOS) sensors and detected at a frequency of 1 kHz. The delay between the pump and probe pulses was controlled by a motorized probe delay stage. The pump beam was chopped by a synchronized chopper to 500 Hz. The change in absorbance of the samples with and without pump was calculated. The samples used in TA-vis experiments are deposited on FTO glass. The instrument response function (IRF) of this system was measured to be ~300 fs by measuring the pump-probe response on a FTO substrate.

In TA-IR experiment, output from the same visible OPA is used as pump beam, it was focused on the IR sample stage with a beam waist of 410 µm. 40 % of 800 nm fundamental out (2 mJ) is used to pump an IR OPA (Opera, Coherent). Two tunable near-IR signal and idler pulses from 1.1 to 2.5 µm were generated. The singal and idler pulses were further combined in a 1-mm-thick AgGaS₂ crystal to generate a tunable mid-IR pulse from 3 to 10 µm by difference frequency generation (DFG). The mid-IR beam was focused on the sample stage at a beam waist of around 290 µm to overlap with pump beam. After passing the sample, mid-IR probe was dispersed into a spectrograph and detected with a 32-element infrared HgCdTe (MCT) array detector at a frequency of 1k Hz. The pump beam was chopped by a synchronized chopper to 500 Hz. The typical IRF of TA-IR

experiments was determined to be ~ 240 fs using a silicon wafer. The sample used in TA-IR experiments are deposited on a sapphire window to avoid strong IR absorption of FTO.

4.3 Results and Discussion

4.3.1 Characterization of TiO₂ and TiO₂-Co₉POM photoelectrodes

Co₉POM and TiO₂ photoelectrodes coated with Co₉POM (referred to as TiO₂-APS-Co₉POM or TiO₂-Co₉POM) were synthesized as described in the experimental section. The Fourier transform infrared (FT-IR) spectrum (Figure 4.1a) of Co₉POM has characteristic Keggin structure peaks at 803 cm⁻¹ ν (W-O_c-W, c = octahedral edge-sharing), 886 cm⁻¹ ν (W-O_b-W, b = octahedral corner-sharing), 935 cm⁻¹ ν (W-O_d, d = terminal), and 1029 cm⁻¹ $v(P-O_a, a = tetrahedral)$. Another prominent peak at 716 cm⁻¹ corresponds to ν (Co-O-Co) stretching. These peaks are consistent with the literature assignments⁵⁰, thereby confirming the presence of Co₉POM: infrared bands represent a reliable fingerprint for molecular structure in POM chemistry. The number of water molecules in Co₉POM is calculated to be 49 based on the thermogravimetric data (Figure 4.1b). After treatment of TiO₂ nanoporous films with the cationic silylating agent (APS), anionic Co₉POM is absorbed onto the TiO₂ photoelectrode via strong electrostatic interaction. Raman spectroscopy confirmed the attachment of Co₉POM on TiO₂ as shown in Figure 4.2. Four characteristic peaks at 151 cm⁻¹, 390 cm⁻¹, 505 cm⁻¹, 626 cm⁻¹ are observed on TiO₂, corresponding to E_g, B_{1g}, A_{1g}, and E_g of anatase phase of TiO₂ (black diomond).⁵¹, ⁵² Co₉POM characteristic peaks (red stars) are observed on solid Co₉POM consistent with previous report.³⁵ On TiO₂-Co₉POM, both TiO₂ and Co₉POM characteristic peaks can be identified simultaneously, confirming the successful surface immobilization. The diffuse reflectance spectra (Figure 4.3) of TiO₂, TiO₂-APS, and TiO₂-APS-Co₉POM all

show a band-edge absorption around 390 nm (3.2 eV). TiO₂ and TiO₂-APS have a similar and small absorption in the visible region but TiO₂-APS-Co₉POM has a higher absorption due to the presence of surface-bound Co₉POM.

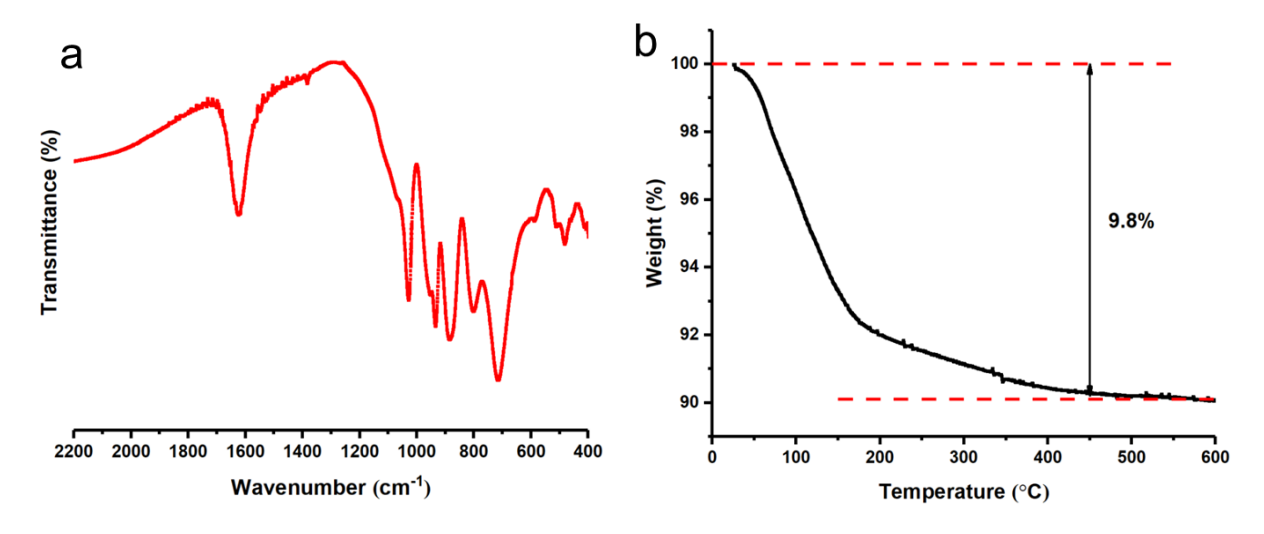


Figure 4.1. FT-IR spectroscopy (a) and TGA (b) of Co₉POM.

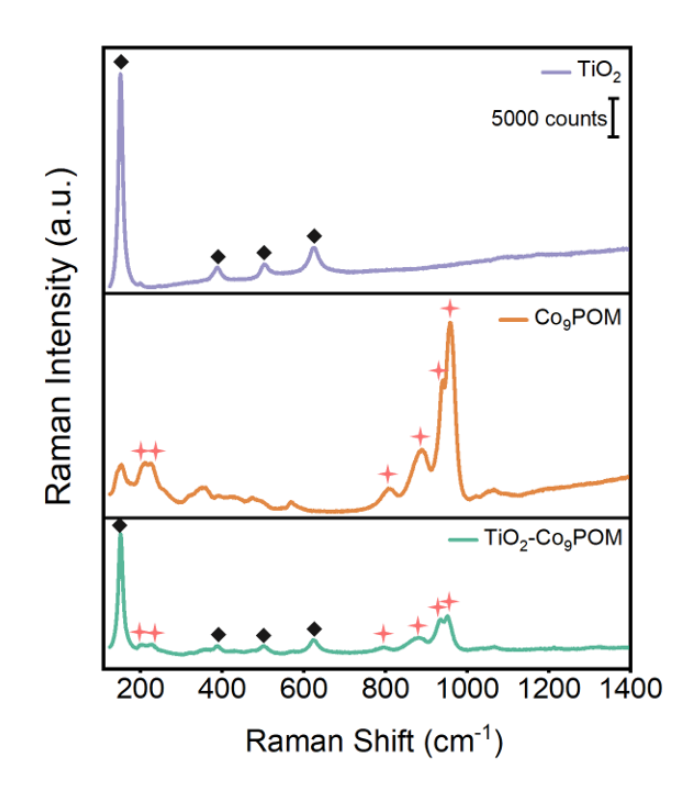


Figure 4.2. Raman spectra of TiO₂, TiO₂-APS-Co₉POM on the FTO electrode and Co₉POM solid.

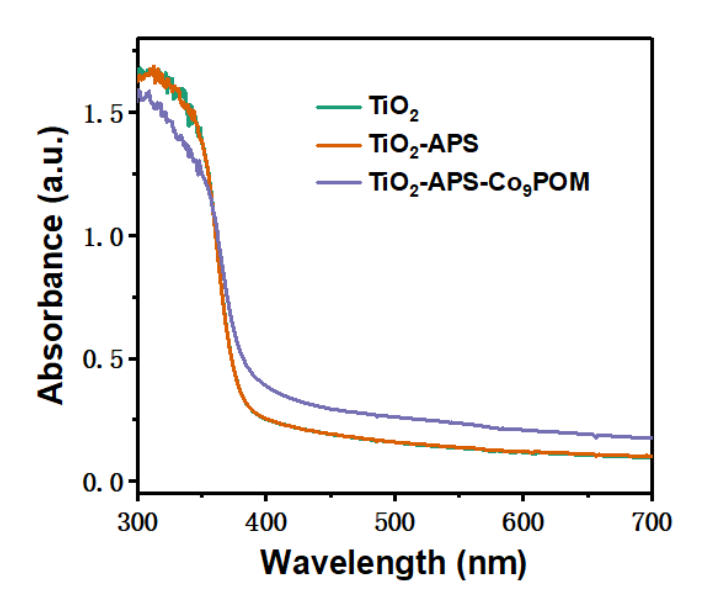


Figure 4.3. Diffuse reflectance spectra of TiO₂, TiO₂-APS, and TiO₂-APS-Co₉POM.

To further assess the incorporation of Co₉POM on the TiO₂ photoelectrode, X-ray photoelectron spectroscopy (XPS) was conducted on the TiO₂-APS-Co₉POM film. Figure 4.4 shows the full XPS spectrum of TiO₂-APS-Co₉POM, which confirms the existence of TiO₂ (Ti 2p peak and O 1s peak), APS (C 1s peak, N 1s peak, and Si 2p peak), and Co₉POM (Co 2p peak, W 4f peak, and O 1s peak). The XPS spectrum of Ti 2p (Figure 4.5a) has significantly split spin-orbit components (Δ_{oxide} = 5.7 eV) with the Ti 2p_{3/2} peak and the Ti 2p_{1/2} peak located at 458.5 eV and 464.2 eV, respectively. A broad satellite peak at 472 eV is consistent with the literature.⁵³ The signal to noise ratios of these Ti peaks are understandably low because TiO₂ surface is covered by APS and Co₉POM. The XPS spectrum of W 4f (Figure 4.5b) shows the binding energy of 35.28 eV (4f_{7/2}) and 37.48 eV (4f_{5/2}), which are typical for tungsten in the VI oxidation state. The loss feature for W(VI) at 41 eV is also observed. Figure 4.6a displays the XPS spectrum of Co 2p with the binding energies of 780.7 eV (2p_{3/2}) and 797.1 eV (2p_{1/2}). Associated with these peaks are two observable satellite peaks at 786.4 eV and 803.0 eV. These features correspond

to the Co(II) oxidation state and will be used for comparison in the following characterizations. The O 1s XPS spectrum in Figure 4.6b could be fitted with two peaks located at 530.5 eV and 532.2 eV, which are assigned to oxygen atoms in the chemical environment of W-O (POM) and Si-O (APS), respectively. The ICP experiment quantifies a Co loading of 7.7 μ g/cm² sample geometric area.

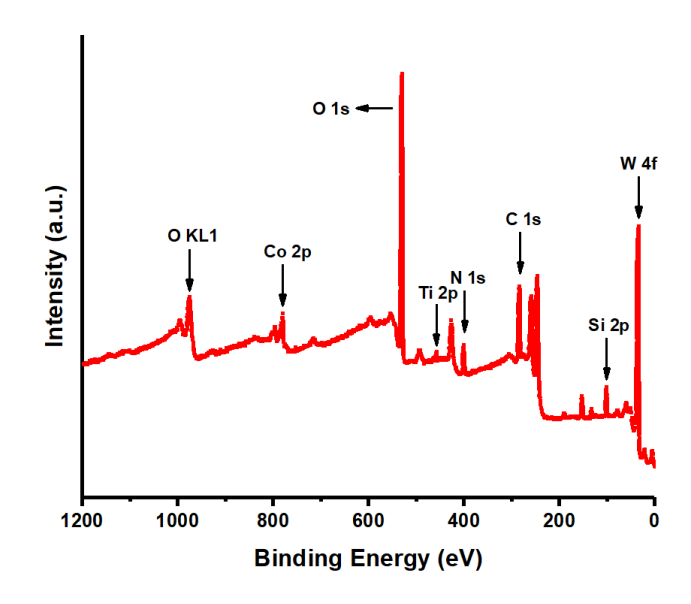


Figure 4.4. XPS of TiO₂-APS-Co₉POM.

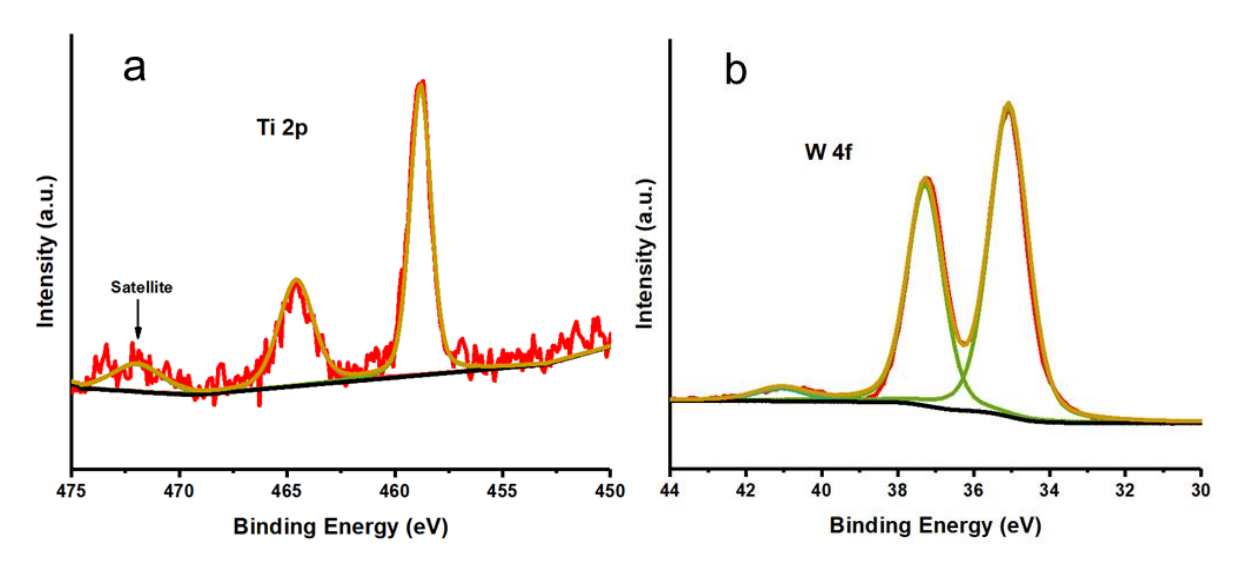


Figure 4.5. XPS of (a) Ti 2p and (b) W 4f in TiO₂-APS-Co₉POM.

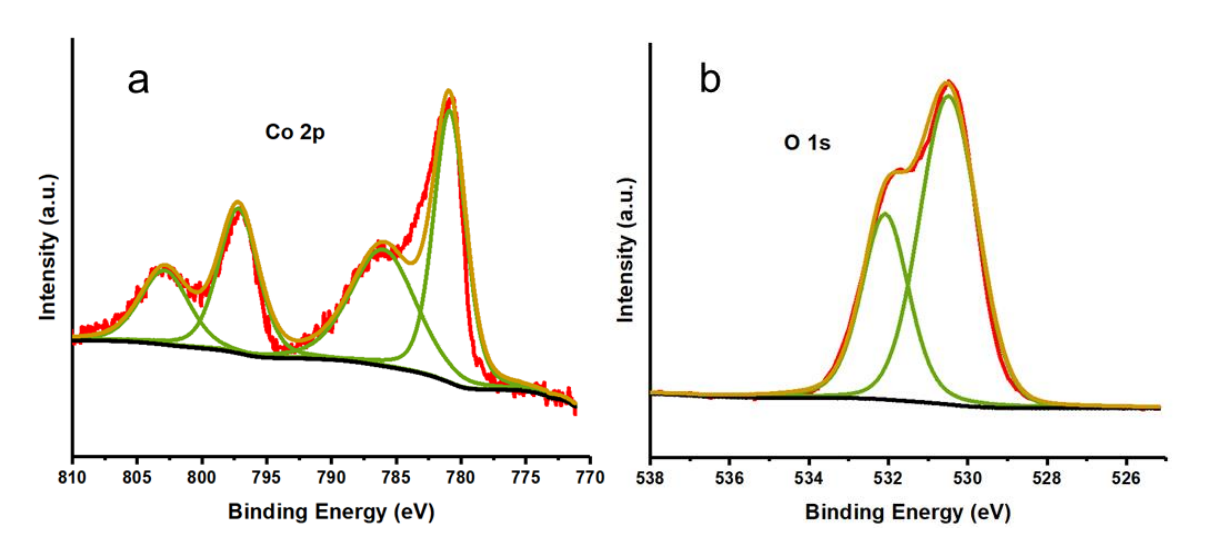


Figure 4.6. XPS of (a) Co 2p and (b) O 1s in TiO₂-APS-Co₉POM.

4.3.2 Photoelectrochemical Oxygen Evolution by TiO₂-Co₉POM

The details of (photo)electrochemical studies of Co₉POM and TiO₂-Co₉POM photoelectrode are described in the experimental section. The effect of the Co₉POM modification on TiO₂ photoelectrode is evaluated by linear sweep voltammograms and open circuit photovoltage as shown in Figure 4.7. Under the dark environment, TiO₂ and TiO₂-Co₉POM electrodes exhibit negligible current when scanned to positive potentials, though there is an oxidation peak at around 0.0 V vs. RHE that is attributed to Ti(III)/Ti(IV) redox couple.⁵⁴ When the UV light is turned on, the photocurrent increases substantially and reaches plateau at around +0.25 V vs. RHE for both TiO₂ and TiO₂-Co₉POM. The saturated photocurrent of TiO₂-Co₉POM is nearly three times that of TiO₂. Figure 4.7b shows the open circuit measurement with the arrow indicating light on and off. The open circuit potential (OCP) of TiO₂ and POM-modified TiO₂ are similar under dark condition at ~290 mV. Under UV illumination, however, the OCP of TiO₂-Co₉POM (-170 mV) is more negative than that of TiO₂ (-80 mV). More interestingly, OCP of TiO₂-Co₉POM shows a slower recovery to its dark equilibrium potential when the light is off compared to pure

TiO₂ (Figure 4.7b). These phenomena can be attributed to the synergic effect of band edge modification and the charge transfer effect. The first effect can be confirmed by around 100 mV more negative flat-band potential (Efb) of TiO₂-Co₉POM (-0.16 V_{RHE}) compared to TiO₂ (-0.83 V_{RHE}) and TiO₂-APS extracted from Mott-Schottky analysis (Figure 4.8a). The highly charged Co₉POM modifies the conduction and valance band edge, enabling a faster electron-hole separation and a higher electron concentration build-up, i.e., OCP_{light}, under illumination. As an efficient water oxidation catalyst, Co₉POM can also extract and store photogenerated holes, resulting in a larger OCP photovoltage and slower electron-hole recombination (Figure 4.9).

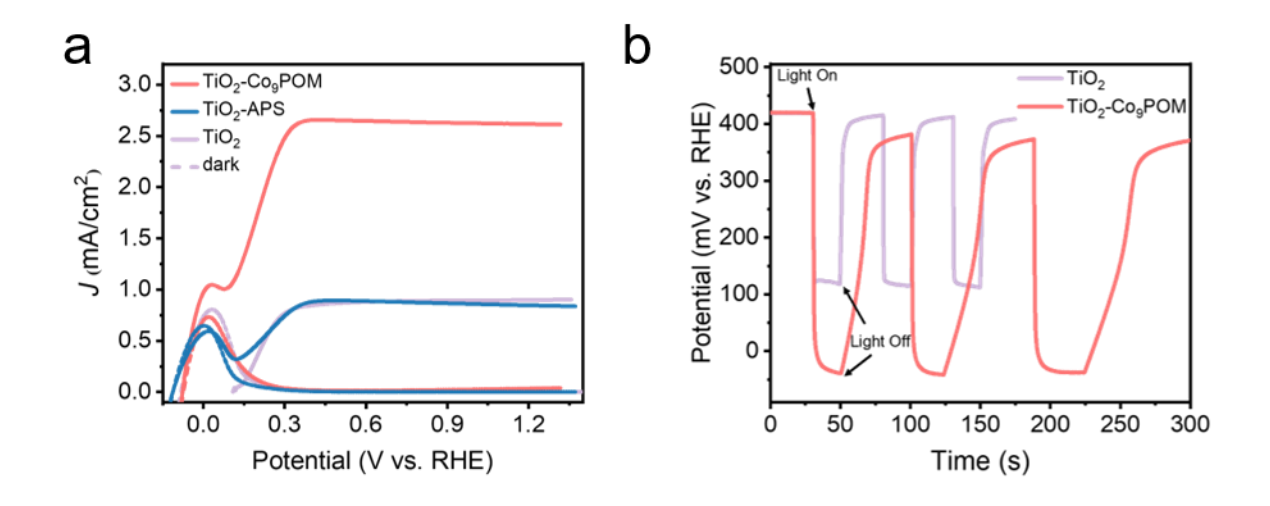


Figure 4.7. Linear sweep voltammogram (a) and open circuit photovoltage (b) of TiO₂ and TiO₂-Co₉POM. Both experiments are performed under 100 mW/cm² 365 nm illumination.

AC impedance measurements are performed on TiO₂, TiO₂-APS, and TiO₂-Co₉POM to further reveal the function of APS and the catalyst effect of Co₉POM under light illumination. As shown in Figure 4.8b and Table 4.1, TiO₂-Co₉POM exhibits a smaller trapping resistance and large capacitance compared to TiO₂ and TiO₂-APS, which can be attributed to the hole extraction and storage properties of Co₉POM. The impedance

between TiO₂ and TiO₂-APS samples, however, are very similar. Together with the LSV performance and Mott-Schottky experiments, we believe that APS ligands behave more as a spectator than as a passivation layer on TiO₂.

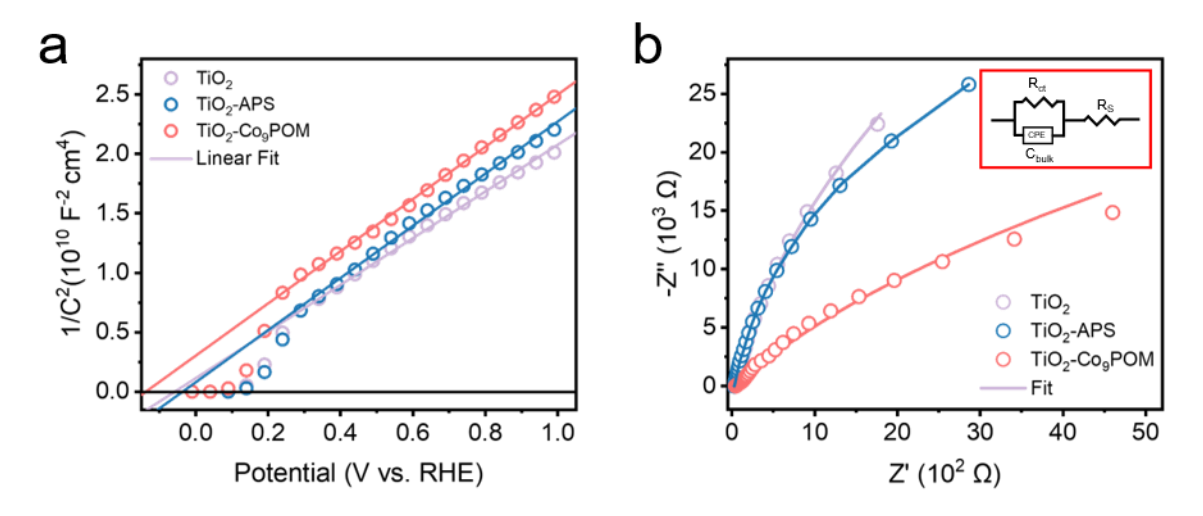


Figure 4.8. (a) Mott-Schottky and (b) Nyquist plot of electrochemical impedance spectroscopy of TiO₂, TiO₂-APS, and TiO₂-Co₉POM, respectively. Mott-Schottky is conducted under 500 Hz frequency, AC impedance is performed at 1.23 V_{RHE} under 12.8 mW/cm² 365 nm UV illumination.

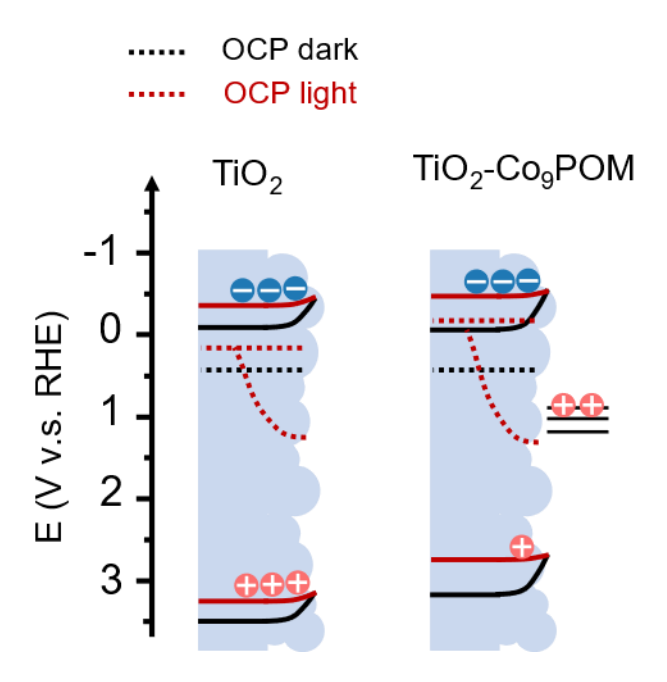


Figure 4.9. Band structure schematic of TiO₂ and TiO₂-Co₉POM under illumination and dark OCP process.

Table 4.1. AC impedance fitting paramater of TiO₂, TiO₂-APS and TiO₂-Co₉POM photoanode

	TiO ₂	TiO ₂ -APS	TiO ₂ -
	IIO ₂	HO2-AP3	Co ₉ POM
Ufb	-	-	-
(V _{RHE})	0.083±0.017	0.062±0.020	0.164±0.009
Rs			
(Ohm	25.41 <u>+</u> 0.17	27.88 <u>+</u> 0.12	46.32 <u>+</u> 0.28
cm ⁻²)			
Rct			
(kOhm	567.8 <u>+</u> 292	410.3 <u>±</u> 80.6	153.3 <u>+</u> 28.2
cm ⁻²)			
CPE-			
Q (μF	7.70 <u>+</u> 0.10	6.67 <u>+</u> 0.05	126.2 <u>+</u> 0.16
cm ⁻²)			
CPE-	0.978±0.002	0.979±0.001	0.904±0.002
α	0.870 <u>1</u> 0.002	0.979 <u>1</u> 0.001	0.30410.002

Excitation fluence-dependent photocurrent densities of TiO₂, TiO₂-APS, and the TiO₂-Co₉POM photoanode are given in Figure 4.10. Corresponding calculated incident photon-to-current efficiencies (IPCEs) are as shown in Figure 4.10b. TiO₂ and TiO₂-APS show a steady IPCE of around 5% regardless of illumination intensity. Notably, IPCE of

TiO₂-Co₉POM remains unchanged at around 18% before 6.4 mW/cm², while it decreases at a higher intensity. This means that the catalysts turnover rate lag behind the photogeneration rate at higher illumination intensity, shifting the efficiency limiting step from photon generation to catalyst loading.

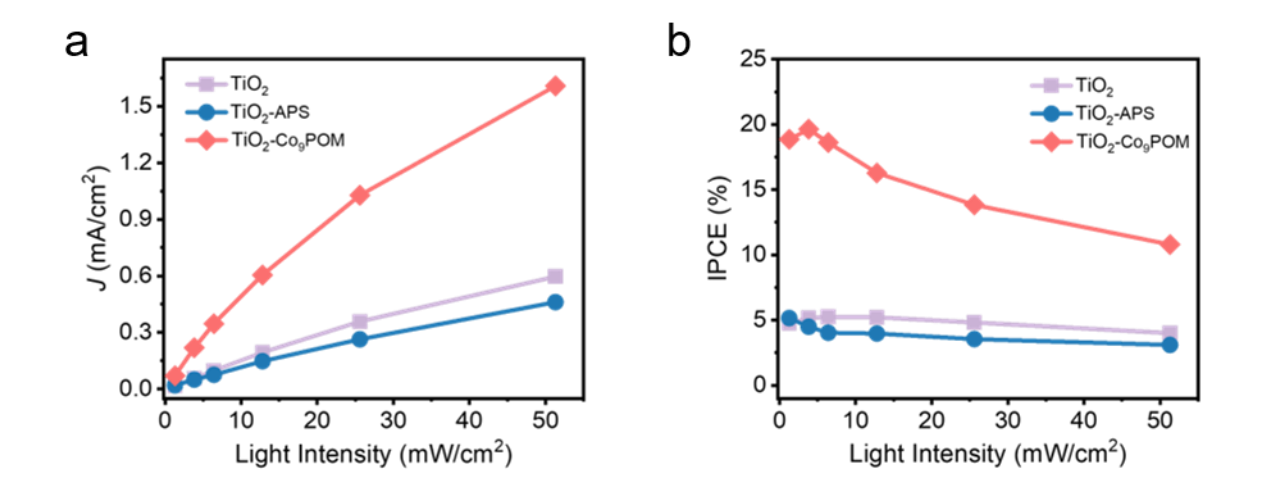


Figure 4.10. (a) Photocurrent density measured at 1.23 V_{RHE} and (b) corresponding IPCE of TiO₂, TiO₂-APS, and TiO₂-Co₉POM plotted as a function of 365 nm illumination power density.

The stability test of TiO₂-Co₉POM is carried out under chronoamperometric conditions under 0.73 V_{RHE} applied potential and 20 mW/cm² 365 nm UV illumination. As shown in Figure 4.11a, the photoanode exhibits a stable photocurrent throughout 5-hour test passing around 3 coulombs of charge. The initial fast decay is related to the capacitance, a non-Faradaic process, which is also reported in the previous literature.³⁵ The Co and W peaks in the XPS of the photoanode were well-maintained after 5 hours of use (Figures 4.11b-d), which are different from XPS peaks of CoO_x (Figure 4.12) thus indicating the structural integrity over this time-scale. All these data showed that Co₉POM-modified TiO₂ acts as a highly efficient and stable system.

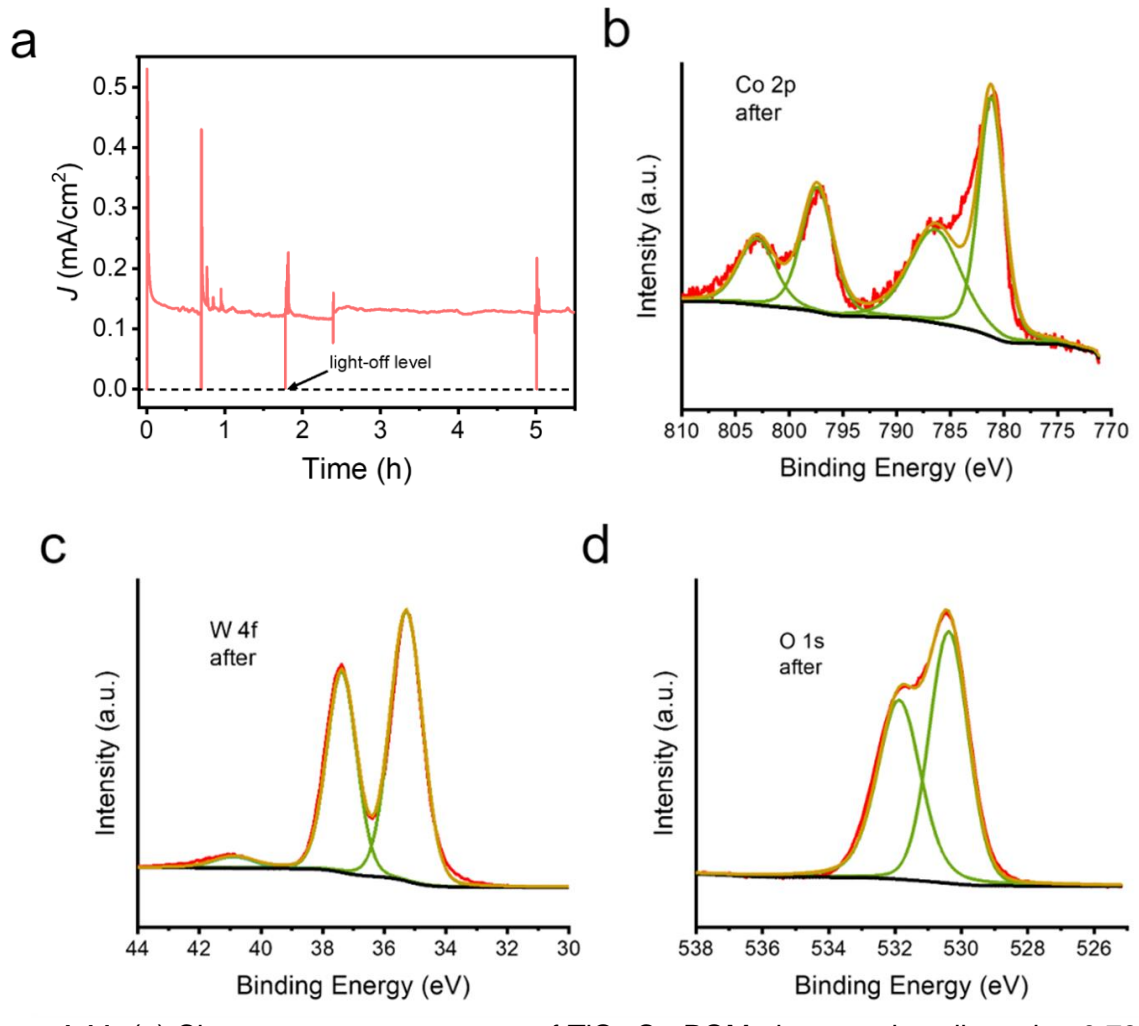


Figure 4.11. (a) Chronoamperometry curve of TiO_2 - Co_9POM photoanode collected at 0.73 V_{RHE} under 20 mW/cm² 365 nm UV illumination. (b)-(d) XPS test of Co 2p, W 4f, O 1s after stability test, respectively.

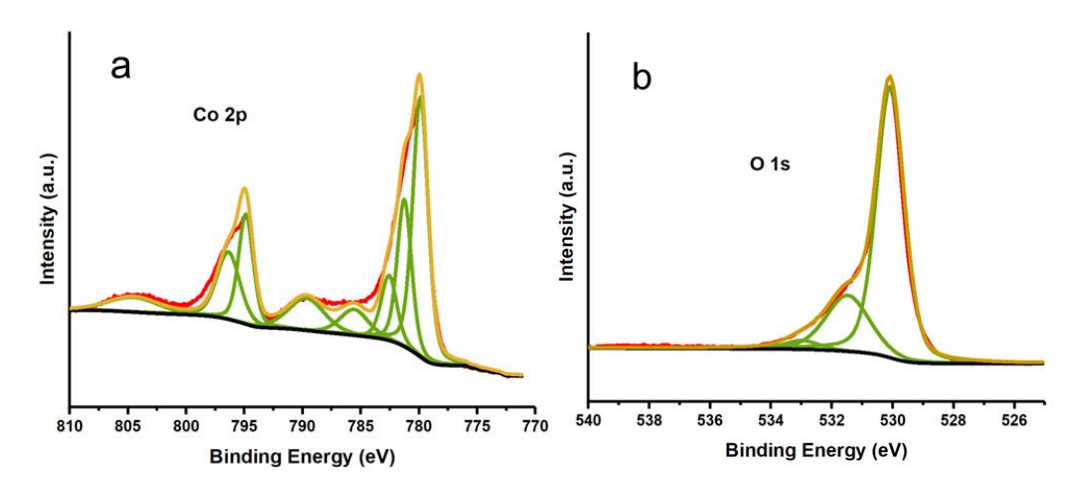


Figure 4.12. XPS of (a) Co 2p and (b) O 1s in CoO_x.

Control experiments using the non-transition-metal substituted POM and Co-Pi modified TiO₂ photoelectrodes were also conducted to confirm the indispensable role of Co₉POM for catalytic water oxidation reaction in aqueous acid. As shown in Figure 4.13, both H₃PW₁₂O₄₀ and Co-Pi coated TiO₂ photoelectrodes exhibit inferior activity relative to the pure TiO₂ photoelectrode. The lack of a catalytic metal center in the H₃PW₁₂O₄₀-modified TiO₂ leads to decreased photocurrent. This also confirms that it is Co center rather than Keggin polyanion that acts as the water oxidation active site. In addition, although Co-Pi has been extensively reported as a superior water oxidation co-catalyst in neutral and alkaline solutions,^{47, 55-57} it does not act as an efficient catalyst in acidic condition. It likely blocks the water oxidation reaction sites on TiO₂, leading to a worse performance.

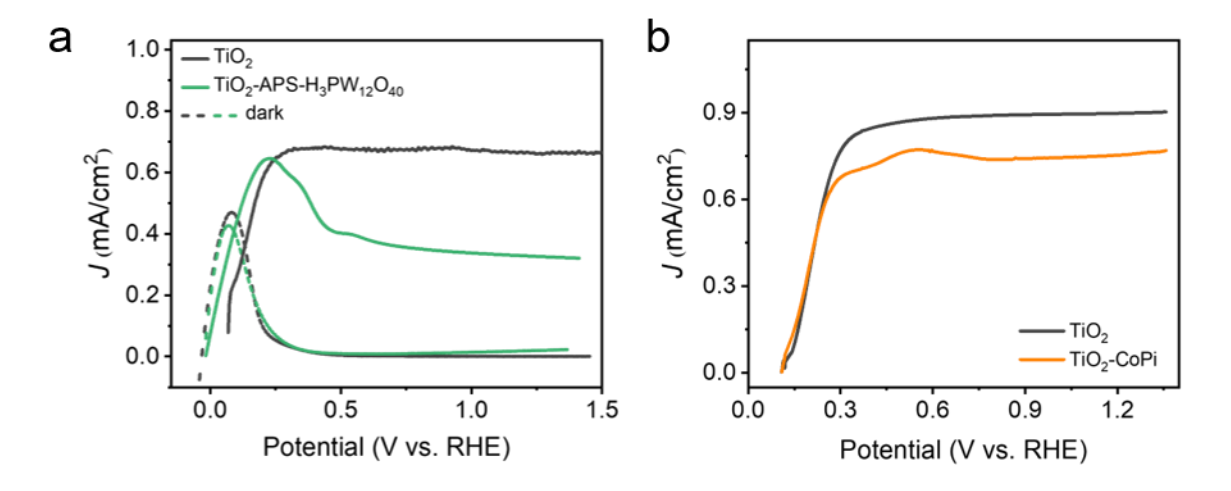


Figure 4.13. (a) J-V curve of H₃PW₁₂O₄₀ and (b) J-V photocurrent of Co-Pi modified TiO₂ under 100 mW cm⁻² 365 nm LED light illumination.

4.3.3 Transient Absorption Spectroscopies of TiO₂-Co₉POM

To further elucidate the charge carrier dynamics in TiO₂-Co₉POM, transient absorption (TA) spectroscopy has been applied to study the photo-physics of this

photoanode in both visible (TA-vis) and mid-IR (TA-IR) regions as shown in Figure 4.15. Before detailed analysis of TA spectra and kinetics of TiO₂-Co₉POM, a series of control experiments were done on TiO₂ to assign the spectral features observed in the visible range after excitation. As shown in Figure 4.14a and Figure 4.15a, similar broad positive signals were observed upon excitation on both TiO₂ and TiO₂-Co₉POM. The broad signal in the visible range is assigned to be a convolution contribution of both electron and hole signals, where the trapped hole and electrons have absorption peaks at 520 and 770 nm by previous reports.⁵⁸⁻⁶⁰ We extracted the kinetics from 460-520 nm and compare their decay behavior in DI H₂O, an electron scavenger solution (0.1 M Na₂S₂O₈ aqueous solution), and a hole scavenger solution (30% methanol aqueous solution) as shown in Figure 4.14d. Compare to kinetics in DI H₂O, the kinetics decay much faster in 30% methanol solution and slightly slower in electron scavenger solution. This indicates that the kinetics from 460-520 nm mainly originated from photogenerated holes in nanocrystalline TiO₂ and agrees well with previous assignments. Kinetics at this range can be further used to represent the kinetic decay of photogenerated holes.

Excitation fluence-dependent hole kinetic decays are done and compared in Figure 4.14b and c. Interestingly, the maximum signal amplitude scales linearly with power density, but signal decay half-time and signal residual decay with increased excitation power. This means that the amount of photogenerated holes linearly scales with excitation power, but recombines faster with more generated carriers. These can be explained by the trap-assisted electron-hole recombination nature. Fluence-dependent hole kinetics can be well-fitted by a power law decay $A = (t-t_0)^{-\beta}$, with β lying within 0.25 \pm 0.002 for all decays. The dispersive bimolecular recombination is in accordance with

metal oxides and organic semiconductor materials.⁶¹⁻⁶⁴ The hole kinetics decay in TiO₂, TiO₂-APS, and TiO₂-Co₉POM samples are compared in Figures 4.14e and 4.15b. The hole decay kinetics are similar in TiO₂ and TiO₂-APS, while the signal decay is accelerated in TiO₂-Co₉POM. This further confirms the previous conclusion: Co₉POM acts as a water oxidation catalyst that can extract photogenerated holes at ultrafast timescale, while APS acts as a spectator and does not affect the hole kinetics.

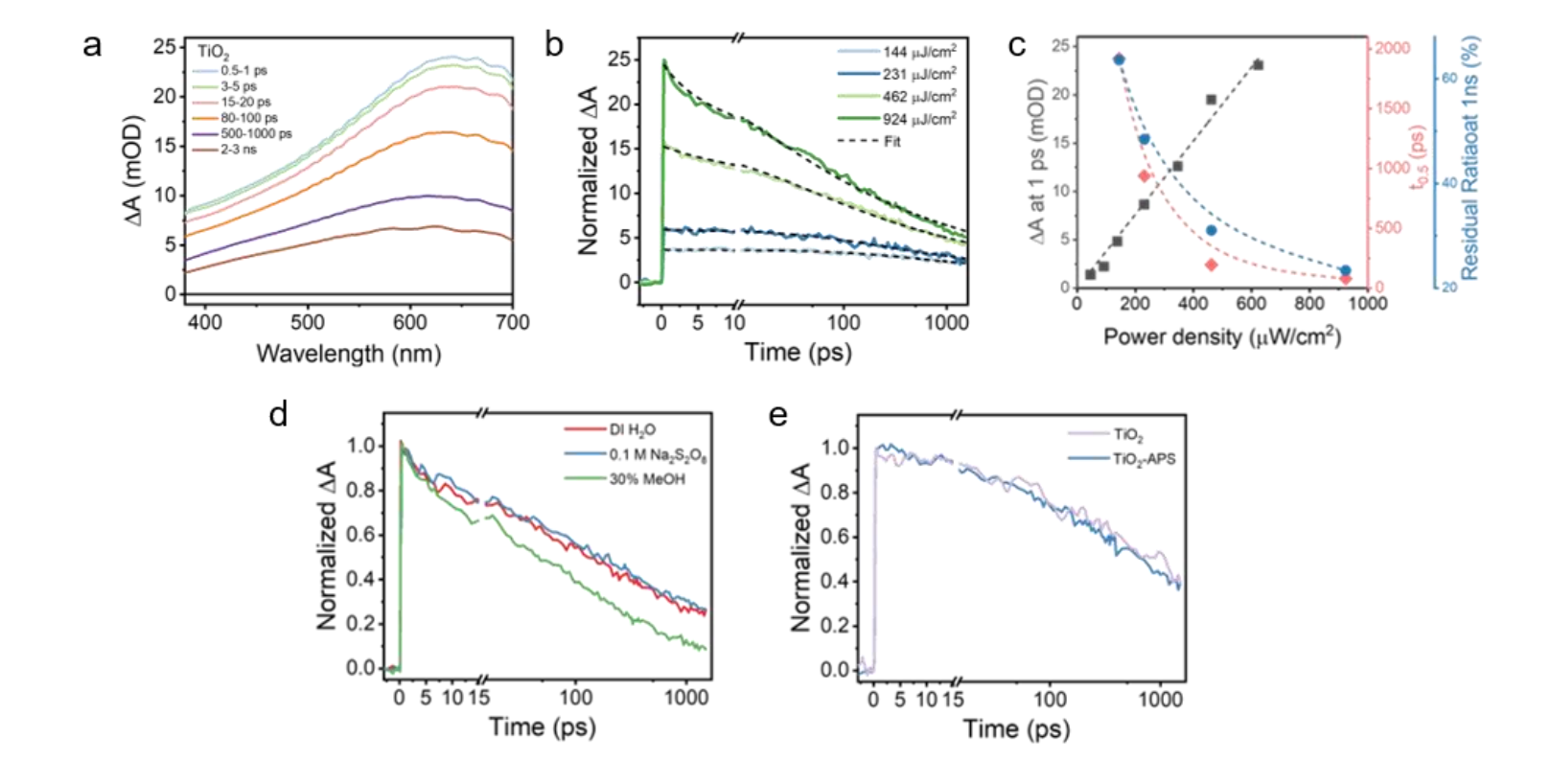


Figure 4.14. Transient absorption spectroscopy of TiO_2 on FTO pumped by 350 nm probe by visible white light: (a) TA-vis spectra; excitation fluence dependence of (b) kinetic decay and (c) maximum signal amplitude, half lifetime and signal residual; (d) kinetic decay in DI water, 0.1 M Na₂SO₄, and 30% methanol; (e) kinetic decay of TiO_2 and TiO_2 -APS compared. All signal kinetics decays are extracted by averaging 460-520 nm; an excitation power density of 462 μJ/cm² was used in (a), and 231 μJ/cm² was used in (d) and (e).

Furthermore, TA-IR spectroscopy is conducted on TiO₂, TiO₂-APS, and TiO₂-Co₉POM samples to probe the photogenerated electron kinetics in the TiO₂ conduction band as shown in Figure 4.15 c, d, and Figure 4.16. All samples showed a broad positive signal in the IR range from 2000 to 2080 cm⁻¹ upon excitation. The signal can be assigned to the free electron absorption at TiO₂ conduction band. 65-67 The contribution of Co₉POM or APS excited states or oxidized states are excluded in the TA-IR spectra, judging from the lack of IR transitions in this region.⁶⁸ As shown in Figure 4.16d, the electron signal in TiO₂ shows a similar decay feature with or without APS-present, indicating that APS is not reduced by TiO₂ conduction band electrons and remains stable. Notably, the electron signal decays faster when Co₉POM is attached to TiO₂-APS. This can be explained by TiO₂ conduction band electrons reducing tungsten in Co₉POM due to its favorable energetics (~-0.1 VRHE, Figure 4.17)⁶⁹ compared to TiO₂ conduction band edge (-0.4 VRHE). Despite this unfavorable electron transfer process observed in dry film TA-IR measurement conditions, we believe this effect will be greatly mitigated during OER condition as sufficient applied positive potential can decrease the electron population in nanocrystalline TiO₂. In summary, from the above TA-vis and TA-IR experiments, we identify the TiO₂-Co₉POM to be a highly coupled system that can achieve both electron and hole transfer, owing to the APS ligand serving as both electron and hole transfer highway.

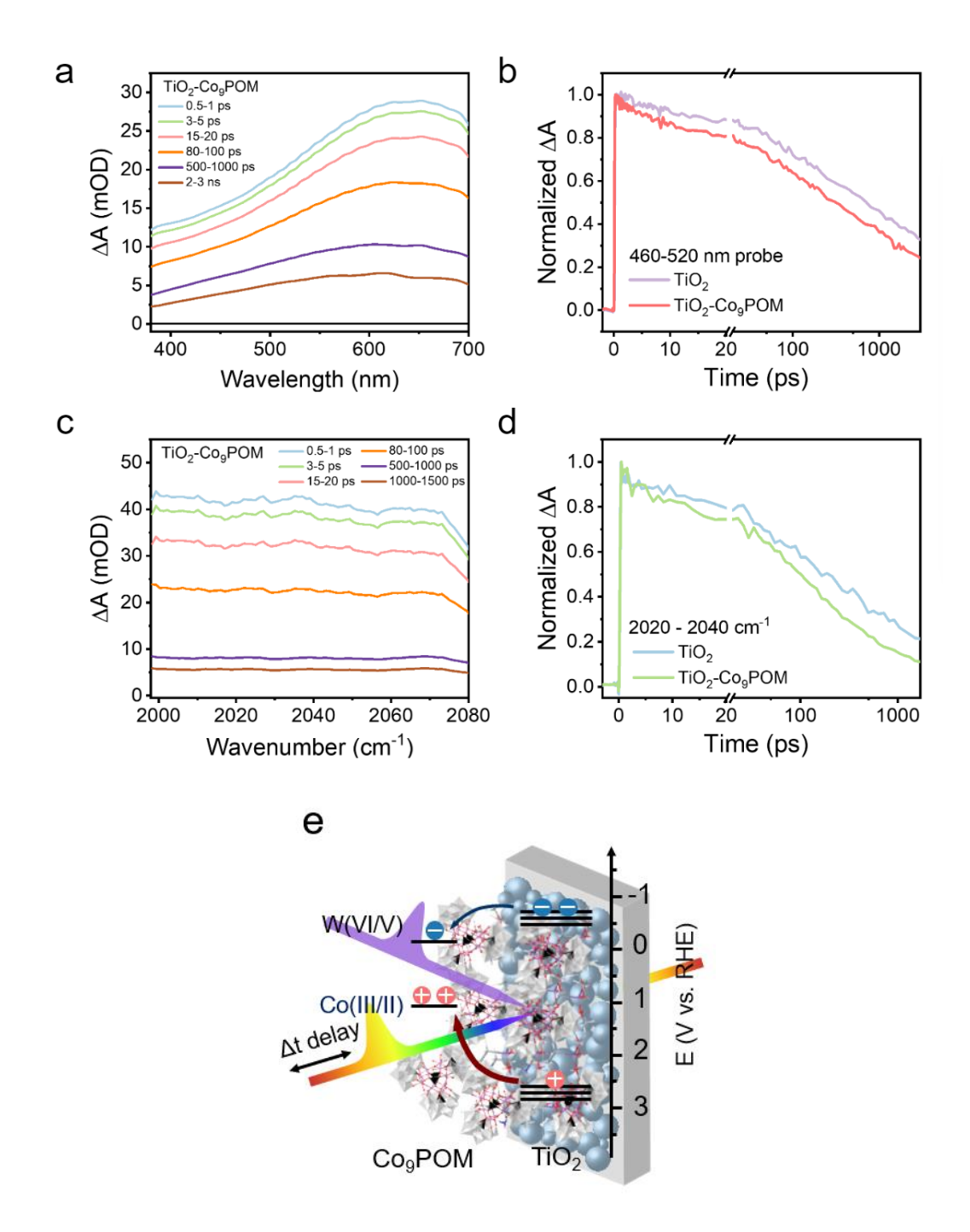


Figure 4.15. Transient absorption spectra of TiO_2 - Co_9POM under 350 nm pump using a (a) visible and a (b) mid-IR probe. Transient absorption decay kinetics of TiO_2 and TiO_2 - Co_9POM compared in the (b) 460-520 nm visible and (d) 2020-2040 cm⁻¹ regions. (e) Schematic illustration of the charge transfer mechanism between TiO_2 and Co_9POM . Samples for TA-vis experiments are deposited on FTO substrates, samples for TA-IR experiments are deposited on sapphire windows to avoid extensive absorption by tin oxide. An excitation power density of 462 μJ/cm² is used in all experiments.

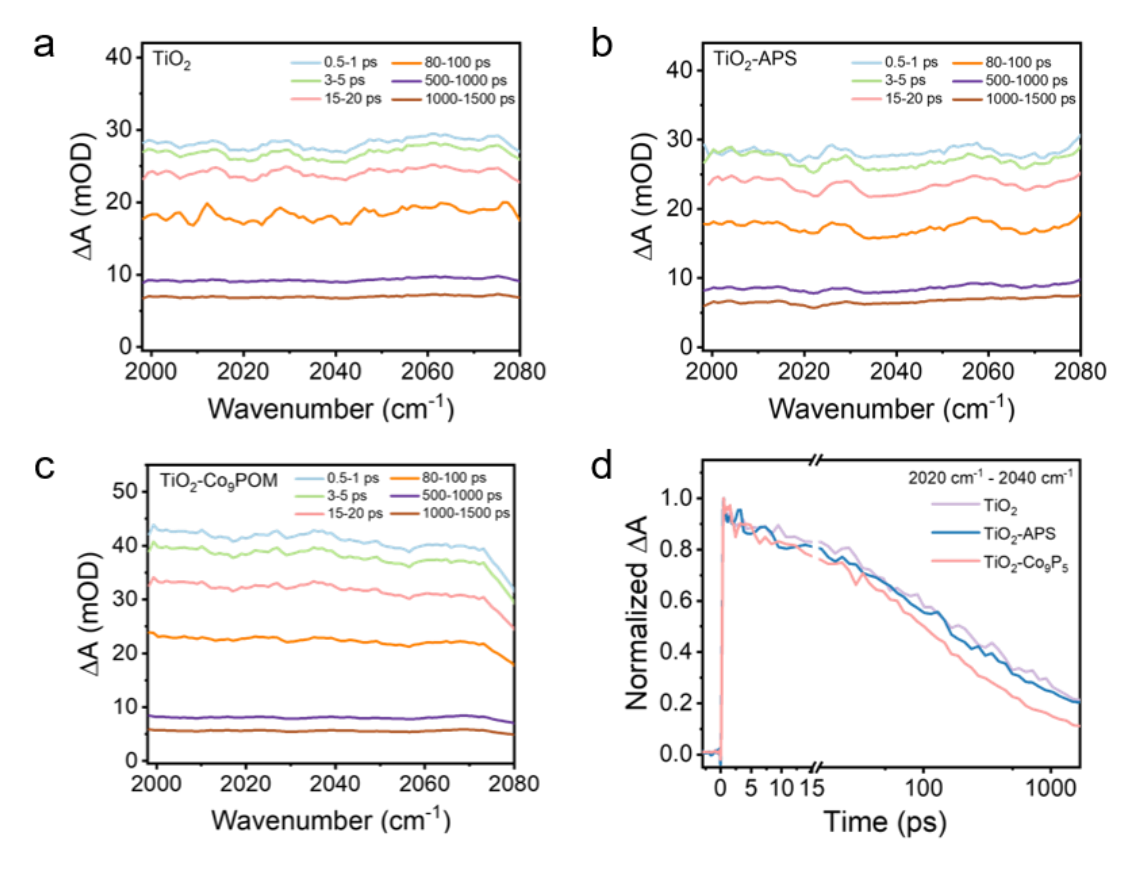


Figure 4.16. TA-IR spectra of (a) TiO₂, (b) TiO₂-APS, and (c) TiO₂-Co₉POM samples. (d) Kinetics comparison of three samples from 2020-2040 cm⁻¹. TA-IR experiments are conducted under 462 μJ/cm² 350 nm pump, samples are all deposited on the sapphire window.

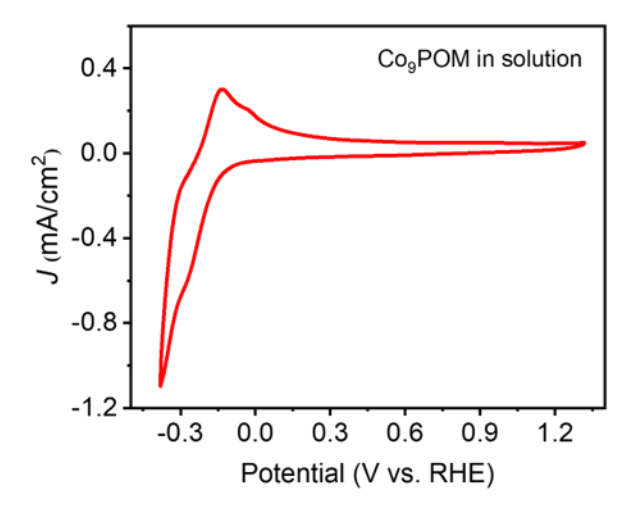


Figure 4.17. Cyclic voltammetry of Co₉POM in pH 2 sulfate buffer solution.

4.4 Conclusions

- 1. By treating porous n-type TiO_2 with cationic 3-aminopropyltrimethoxysilane (APS), $Na_8K_8[Co_9(H_2O)_6(OH)_3(HPO_4)_2(PW_9O_{34})_3]$ (Co_9POM) is successfully introduced onto TiO_2 photoelectrodes via electrostatic interactions. Co_9POM -modified TiO_2 photoelectrodes exhibit an approximately three-fold OER enhancement of photocurrent compared to the unmodified TiO_2 in a sulfate buffer solution (pH = 2). This enhancement is maintained throughout bulk electrolysis while the surface-bound Co_9POM remains intact, which is confirmed by the X-ray photoelectron spectroscopy.
- 2. Open circuit photovoltage measurements and transient absorption spectroscopy in both the visible and mid-IR ranges are conducted to reveal the catalytic effect of Co₉POM. We conclude that Co₉POM serves as an efficient water oxidation catalyst, extracting photogenerated holes from TiO₂ at picosecond timescale. The functionalized Co₉POM layer also separates the photogenerated carriers and mitigates surface recombination by creating a favorable interfacial electric field.

4.5 References

- 1. Hu, S.; Shaner, M. R.; Beardslee, J. A.; Lichterman, M.; Brunschwig, B. S.; Lewis, N. S., Amorphous TiO₂ coatings stabilize Si, GaAs, and GaP photoanodes for efficient water oxidation. *Science* **2014**, *344*, 1005-1009.
- 2. Kim, T. W.; Choi, K. S., Nanoporous BiVO₄ Photoanodes with Dual-Layer Oxygen Evolution Catalysts for Solar Water Splitting. *Science* **2014**, *343*, 990-994.

- 3. Liu, J.; Liu, Y.; Liu, N.; Han, Y.; Zhang, X.; Huang, H.; Lifshitz, Y.; Lee, S. T.; Zhong, J.; Kang, Z., Metal-free efficient photocatalyst for stable visible water splitting via a two-electron pathway. *Science* **2015**, *347*, 970-974.
- 4. Trotochaud, L.; Ranney, J. K.; Williams, K. N.; Boettcher, S. W., Solution-cast metal oxide thin film electrocatalysts for oxygen evolution. *J. Am. Chem. Soc.* **2012**, *134* (41), 17253-17261.
- 5. Okamura, M.; Kondo, M.; Kuga, R.; Kurashige, Y.; Yanai, T.; Hayami, S.; Praneeth, V. K.; Yoshida, M.; Yoneda, K.; Kawata, S.; Masaoka, S., A pentanuclear iron catalyst designed for water oxidation. *Nature* **2016**, *530* (7591), 465-468.
- 6. Zhang, B.; Zheng, X.; Voznyy, O.; Comin, R.; Bajdich, M.; García-Melchor, M.; Han, L.; Xu, J.; Liu, M.; Zheng, L.; García de Arquer, F. P.; Dinh, C. T.; Fan, F.; Yuan, M.; Yassitepe, E.; Chen, N.; Regier, T.; Liu, P.; Li, Y.; Luna, P. D.; Janmohamed, A.; Xin, H. L.; Yang, H.; Vojvodic, A.; Sargent, E. H., Homogeneously dispersed multimetal oxygen-evolving catalysts. *Science* **2016**, *352*, 333-337.
- 7. Grimaud, A.; Diaz-Morales, O.; Han, B.; Hong, W. T.; Lee, Y. L.; Giordano, L.; Stoerzinger, K. A.; Koper, M. T. M.; Shao-Horn, Y., Activating lattice oxygen redox reactions in metal oxides to catalyse oxygen evolution. *Nat. Chem.* **2017**, *9* (5), 457-465.
- 8. Fei, H.; Dong, J.; Feng, Y.; Allen, C. S.; Wan, C.; Volosskiy, B.; Li, M.; Zhao, Z.; Wang, Y.; Sun, H.; An, P.; Chen, W.; Guo, Z.; Lee, C.; Chen, D.; Shakir, I.; Liu, M.; Hu, T.; Li, Y.; Kirkland, A. I.; Duan, X.; Huang, Y., General synthesis and definitive structural identification of MN₄C₄ single-atom catalysts with tunable electrocatalytic activities. *Nat. Catal.* **2018**, *1* (1), 63-72.

- 9. Garcés-Pineda, F. A.; Blasco-Ahicart, M.; Nieto-Castro, D.; López, N.; Galán-Mascarós, J. R., Direct magnetic enhancement of electrocatalytic water oxidation in alkaline media. *Nat. Energy* **2019**, *4* (6), 519-525.
- 10. McCrory, C. C.; Jung, S.; Peters, J. C.; Jaramillo, T. F., Benchmarking heterogeneous electrocatalysts for the oxygen evolution reaction. *J. Am. Chem. Soc.* **2013**, *135* (45), 16977-16987.
- McCrory, C. C.; Jung, S.; Ferrer, I. M.; Chatman, S. M.; Peters, J. C.;
 Jaramillo, T. F., Benchmarking hydrogen evolving reaction and oxygen evolving
 reaction electrocatalysts for solar water splitting devices. *J. Am. Chem. Soc.* 2015, 137 (13), 4347-4357.
- 12. Lewis, N. S.; Nocera, D. G., Powering the planet: Chemical challenges in solar energy utilization. *Proc. Natl. Acad. Sci. U.S.A.* **2006**, *103*, 15729-15735.
- 13. Hisatomi, T.; Kubota, J.; Domen, K., Recent advances in semiconductors for photocatalytic and photoelectrochemical water splitting. *Chem. Soc. Rev.* **2014**, *43* (22), 7520-7535.
- 14. Takata, T.; Jiang, J.; Sakata, Y.; Nakabayashi, M.; Shibata, N.; Nandal, V.; Seki, K.; Hisatomi, T.; Domen, K., Photocatalytic water splitting with a quantum efficiency of almost unity. *Nature* **2020**, *581* (7809), 411-414.
- 15. Zhou, P.; Navid, I. A.; Ma, Y.; Xiao, Y.; Wang, P.; Ye, Z.; Zhou, B.; Sun, K.; Mi, Z., Solar-to-hydrogen efficiency of more than 9% in photocatalytic water splitting. *Nature* **2023**, *613* (7942), 66-70.
- 16. Stamenkovic, V. R.; Strmcnik, D.; Lopes, P. P.; Markovic, N. M., Energy and fuels from electrochemical interfaces. *Nat. Mater.* **2016**, *16* (1), 57-69.

- 17. Han, L.; Dong, S.; Wang, E., Transition-Metal (Co, Ni, and Fe)-Based Electrocatalysts for the Water Oxidation Reaction. *Adv. Mater.* **2016**, *28* (42), 9266-9291.
- 18. Suen, N. T.; Hung, S. F.; Quan, Q.; Zhang, N.; Xu, Y. J.; Chen, H. M., Electrocatalysis for the oxygen evolution reaction: recent development and future perspectives. *Chem. Soc. Rev.* **2017**, *46* (2), 337-365.
- 19. Song, J.; Wei, C.; Huang, Z. F.; Liu, C.; Zeng, L.; Wang, X.; Xu, Z. J., A review on fundamentals for designing oxygen evolution electrocatalysts. *Chem. Soc. Rev.* **2020**, *49* (7), 2196-2214.
- 20. Yu, Z. Y.; Duan, Y.; Feng, X. Y.; Yu, X.; Gao, M. R.; Yu, S. H., Clean and Affordable Hydrogen Fuel from Alkaline Water Splitting: Past, Recent Progress, and Future Prospects. *Adv. Mater.* **2021,** *33* (31), e2007100.
- 21. Yin, J.; Jin, J.; Lu, M.; Huang, B.; Zhang, H.; Peng, Y.; Xi, P.; Yan, C. H., Iridium Single Atoms Coupling with Oxygen Vacancies Boosts Oxygen Evolution Reaction in Acid Media. *J. Am. Chem. Soc.* **2020**, *142* (43), 18378-18386.
- 22. Wu, Z. Y.; Chen, F. Y.; Li, B.; Yu, S. W.; Finfrock, Y. Z.; Meira, D. M.; Yan, Q. Q.; Zhu, P.; Chen, M. X.; Song, T. W.; Yin, Z.; Liang, H. W.; Zhang, S.; Wang, G.; Wang, H., Non-iridium-based electrocatalyst for durable acidic oxygen evolution reaction in proton exchange membrane water electrolysis. *Nat. Mater.* **2023**, *22* (1), 100-108.
- 23. Huynh, M.; Bediako, D. K.; Nocera, D. G., A functionally stable manganese oxide oxygen evolution catalyst in acid. *J. Am. Chem. Soc.* **2014,** *136* (16), 6002-6010.

- 24. Huynh, M.; Shi, C.; Billinge, S. J.; Nocera, D. G., Nature of Activated Manganese Oxide for Oxygen Evolution. *J. Am. Chem. Soc.* **2015**, *137* (47), 14887-14904.
- 25. Mondschein, J. S.; Callejas, J. F.; Read, C. G.; Chen, J. Y. C.; Holder, C. F.; Badding, C. K.; Schaak, R. E., Crystalline Cobalt Oxide Films for Sustained Electrocatalytic Oxygen Evolution under Strongly Acidic Conditions. *Chemistry of Materials* **2017**, *29* (3), 950-957.
- 26. Huynh, M.; Ozel, T.; Liu, C.; Lau, E. C.; Nocera, D. G., Design of template-stabilized active and earth-abundant oxygen evolution catalysts in acid. *Chem. Sci.* **2017**, *8* (7), 4779-4794.
- 27. Chatti, M.; Gardiner, J. L.; Fournier, M.; Johannessen, B.; Williams, T.; Gengenbach, T. R.; Pai, N.; Nguyen, C.; MacFarlane, D. R.; Hocking, R. K.; Simonov, A. N., Intrinsically stable in situ generated electrocatalyst for long-term oxidation of acidic water at up to 80 °C. *Nat. Catal.* **2019**, *2* (5), 457-465.
- 28. Yu, J.; Garces-Pineda, F. A.; Gonzalez-Cobos, J.; Pena-Diaz, M.; Rogero, C.; Gimenez, S.; Spadaro, M. C.; Arbiol, J.; Barja, S.; Galan-Mascaros, J. R., Sustainable oxygen evolution electrocatalysis in aqueous 1 M H₂SO₄ with earth abundant nanostructured Co₃O₄. *Nat. Commun.* **2022**, *13* (1), 4341.
- 29. Chong, L.; Gao, G.; Wen, J.; Li, H.; Xu, H.; Green, Z.; Sugar, J. D.; Kropf, A. J.; Xu, W.; Lin, X. M.; Xu, H.; Wang, L. W.; Liu, D. J., La- and Mn-doped cobalt spinel oxygen evolution catalyst for proton exchange membrane electrolysis. *Science* **2023**, *380*, 609-616.

- 30. Xiong, Q.; Zhang, X.; Wang, H.; Liu, G.; Wang, G.; Zhang, H.; Zhao, H., One-step synthesis of cobalt-doped MoS₂ nanosheets as bifunctional electrocatalysts for overall water splitting under both acidic and alkaline conditions. *Chem. Commun.* **2018**, *54* (31), 3859-3862.
- 31. Yang, Y.; Yao, H.; Yu, Z.; Islam, S. M.; He, H.; Yuan, M.; Yue, Y.; Xu, K.; Hao, W.; Sun, G.; Li, H.; Ma, S.; Zapol, P.; Kanatzidis, M. G., Hierarchical Nanoassembly of MoS₂/Co₉S₈/Ni₃S₂/Ni as a Highly Efficient Electrocatalyst for Overall Water Splitting in a Wide pH Range. *J. Am. Chem. Soc.* **2019**, *141* (26), 10417-10430.
- 32. Yin, Q.; Tan, J. M.; Besson, C.; Geletii, Y. V.; Musaev, D. G.; Kuznetsov, A. E.; Luo, Z.; Hardcastle, K. I.; Hill, C. L., A Fast Soluble Carbon-Free Molecular Water Oxidation Catalyst Based on Abundant Metals. *Science* **2010**, *328*, 342-345.
- 33. Vickers, J. W.; Lv, H.; Sumliner, J. M.; Zhu, G.; Luo, Z.; Musaev, D. G.; Geletii, Y. V.; Hill, C. L., Differentiating homogeneous and heterogeneous water oxidation catalysis: confirmation that [Co₄(H₂O)₂(α-PW₉O₃₄)₂]¹⁰⁻ is a molecular water oxidation catalyst. *J. Am. Chem. Soc.* **2013**, *135* (38), 14110-14118.
- 34. Lv, H.; Song, J.; Geletii, Y. V.; Vickers, J. W.; Sumliner, J. M.; Musaev, D. G.; Kogerler, P.; Zhuk, P. F.; Bacsa, J.; Zhu, G.; Hill, C. L., An exceptionally fast homogeneous carbon-free cobalt-based water oxidation catalyst. *J. Am. Chem. Soc.* **2014**, *136* (26), 9268-9271.
- 35. Blasco-Ahicart, M.; Soriano-Lopez, J.; Carbo, J. J.; Poblet, J. M.; Galan-Mascaros, J. R., Polyoxometalate electrocatalysts based on earth-abundant metals for efficient water oxidation in acidic media. *Nat Chem* **2018**, *10* (1), 24-30.

- 36. Arens, J. T.; Blasco-Ahicart, M.; Azmani, K.; Soriano-López, J.; García-Eguizábal, A.; Poblet, J. M.; Galan-Mascaros, J. R., Water oxidation electrocatalysis in acidic media with Co-containing polyoxometalates. *J. Catal.* **2020**, *389*, 345-351.
- 37. Goberna-Ferron, S.; Vigara, L.; Soriano-Lopez, J.; Galan-Mascaros, J. R., Identification of a nonanuclear {Co^{II9}} polyoxometalate cluster as a homogeneous catalyst for water oxidation. *Inorg. Chem.* **2012**, *51* (21), 11707-11715.
- 38. Mukhopadhyay, S.; Debgupta, J.; Singh, C.; Kar, A.; Das, S. K., A Keggin Polyoxometalate Shows Water Oxidation Activity at Neutral pH: POM@ZIF-8, an Efficient and Robust Electrocatalyst. *Angew. Chem., Int. Ed.* **2018,** *57* (7), 1918-1923.
- 39. Paille, G.; Gomez-Mingot, M.; Roch-Marchal, C.; Lassalle-Kaiser, B.; Mialane, P.; Fontecave, M.; Mellot-Draznieks, C.; Dolbecq, A., A Fully Noble Metal-Free Photosystem Based on Cobalt-Polyoxometalates Immobilized in a Porphyrinic Metal-Organic Framework for Water Oxidation. *J. Am. Chem. Soc.* **2018**, *140* (10), 3613-3618.
- 40. Folkman, S. J.; Soriano-Lopez, J.; Galan-Mascaros, J. R.; Finke, R. G., Electrochemically Driven Water-Oxidation Catalysis Beginning with Six Exemplary Cobalt Polyoxometalates: Is It Molecular, Homogeneous Catalysis or Electrode-Bound, Heterogeneous CoO_x Catalysis? *J. Am. Chem. Soc.* **2018**, *140* (38), 12040-12055.
- 41. Sullivan, K. P.; Wieliczko, M.; Kim, M.; Yin, Q.; Collins-Wildman, D. L.; Mehta, A. K.; Bacsa, J.; Lu, X.; Geletii, Y. V.; Hill, C. L., Speciation and Dynamics in the [Co₄V₂W₁₈O₆₈]¹⁰⁻/Co(II)aq/CoO_x Catalytic Water Oxidation System. *ACS Catal.* **2018**, *8* (12), 11952-11959.
- 42. Huang, Z.; Luo, Z.; Geletii, Y. V.; Vickers, J. W.; Yin, Q.; Wu, D.; Hou, Y.; Ding, Y.; Song, J.; Musaev, D. G.; Hill, C. L.; Lian, T., Efficient light-driven carbon-free

- cobalt-based molecular catalyst for water oxidation. *J. Am. Chem. Soc.* **2011**, *133* (7), 2068-2071.
- 43. Martin-Sabi, M.; Soriano-Lopez, J.; Winter, R. S.; Chen, J. J.; Vila-Nadal, L.; Long, D. L.; Galan-Mascaros, J. R.; Cronin, L., Redox tuning the Weakley-type polyoxometalate archetype for the oxygen evolution reaction. *Nat. Catal.* **2018**, *1* (3), 208-213.
- 44. Galán-Mascarós, J. R.; Gómez-Garcia, C. J.; Borrás-Almenar, J. J.; Coronado, E., High nuclearity magnetic clusters: Magnetic properties of a nine cobalt cluster encapsulated in a polyoxometalate, [Co₉(OH)₃(H₂O)₆(HPO₄)₂(PW₉O₃₄)₃]¹⁶-. *Adv. Mater.* **1994,** *6* (3), 221-223.
- 45. Suo, S.; Sheehan, C.; Zhao, F.; Xiao, L.; Xu, Z.; Meng, J.; Mallouk, T. E.; Lian, T., Direct Vibrational Stark Shift Probe of Quasi-Fermi Level Alignment in Metal Nanoparticle Catalyst-Based Metal-Insulator-Semiconductor Junction Photoelectrodes. *J. Am. Chem. Soc.* **2023**, *145* (26), 14260-14266.
- 46. Lauinger, S. M.; Sumliner, J. M.; Yin, Q.; Xu, Z.; Liang, G.; Glass, E. N.; Lian, T.; Hill, C. L., High Stability of Immobilized Polyoxometalates on TiO₂ Nanoparticles and Nanoporous Films for Robust, Light-Induced Water Oxidation. *Chem. Mater.* **2015**, *27* (17), 5886-5891.
- 47. Kanan, M. W.; Nocera, D. G., In Situ Formation of an Oxygen-Evolving Catalyst in Neutral Water Containing Phosphate and Co²⁺. *Science* **2008**, *321*, 1072-1075.
- 48. Zhong, D. K.; Choi, S.; Gamelin, D. R., Near-complete suppression of surface recombination in solar photoelectrolysis by "Co-Pi" catalyst-modified W:BiVO₄. *J. Am. Chem. Soc.* **2011**, *133* (45), 18370-18377.

- 49. Zhong, D. K.; Cornuz, M.; Sivula, K.; Grätzel, M.; Gamelin, D. R., Photo-assisted electrodeposition of cobalt–phosphate (Co–Pi) catalyst on hematite photoanodes for solar water oxidation. *Energy Environ. Sci.* **2011**, *4* (5), 1759-1764.
- 50. Blasco-Ahicart, M.; Soriano-Lopez, J.; Carbo, J. J.; Poblet, J. M.; Galan-Mascaros, J. R., Polyoxometalate electrocatalysts based on earth-abundant metals for efficient water oxidation in acidic media. *Nat. Chem.* **2018**, *10* (1), 24-30.
- 51. Challagulla, S.; Tarafder, K.; Ganesan, R.; Roy, S., Structure sensitive photocatalytic reduction of nitroarenes over TiO₂. *Sci. Rep.* **2017**, *7* (1), 8783.
- 52. El-Deen, S. S.; Hashem, A. M.; Abdel Ghany, A. E.; Indris, S.; Ehrenberg, H.; Mauger, A.; Julien, C. M., Anatase TiO₂ nanoparticles for lithium-ion batteries. *Ionics* **2018**, *24* (10), 2925-2934.
- 53. Chen, X.; Burda, C., The Electronic Origin of the Visible-Light Absorption Properties of C-, N- and S-Doped TiO₂ Nanomaterials. *J. Am. Chem. Soc.* **2008**, *130*, 5018-5019.
- 54. Amorello, D.; Ledda, F.; Romano, V.; Zingales, R., Batch Experiments for the Determination of the Ti(IV,III) Couple Formal Potential in 1 mol·dm⁻³ HCl, 2 mol·dm⁻³ NaCl Medium at 25 °C. *J. Solution Chem.* **2008**, *38* (2), 259-263.
- 55. Ma, Y.; Kafizas, A.; Pendlebury, S. R.; Le Formal, F.; Durrant, J. R., Photoinduced Absorption Spectroscopy of CoPi on BiVO₄: The Function of CoPi during Water Oxidation. *Adv. Funct. Mater.* **2016**, *26* (27), 4951-4960.
- 56. Nellist, M. R.; Laskowski, F. A. L.; Qiu, J.; Hajibabaei, H.; Sivula, K.; Hamann, T. W.; Boettcher, S. W., Potential-sensing electrochemical atomic force microscopy for

- in operando analysis of water-splitting catalysts and interfaces. *Nat. Energy* **2018,** 3 (1), 46-52.
- 57. Barroso, M.; Cowan, A. J.; Pendlebury, S. R.; Gratzel, M.; Klug, D. R.; Durrant, J. R., The role of cobalt phosphate in enhancing the photocatalytic activity of α-Fe₂O₃ toward water oxidation. *J. Am. Chem. Soc.* **2011**, *133* (38), 14868-14871.
- 58. Yoshihara, T.; Katoh, R.; Furube, A.; Tamaki, Y.; Murai, M.; Hara, K.; Murata, S.; Arakawa, H.; Tachiya, M., Identification of Reactive Species in Photoexcited Nanocrystalline TiO₂ Films by Wide-Wavelength-Range (400-2500 nm) Transient Absorption Spectroscopy. *J. Phys. Chem. B.* **2004**, *108*, 3817-3823.
- 59. Cowan, A. J.; Tang, J.; Leng, W.; Durrant, J. R.; Klug, D. R., Water Splitting by Nanocrystalline TiO₂ in a Complete Photoelectrochemical Cell Exhibits Efficiencies Limited by Charge Recombination. *J. Phys. Chem. C* **2010**, *114*, 4208-4214.
- 60. Kafizas, A.; Wang, X.; Pendlebury, S. R.; Barnes, P.; Ling, M.; Sotelo-Vazquez, C.; Quesada-Cabrera, R.; Li, C.; Parkin, I. P.; Durrant, J. R., Where Do Photogenerated Holes Go in Anatase:Rutile TiO₂? A Transient Absorption Spectroscopy Study of Charge Transfer and Lifetime. *J. Phys. Chem. A.* **2016**, *120* (5), 715-723.
- 61. Sachs, M.; Pastor, E.; Kafizas, A.; Durrant, J. R., Evaluation of Surface State Mediated Charge Recombination in Anatase and Rutile TiO₂. *J. Phys. Chem. Lett.* **2016**, *7* (19), 3742-3746.
- 62. Godin, R.; Wang, Y.; Zwijnenburg, M. A.; Tang, J.; Durrant, J. R., Time-Resolved Spectroscopic Investigation of Charge Trapping in Carbon Nitrides

- Photocatalysts for Hydrogen Generation. *J. Am. Chem. Soc.* **2017**, *139* (14), 5216-5224.
- 63. Yang, W.; Godin, R.; Kasap, H.; Moss, B.; Dong, Y.; Hillman, S. A. J.; Steier, L.; Reisner, E.; Durrant, J. R., Electron Accumulation Induces Efficiency Bottleneck for Hydrogen Production in Carbon Nitride Photocatalysts. *J. Am. Chem. Soc.* **2019**, *141* (28), 11219-11229.
- 64. Nelson, J.; Chandler, R. E., Random walk models of charge transfer and transport in dye sensitized systems. *Coord. Chem. Rev.* **2004**, *248* (13), 1181-1194.
- 65. Yamakata, A.; Ishibashi, T.-a.; Onishi, H., Time-resolved infrared absorption spectroscopy of photogenerated electrons in platinized TiO₂ particles. *Chem. Phys. Lett.* **2001**, 333, 271-277.
- 66. Yamakata, A.; Ishibashi, T.-a.; Onishi, H., Water- and Oxygen-Induced Decay Kinetics of Photogenerated Electrons in TiO₂ and Pt/TiO₂: A Time-Resolved Infrared Absorption Study. *J. Phys. Chem. B.* **2001**, *105*, 7258-7262.
- 67. Song, J.; Long, J.; Liu, Y.; Xu, Z.; Ge, A.; Piercy, B. D.; Cullen, D. A.; Ivanov, I. N.; McBride, J. R.; Losego, M. D.; Lian, T., Highly Efficient Plasmon Induced Hot-Electron Transfer at Ag/TiO₂ Interface. *ACS Photonics* **2021**, *8* (5), 1497-1504.
- 68. Brito, R.; A., R. V.; Figueroa, J.; Cabrera, C. R., Adsorption of 3-mercaptopropyltrimethoxysilane and 3-aminopropyltrimethoxysilane at platinum electrodes. *J. Electroanal. Chem.* **2002**, *520*, 47-52.
- 69. Ueda, T., Electrochemistry of Polyoxometalates: From Fundamental Aspects to Applications. *ChemElectroChem* **2018**, *5* (6), 823-838.

Chapter 5:

Polyoxometalate-Incorporated Metal-Organic Frameworks for Aerobic Thiol Oxidation

Abstract: A multi-electron-capable POM captured in the pores of a metal-organic framework (MOF), HKUST-1 (POM@HKUST), is synthesized to achieve the synergism between polyoxometalates (POM) and Cu(II) ion for aerobic thiol oxidation that has already been established in homogeneous solutions. The synergism between POM and the Cu(II) nodes in the MOF depends on the type of POM. The incorporation of phosphovanadomolybdates, PVxMo12-xO40^{(3+x)-} (x = 1-3) (PVMo), but not transition-metal-substituted polytungstates, PXW11 (X = V, Co, Zn and Co), results in POM@MOF materials that exhibit synergy not only for reactivity but also for catalyst structural stability. The PVMo@HKUST materials catalyze thiol oxidation reaction with nearly 100% conversion and the material is recoverable and unchanged based on FTIR spectroscopy, powder XRD data and other observations after reaction. In contrast, PXW11@HKUST materials show limited activity and decompose to white powders after the reaction.

5.1 Introduction:

POM@MOF composites comprising polyoxometalates (POMs) residing in metalorganic framework (MOF) pores.^{1–4} have been reported as catalysts for oxidative, electrocatalytic, photocatalytic and other reactions.^{3–6} A central point of interest is that they can combine the attractive properties of POMs and also those of MOFs. POMs have been investigated as catalysts for years,^{7–10} resulting from one or more of their following attributes: strong acidity,^{11,12} facile redox chemistry,^{13–16} photoactivity^{17–22} and multielectron transfer ability.^{17,23,24} POMs in conventional solid phases, not pseudoliquid phases,²⁵ have small surface areas but are soluble in aqueous and many organic solvents. Thus, the immobilization of POMs on porous materials, including polymers,²⁶ covalent organic frameworks (COFs),²⁷ zeolites²⁸ and MOFs,^{29–32} is attractive because it converts these homogeneous catalysts into more utilitarian heterogeneous ones with substantial surface area. Among all POM supports, MOFs, such as MIL-101,^{33–35} MOF-199 (HKUST-1),^{4,36–38} NU-1000,^{39–42} UIO-66 ^{43–46} and ZIF-8 ^{47–49} are highly attractive host materials because they offer high porosity and sufficient pore (cage) size to encapsulate POMs, including Keggin,³⁷ Wells-Dawson⁴³ and sandwich structural families,⁵⁰ as guest materials forming POM@MOF composites.

Recent work in our group^{51,52} reveals strong synergism effect between Cu(II) ion and phosphovanadomolybdates, $PV_xMo_{12-x}O_{40}^{(3+x)-}$ (x = 1-6) (PVMo) for catalysis of airbased oxidative removal of odorous thiols, facilitated by the redox buffering effect of PVMo. Moreover, the redox buffering and synergism are only operative for PVMo and not phosphovanadotungstates, $PV_xW_{12-x}O_{40}^{(3+x)-}$ (x = 1, 3, 6) (PVW). Triggered by this, we sought formulation of a solid and thus more useful catalyst for aerobic thiol deodorization by combining Cu(II) and POM together as a heterogeneous catalyst. Here, we use the POM, HKUST-1 with Cu-containing nodes to bring Cu(II) and reversible multi-electron POM centers into proximity. HKUST-1, in addition to providing wellligated Cu(II), contains large pores that accommodate Keggin POMs with their accompanying counter-cations in the smaller pores. Various Keggin POMs have been incorporated into HKUST-1 for oxidation, ^{36,53–59} esterification, ^{60,61} hydrolysis ³⁷ and other organocatalytic reactions.⁶² Many efforts have been made to increase the catalytic activity such as tuning the nanocrystal size, 53 modifying the morphology, 60 designing the hierarchical structure⁵⁷ and regulating the pore size.⁶³ Incorporating Keggin POMs into

HKUST-1 not only increases the thermal⁶⁴ and hydrolytic³⁶ stability of the MOF but also increases the reactivity of the POM with a marked synergy between POM and MOF framework.^{36,53–55} However, almost all the synergism reported previously is due to the MOF framework confinement effect that enhances the absorption, selectivity, and conversion of organic substrates, while POM is the real catalytic center of the reaction.^{53–55} In this work, we show that the aerobic thiol oxidation mechanism involves both the Cu(II) nodes in the MOF framework and multi-electron redox processes of the POM polyanion. In addition, we show that synergistic electron transfer between MOF and POM maintains the overall POM@MOF framework.

5.2 Experimental

5.2.1 General Materials and Methods

All the polyoxometalates (POM) including $[PVMo_{11}]^{4-}$, $[PV_2Mo_{10}]^{5-}$, $[PV_3Mo_9]^{6-}$, $[PVW_{11}]^{5-}$, $[PV_2W10]^{5-}$, $[PV_2W10]^{5-}$, $[PCoW_{11}]^{5-}$ and $[PCuW_{11}]^{5-}$ were synthesized according to literature methods. PVMo@HKUST ($PV_nMo_{12-n}O_{40}^{(3+n)-}$) $[PMo_{12}]^{3-}$, $[PVMo_{11}]^{4-}$, $[PV_2Mo_{10}]^{5-}$ and $[PV_3Mo_9]^{6-}$, in HKUST-1) and $PW_{12}@HKUST$ were prepared following literature methods. All other chemicals and solvents were purchased from commercial sources without further purification. The FT-IR spectra were collected on a Nicolet TM 600 FT-IR spectrometer by the attenuated total reflectance (ATR) sampling technique. Powder XRD data were collected on a D8 Discover Powder Instrument using monochromatic Cu K α (λ = 1.54060 Å) radiation. SEM-EDX data were collected on a HITACHI SU8230 FE-SEM. The POM@MOF samples were coated with gold using a Hummer 6 sputterer. UV-vis spectra were collected with an Agilent 8453

spectrophotometer using a 1.0 cm optical path length quartz cuvette. The kinetics were followed by an SF-61 stopped-flow instrument (Hi-Tech Scientific, U.K.) ¹H nuclear magnetic resonance (NMR) spectra were acquired on a Varian INOVA 400 spectrometer. The thermogravimetric (TGA) data were collected on a Mettler Toledo TGA instrument. X-ray photoelectron spectroscopy (XPS) was conducted on a thermos K-ALPHA XPS instrument. The nitrogen isotherms were collected by Micromeritics Instrument Corporation.

5.2.2 Synthesis of POM@HKUST

PXW@HKUST ([PVW₁₁]⁵⁻, [PCoW₁₁]⁵⁻ and [PNiW₁₁]⁵⁻ in HKUST-1) were synthesized by modified methods as previously reported for PCuW₁₁@HKUST.⁹ In a typical experiment, Cu(NO₃)₂-2.5H₂O (240 mg) and POM (200 mg) were added to a flask with 10 mL of distilled water and stirred for 20 min. Trimesic acid (210 mg) and (CH₃)₄NOH (180 mg) were then added sequentially and stirred for 10 min after each addition. The solution was stirred until a uniform dispersion was achieved. The resulting solution (pH ~ 2 for [PVW₁₁]⁵⁻, pH ~ 4 for [PCoW₁₁]⁵⁻ and [PNiW₁₁]⁵⁻) was transferred to a Teflon-lined Parr bomb, programmatically heated up to 200 °C for 16 h, then cooled down and maintained at 100 °C for another 4 h. Finally, the reactor was allowed to cool to ambient temperature. Blue or dark green crystals were obtained and separated from the solution. The products were washed 3 times with distilled water, 3 times with 50% v/v ethanol at 50 °C, then dried in vacuo overnight to remove solvent molecules. The crystal structures were characterized by single crystal X-ray diffraction. Their purity was confirmed by Fourier transform infrared (FT-IR) and powder X-ray diffraction (XRD)

analyses. The new materials in this work are PVW₁₁@HKUST, PCoW₁₁@HKUST and PNiW₁₁@HKUST.

5.2.3 Thiol (RSH) oxidation

An exemplary substrate, 2-mercaptoethanol, was used for probing the aerobic thiol oxidation mechanism, eq S1, where RSH is 2-mercaptoethanol. The product (bis(2-hydroxyethyl) disulfide (RSSR)) was formed : 2 RSH + $\frac{1}{2}$ O₂ \rightarrow RSSR + H₂O In a typical RSH oxidation catalyzed by the heterogeneous POM@HKUST systems, 20 mg catalyst, 28.6 mM RSH and 5 mL dichloroethane were stirred in a 50 mL heavy-wall glass pressure vessel at 50 °C under air. Aliquots were withdrawn every hour, and the RSH concentration was determined using Ellman's reagent, 5,5-dithiobis(2-nitrobenzoic acid (DTNB). The head space of the vessel was purged with fresh air every hour. The product RSSR was confirmed by 1 H NMR. The POM@HKUST catalysts were collected by centrifugation and dried under vacuum overnight then evaluated to quantify stability. The IR spectrum and powder XRD were measured and compared with those data before RSH oxidation.

5.3 Results and discussion

5.3.1 POM@MOF Materials and Characterization

 $PV_xMo_{12-x}O_{40}^{(3+x)-}$ (x = 0-3) (PVMo) were incorporated into the HKUST-1 using the well-established hydrothermal synthetic method,^{37,38} however the synthesis of POM@HKUST with PVMo with x>3 using the same synthetic method failed. It is possibly because of the decreasing hydrolytic stability of PVMo with the increasing number of V on it. We note that there are other synthetic methods to synthesize

POM@HKUST materials^{53,61,65,66} that we didn't explore. Thus, in this work, PVMo@HKUST (PVMo11@HKUST, PV2Mo10@HKUST and PV3Mo9@HKUST) were discussed. The phase purity of PVMo@HKUST was established by FT-IR spectra and powder X-ray diffraction (PXRD) patterns (Figures 5.1a, b). For the PVW, only x=0, 1 can be inserted into HKUST-1 (PW12@HKUST and PVW11@HKUST). This likely derives from the fact that unlike the corresponding Mo-based Keggin POMs, the Keggin polytungstates are more rigid and far less hydrolytically labile. In addition, we succeeded in incorporating a series of transition-metal-substituted polytungstates (PXW11, X = Cu, Co and Ni) into HKUST-1. FT-IR spectroscopies establish the phase purity of these materials as shown in Figures 5.2. Nitrogen isotherms of PV2Mo10@HKUST and PCoW11@HKUST (Figure 5.3) show the specific surface area are 619.2 and 413.5 m²/g, respectively, which are comparable with previous reports.^{36,60} Compared with the HKUST-1 alone, 1264 m²/g,³⁶ the smaller specific surface area can be attributed to the successful insertion of POMs.

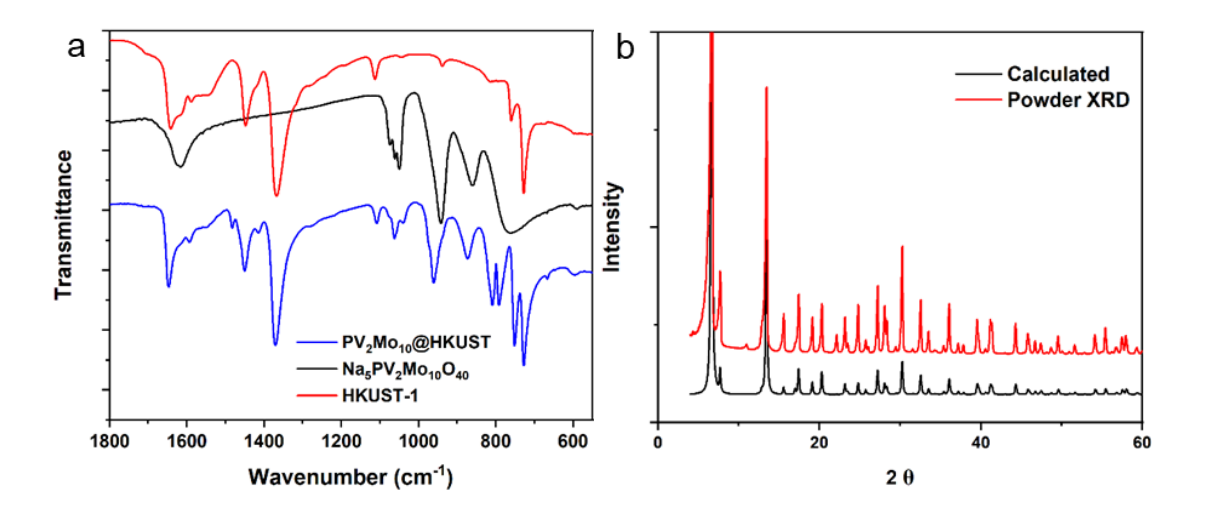


Figure 5.1. (a) FT-IR of Na₅PV₂Mo₁₀O₄₀, HKUST-1 and PV₂Mo₁₀@HKUST; (b) PV₂Mo₁₀@HKUST calculated XRD pattern from single-crystal refinement data compare with the experimental powder XRD pattern.

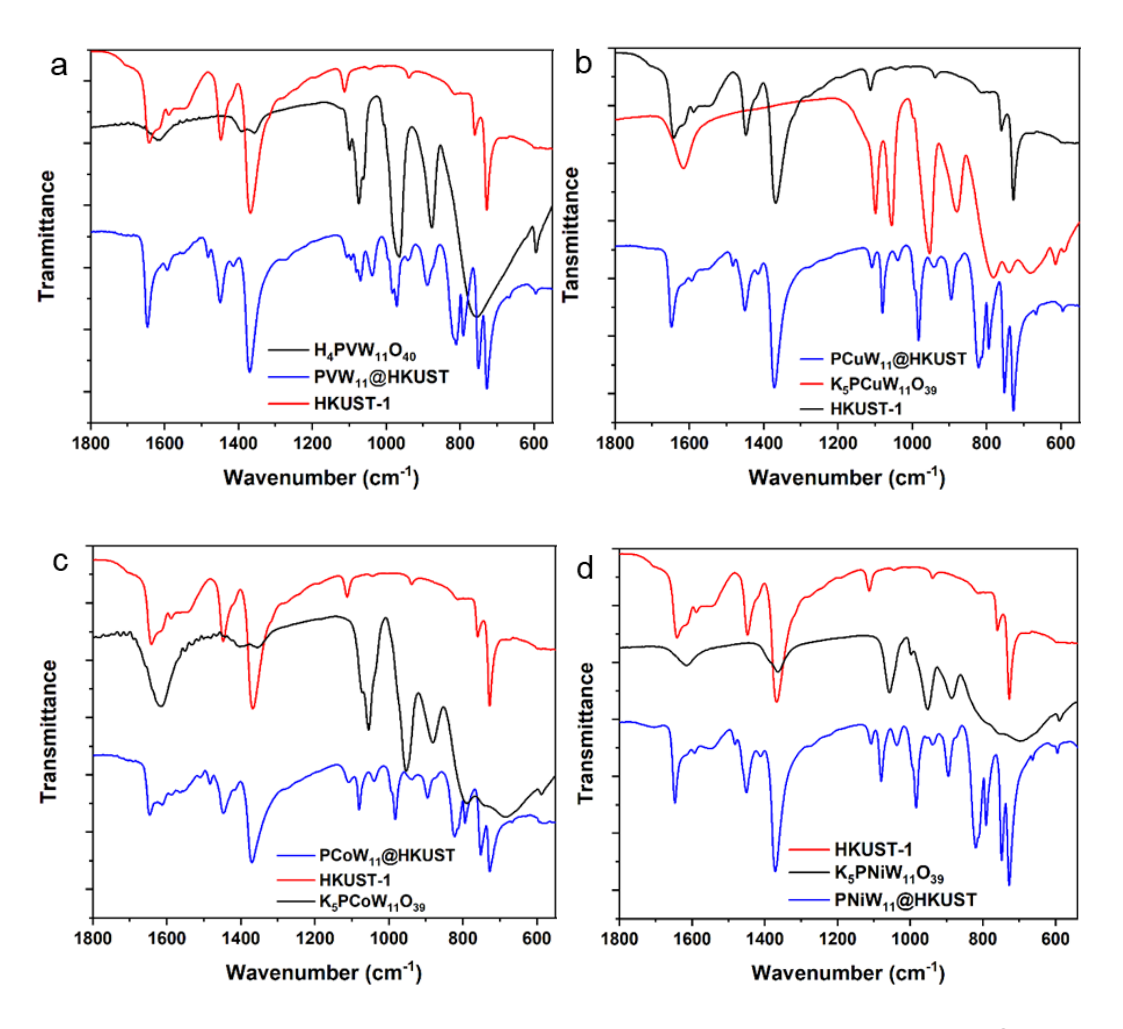


Figure 5.2. FT-IR of POM alone, HKUST-1 and the corresponding PXW₁₁@HKUST. (a) PVW₁₁@HKUST; (b) PCuW₁₁@HKUST; (c) PCoW₁₁@HKUST; (d) PNiW₁₁@HKUST.

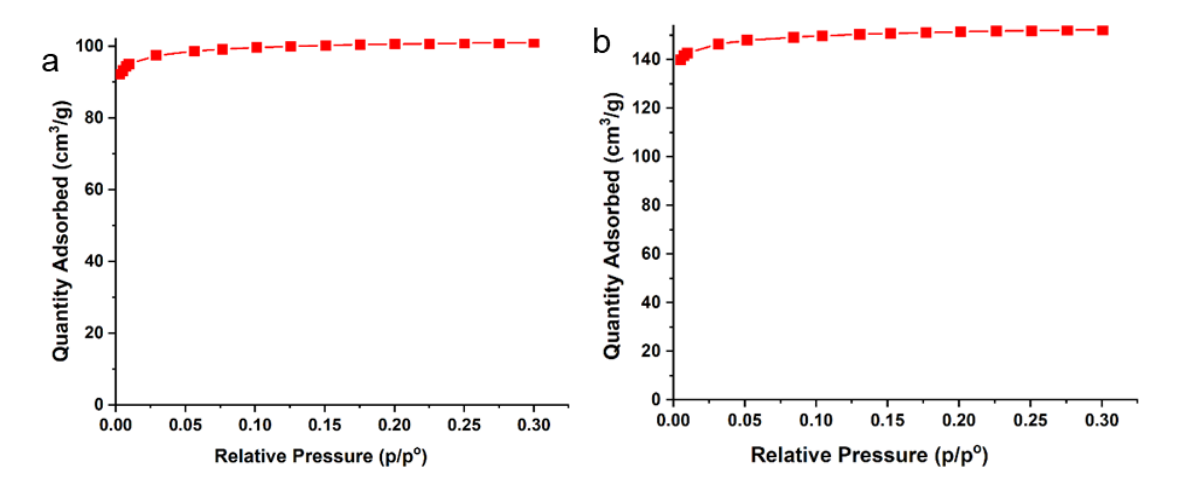


Figure 5.3. N_2 gas adsorption isotherms of $PV_2Mo_{10}@HKUST$ and $PCoW_{11}@HKUST$ measured at 77 K.

5.3.2 POM Leaching and Solvent Selection

The leaching of POM from MOF pores during the reaction is a potential issue for POM@MOF materials.^{3,4} Figure 5.4a shows the thiol (RSH) oxidation reactivity of PV₂Mo₁₀@HKUST in different organic solvents. Auto-catalytic behavior is seen in acetonitrile (AN) and dimethylacetamide (DMA). This is because POM is leached into the solution during reaction in these polar POM-solubilizing solvents, and the dominant mode of catalysis switches from heterogeneous to homogeneous by POM in solution. To further address POM leaching from MOF pores in these catalytic studies, we developed a colorimetric method to detect whether POM is extracted into the solution. Supernatants were filtered after the oxidation reaction, then SnCl₂, a strong reducing agent, was added to the argon-purged, filtered solution. Since Mo(VI)-Mo(V) intervalence charge transfer (IVCT) band has very high extinction coefficient around 600-800 nm,67 even a trace amount of POM that leaks into the solution is rapidly reduced and quantified by the UV-Vis spectroscopy. Figure 5.4b shows the UV-Vis results. When ethanol is used as a solvent, a slight absorbance due to reduced POM in solution is observed; when AN and DMA are used, large absorbances are observed. When solvents less polar than ethanol are used, no absorbances around 600-800 nm are generated. Here we use dielectric constant (ε) to differentiate and quantify the polarity of the organic solvents. The reactivity increases as ε increases, however, when ε is too large (ethanol, 24.6), the POM starts to leach from the MOF pores. As a consequence, we chose dichloroethane for all the catalytic studies.

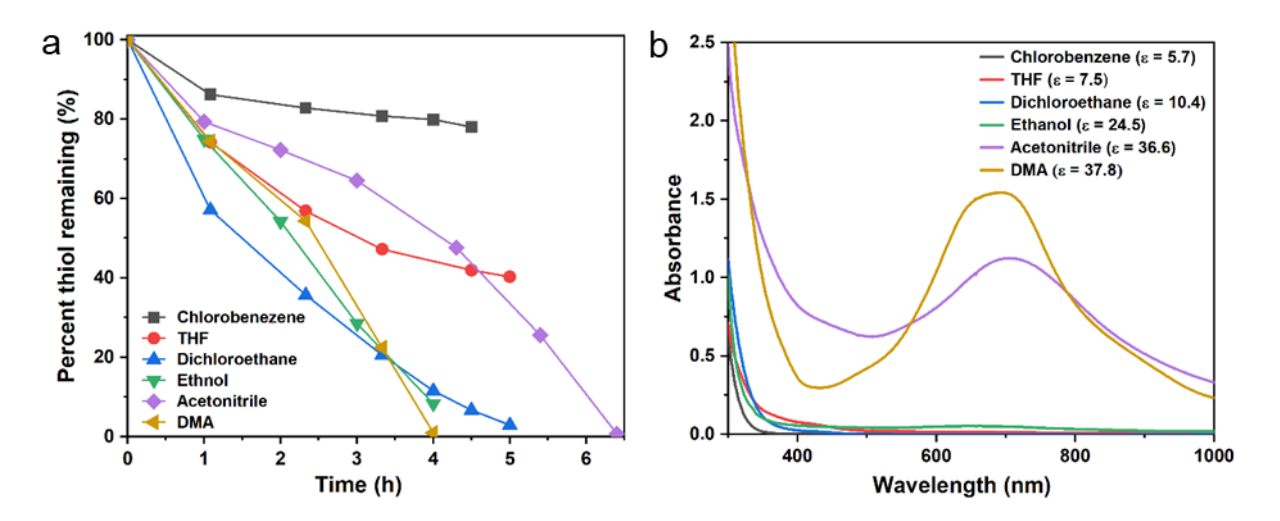


Figure 5.4. (a) RSH consumption catalyzed by $PV_2Mo_{10}@HKUST$ in different solvents. Conditions: dichloroethane (5 mL), 2-mercaptoethanol (28.6 mM), catalyst (0.774 mM), reaction at 50 °C. (b) UV-Vis absorbance of the reduced supernatant solution after addition of $SnCl_2$ under argon after reaction.

5.4 Conclusion

In this work, phosphovanadomolybdates, PV_xMo_{12-x}O₄₀(^{3+x)-} (x = 1-3) (PVMo), and transition-metal-substituted polytungstates, PXW₁₁ (X = V, Co, Zn and Co)-incorporated HKUST-1 materials are synthesized based on the hydrothermal method. While PXW₁₁@HKUST materials exhibit limited catalytic activity for the thiol oxidation reaction and decompose to white powders after reaction, PVMo@HKUST materials catalyze the thiol oxidation reaction with nearly 100% conversion and high stability and recoverability based on FTIR spectroscopy, powder XRD data and other observations after reaction. The superior performance of PVMo@HKUST materials is attributed to the synergism between POM and the Cu(II) nodes in the HKUST.

5.5 References

- J. X. Liu, X. B. Zhang, Y. L. Li, S. L. Huang and G. Y. Yang, *Coord. Chem. Rev.*,
 2020, 414, 213260.
- D. Y. Du, J. S. Qin, S. L. Li, Z. M. Su and Y. Q. Lan, *Chem. Soc. Rev.*, 2014, 43, 4615–4632.
- J. Sun, S. Abednatanzi, P. Van Der Voort, Y. Y. Liu and K. Leus, *Catalysts*, 2020,10, 578.
- 4 M. Samaniyan, M. Mirzaei, R. Khajavian, H. Eshtiagh-Hosseini and C. Streb, *ACS Catal.*, 2019, **9**, 10174–10191.
- 5 M. Genovese and K. Lian, Curr. Opin. Solid State Mater. Sci., 2015, 19, 126–137.
- Y. Liu, C. Tang, M. Cheng, M. Chen, S. Chen, L. Lei, Y. Chen, H. Yi, Y. Fu and L.
 Li, ACS Catal., 2021, 11, 13374–13396.
- 7 M. T. Pope and A. Müller, *Angew. Chemie Int. Ed. English*, 1991, **30**, 34–48.
- 8 C. L. Hill and C. M. Prosser-McCartha, Coord. Chem. Rev., 1995, **143**, 407–455.
- 9 C. L. Hill, L. Delannoy, D. C. Duncan, I. A. Weinstock, R. F. Renneke, R. S. Reiner, R. H. Atalla, J. W. Han, D. A. Hillesheim, R. Cao, T. M. Anderson, N. M. Okun, D. G. Musaev and Y. V. Geletii, *Comptes Rendus Chim.*, 2007, **10**, 305–312.
- 10 S. S. Wang and G. Y. Yang, *Chem. Rev.*, 2015, **115**, 4893–4962.
- 11 I. V. Kozhevnikov, *Chem. Rev.*, 1998, **98**, 171–198.

- 12 I. V. Kozhevnikov, *J. Mol. Catal. A Chem.*, 1997, **117**, 151–158.
- 13 R. Neumann, *Inorg. Chem.*, 2010, **49**, 3594–3601.
- I. A. Weinstock, R. E. Schreiber and R. Neumann, *Chem. Rev.*, 2018, **118**, 2680–2717.
- Noritaka Mizuno and Makoto Misono*, *Chem. Rev.*, 1998, **98**, 199–217.
- 16 K. P. Sullivan, M. Wieliczko, M. Kim, Q. Yin, D. L. Collins-Wildman, A. K. Mehta, J. Bacsa, X. Lu, Y. V. Geletii and C. L. Hill, *ACS Catal.*, 2018, **8**, 11952–11959.
- J. J. Walsh, A. M. Bond, R. J. Forster and T. E. Keyes, *Coord. Chem. Rev.*, 2016,
 306, 217–234.
- 18 T. Yamase, *Chem. Rev.*, 1998, **98**, 307–325.
- 19 E. Papaconstantinou, *Chem. Soc. Rev.*, 1989, **18**, 1–31.
- 20 C. Streb, *Dalt. Trans.*, 2012, **41**, 1651–1659.
- 21 J. M. Cameron, D. J. Wales and G. N. Newton, *Dalt. Trans.*, 2018, **47**, 5120–5136.
- M. Tao, Q. Yin, A. L. Kaledin, N. Uhlikova, X. Lu, T. Cheng, Y. S. Chen, T. Lian, Y. V. Geletii, D. G. Musaev, J. Bacsa and C. L. Hill, *Inorg. Chem.*, 2022, **61**, 6252–6262.
- 23 I. A. Weinstock, *Chem. Rev.*, 1998, **98**, 113–170.
- 24 M. Sadakane and E. Steckhan, *Chem. Rev.*, 1998, **98**, 219–237.
- Noritaka Mizuno and Makoto Misono, Chem. Rev., 1998, 98, 199–217.

- 26 V. G. Snider and C. L. Hill, *J. Hazard. Mater.*, 2023, **442**, 130015.
- 27 H. Ma, B. Liu, B. Li, L. Zhang, Y. G. Li, H. Q. Tan, H. Y. Zang and G. Zhu, *J. Am. Chem. Soc.*, 2016, **138**, 5897–5903.
- 28 L. Vilà-Nadal and L. Cronin, *Nat. Rev. Mater.*, 2017, **2**, 1–15.
- 29 Q. Wang and D. Astruc, *Chem. Rev.*, 2020, **120**, 1438–1511.
- 30 Q. L. Zhu and Q. Xu, Chem. Soc. Rev., 2014, 43, 5468–5512.
- 31 J. L. C. Rowsell and O. M. Yaghi, *Microporous Mesoporous Mater.*, 2004, **73**, 3–14.
- 32 H. Furukawa, K. E. Cordova, M. O'Keeffe and O. M. Yaghi, *Science (80-.).*, 2013, **341**, 1230444.
- 33 N. V. Maksimchuk, O. A. Kholdeeva, K. A. Kovalenko and V. P. Fedin, *Isr. J. Chem.*, 2011, **51**, 281–289.
- J. Juan-Alcañiz, E. V. Ramos-Fernandez, U. Lafont, J. Gascon and F. Kapteijn, *J. Catal.*, 2010, **269**, 229–241.
- 35 G. Férey, C. Mellot-Draznieks, C. Serre, F. Millange, J. Dutour, S. Surblé and I. Margiolaki, *Science (80-.).*, 2005, **309**, 2040–2042.
- 36 J. Song, Z. Luo, D. K. Britt, H. Furukawa, O. M. Yaghi, K. I. Hardcastle and C. L. Hill, J. Am. Chem. Soc., 2011, 133, 16839–16846.
- 37 C. Y. Sun, S. X. Liu, D. D. Liang, K. Z. Shao, Y. H. Ren and Z. M. Su, J. Am. Chem. Soc., 2009, 131, 1883–1888.

- 38 L. Yang, H. Naruke and T. Yamase, *Inorg. Chem. Commun.*, 2003, **6**, 1020–1024.
- S. Ahn, S. L. Nauert, C. T. Buru, M. Rimoldi, H. Choi, N. M. Schweitzer, J. T.
 Hupp, O. K. Farha and J. M. Notestein, *J. Am. Chem. Soc.*, 2018, **140**, 8535–8543.
- 40 C. T. Buru, A. E. Platero-Prats, D. G. Chica, M. G. Kanatzidis, K. W. Chapman and O. K. Farha, *J. Mater. Chem. A*, 2018, **6**, 7389–7394.
- C. T. Buru, P. Li, B. L. Mehdi, A. Dohnalkova, A. E. Platero-Prats, N. D. Browning,K. W. Chapman, J. T. Hupp and O. K. Farha, *Chem. Mater.*, 2017, 29, 5174–5181.
- 42 C. T. Buru, M. C. Wasson and O. K. Farha, *ACS Appl. Nano Mater.*, 2020, **3**, 658–664.
- W. Salomon, C. Roch-Marchal, P. Mialane, P. Rouschmeyer, C. Serre, M.
 Haouas, F. Taulelle, S. Yang, L. Ruhlmann and A. Dolbecq, *Chem. Commun.*,
 2015, 51, 2972–2975.
- 44 W. Xie and F. Wan, *Chem. Eng. J.*, 2019, **365**, 40–50.
- 45 Y. L. Peng, J. Liu, H. F. Zhang, D. Luo and D. Li, *Inorg. Chem. Front.*, 2018, **5**, 1563–1569.
- 46 L. Zeng, L. Xiao, Y. Long and X. Shi, *J. Colloid Interface Sci.*, 2018, **516**, 274–283.
- 47 R. Li, X. Ren, J. Zhao, X. Feng, X. Jiang, X. Fan, Z. Lin, X. Li, C. Hu and B. Wang, *J. Mater. Chem. A*, 2014, **2**, 2168–2173.
- 48 Q. Y. Li, L. Zhang, Y. X. Xu, Q. Li, H. Xue and H. Pang, *ACS Sustain. Chem. Eng.*, 2019, **7**, 5027–5033.

- 49 S. Mukhopadhyay, J. Debgupta, C. Singh, A. Kar and S. K. Das, *Angew. Chemie Int. Ed.*, 2018, **57**, 1918–1923.
- G. Paille, M. Gomez-Mingot, C. Roch-Marchal, B. Lassalle-Kaiser, P. Mialane, M. Fontecave, C. Mellot-Draznieks and A. Dolbecq, *J. Am. Chem. Soc.*, 2018, 140, 3613–3618.
- 51 X. Lu, T. Cheng, Y. V. Geletii and C. L. Hill, *Inorg. Chem.*, 2023, **5**, 2404–2414.
- 52 X. Lu, Y. V Geletii, T. Cheng and C. L. Hill, *Inorg. Chem.*, 2023, **14**, 5822–5830.
- Y. Liu, S. Liu, S. Liu, D. Liang, S. Li, Q. Tang, X. Wang, J. Miao, Z. Shi and Z.Zheng, *ChemCatChem*, 2013, 5, 3086–3091.
- 54 X. Zhong, Y. Lu, F. Luo, Y. Liu, X. Li and S. Liu, *Chem. A Eur. J.*, 2018, **24**, 3045–3051.
- 55 J. Zhu, P. C. Wang and M. Lu, *Catal. Sci. Technol.*, 2015, **5**, 3383–3393.
- J. Zhu, M. N. Shen, X. J. Zhao, P. C. Wang and M. Lu, *Chempluschem*, 2014, **79**, 872–878.
- 57 X. Xu, S. Chen, Y. Chen, H. Sun, L. Song, W. He and X. Wang, *Small*, 2016, **12**, 2982–2990.
- 58 H. Yang, J. Li, L. Wang, W. Dai, Y. Lv and S. Gao, *Catal. Commun.*, 2013, **35**, 101–104.
- 59 E. Rafiee and N. Nobakht, *J. Mol. Catal. A Chem.*, 2015, **398**, 17–25.
- Y. Liu, S. Liu, D. He, N. Li, Y. Ji, Z. Zheng, F. Luo, S. Liu, Z. Shi and C. Hu, J. Am.

- Chem. Soc., 2015, 137, 12697–12703.
- 61 L. H. Wee, S. R. Bajpe, N. Janssens, I. Hermans, K. Houthoofd, C. E. A. Kirschhock and J. A. Martens, *Chem. Commun.*, 2010, **46**, 8186–8188.
- 62 Z. Wang and Q. Chen, *Green Chem.*, 2016, **18**, 5884–5889.
- 63 L. H. Wee, C. Wiktor, S. Turner, W. Vanderlinden, N. Janssens, S. R. Bajpe, K. Houthoofd, G. Van Tendeloo, S. De Feyter, C. E. A. Kirschhock and J. A. Martens, J. Am. Chem. Soc., 2012, 134, 10911–10919.
- D. Mustafa, E. Breynaert, S. R. Bajpe, J. A. Martens and C. E. A. Kirschhock, *Chem. Commun.*, 2011, **47**, 8037–8039.
- 65 C. R. W. and M. Dincă, *Dalt. Trans.*, 2012, **41**, 7782–7791.
- S. R. Bajpe, C. E. A. Kirschhock, A. Aerts, E. Breynaert, G. Absillis, T. N. Parac-Vogt, L. Giebeler and J. A. Martens, *Chem. A Eur. J.*, 2010, **16**, 3926–3932.
- E. A. Nagul, I. D. McKelvie, P. Worsfold and S. D. Kolev, *Anal. Chim. Acta*, 2015,890, 60–82.